

Louisiana Tech University

## Louisiana Tech Digital Commons

---

Doctoral Dissertations

Graduate School

---

Fall 11-2021

### **Lab-on-a-chip Thermoelectric and Solid-phase Immunodetection of Biochemical Analytes and Extracellular Vesicles: Experimental and Computational Analysis**

Saif Mohammad Ishraq Bari

Follow this and additional works at: <https://digitalcommons.latech.edu/dissertations>

---

**LAB-ON-A-CHIP THERMOELECTRIC AND SOLID-PHASE  
IMMUNODETECTION OF BIOCHEMICAL ANALYTES AND  
EXTRACELLULAR VESICLES: EXPERIMENTAL AND  
COMPUTATIONAL ANALYSIS**

by

Saif Mohammad Ishraq Bari, B.S., M.S.

A Dissertation Presented in Partial Fulfillment  
of the Requirements for the Degree  
Doctor of Philosophy

COLLEGE OF ENGINEERING AND SCIENCE  
LOUISIANA TECH UNIVERSITY

November 2021

LOUISIANA TECH UNIVERSITY

GRADUATE SCHOOL

**September 9, 2021**

Date of dissertation defense

We hereby recommend that the dissertation prepared by

**Saif Mohammad Ishraq Bari, B.S., M.S.**

entitled **Lab-on-a-chip Thermoelectric and Solid-phase Immunodetection of  
Biochemical Analytes and Extracellular Vesicles: Experimental and Computational  
Analysis**

be accepted in partial fulfillment of the requirements for the degree of

**Doctor of Philosophy in Engineering, Micro & Nanoscale Systems Conc.**

*gergana nestorova*

Gergana Nestorova  
Supervisor of Dissertation Research

*Shengnian Wang*

Shengnian Wang  
Head of Engineering

**Doctoral Committee Members:**

Gergana Nestorova  
Shengnian Wang  
Louis Reis  
Bryant Hollins  
Chester Wilson

**Approved:**

*Hisham Hegab*

Hisham Hegab  
Dean of Engineering & Science

**Approved:**

*Ramu Ramachandran*

Ramu Ramachandran  
Dean of the Graduate School

## **ABSTRACT**

Microfluidics is the technology of controlling and manipulating fluids at the microscale. Microfluidic platforms provide precise fluidic control coupled with low sample volume and an increase in the speed of biochemical reactions. Lab-on-a-chip platforms are used for detection and quantification of biochemical analytes, capture, and characterization of various proteins, sensitive analysis of cytokines, and isolation and detection of extracellular vesicles (EVs).

This study focuses on the development of microfluidic and solid-phase capture pin platforms for the detection of cytokines, extracellular vesicles, and cell co-culture. The fabrication processes of the devices, experimental workflows, numerical analysis to identify optimal design parameters, and reproducibility studies have been discussed. Layer-by-layer assembly of polyelectrolytes has been developed to functionalize glass and stainless-steel substrates with biotin for the immobilization of streptavidin-conjugated antibodies for selective capture of cytokines or EVs. Microstructure characterization techniques (SEM, EDX, and fluorescence microscopy) have been implemented to assess the efficiency of substrate functionalization. A detailed overview of current methods for purification and analysis of EVs is discussed as well.

Additionally, the dissertation demonstrates the feasibility of a calorimetric microfluidic immunosensor with an integrated antimony-bismuth (Sb/Bi) thermopile sensor for the detection of cytokines with picomolar sensitivity. The developed platform

can be used for the universal detection of both exothermic or endothermic reactions. A three-dimensional numerical model was developed to define the critical design parameters that enhance the sensitivity of the platform. Mathematical analyses identified the optimal combinations of substrate material and dimensions that will maximize the heat transfer to the sensor.

Lab-on-a-chip cell co-culture platform with integrated pneumatic valve was designed, numerically characterized, and fabricated. This device enables the reversible separation of two cell culture chambers and serves as a tool for the effective analysis of cell-to-cell communication. Intercellular communication is mediated by extracellular vesicles. A protocol for the functionalization of stainless-steel probe with exosome-specific CD63 antibody was developed. The efficiency of the layer-by-layer deposition of polyelectrolytes and the effectiveness of biotin and streptavidin covalent bonding were characterized using fluorescent and scanning electron microscopy.

## **APPROVAL FOR SCHOLARLY DISSEMINATION**

The author grants to the Prescott Memorial Library of Louisiana Tech University the right to reproduce, by appropriate methods, upon request, any or all portions of this Thesis. It is understood that “proper request” consists of the agreement, on the part of the requesting party, that said reproduction is for his personal use and that subsequent reproduction will not occur without written approval of the author of this Thesis. Further, any portions of the Thesis used in books, papers, and other works must be appropriately referenced to this Thesis.

Finally, the author of this Thesis reserves the right to publish freely, in the literature, at any time, any or all portions of this Thesis.

Author \_\_\_\_\_

Date \_\_\_\_\_

## **DEDICATION**

*I dedicate this work to my family- my parents, wife, and brother, who always kept faith in me and constantly supported me.*

## TABLE OF CONTENTS

<b>ABSTRACT</b> .....	iii
<b>APPROVAL FOR SCHOLARLY DISSEMINATION</b> .....	v
<b>DEDICATION</b> .....	vi
<b>TABLE OF CONTENTS</b> .....	vii
<b>LIST OF TABLES</b> .....	xi
<b>LIST OF FIGURES</b> .....	xii
<b>ACKNOWLEDGMENTS</b> .....	xx
<b>CHAPTER 1 INTRODUCTION</b> .....	1
1.1    Microfluidic biosensing .....	1
1.2    Extracellular vesicles .....	2
1.3    Rationale .....	4
1.4    Objectives .....	10
1.5    Organization of the dissertation .....	10
<b>CHAPTER 2 ADVANCES IN MICROFLUIDICS FOR ON-CHIP ISOLATION AND MOLECULAR PROFILING OF EXOSOMES</b> .....	13
2.1    Background .....	13
2.2    Exosome biogenesis, molecular cargo, and current state of exosomes-based research .....	16
2.2.1    Biogenesis of exosome .....	16
2.2.2    Exosomes: carries of biological information .....	17
2.2.3    Applications and challenges of exosome-based research .....	19
2.3    Conventional methods for isolation and detection of exosomes .....	21



2.3.1	Conventional isolation techniques .....	21
2.3.2	Detection and analysis of exosomes .....	26
2.4	Microfluidics-based methods for exosomes isolation .....	28
2.4.1	The application of the microfluidics platforms in exosome research .....	28
2.4.2	Microfluidic based exosome isolation techniques .....	28
2.5	Microfluidics-based exosome detection/analysis techniques .....	40
2.5.1	Fluorescence .....	40
2.5.2	Colorimetric .....	42
2.5.3	Magnetic based methods .....	45
2.5.4	Surface plasmon resonance (SPR) .....	47
2.5.5	Electrochemical .....	49
2.6	Conclusions and discussions .....	51
<b>CHAPTER 3 DEVELOPMENT OF ANTIBODY FUNCTIONALIZED PROBE FOR SELECTIVE PURIFICATION OF EXOSOMES<sup>†</sup></b> .....		53
3.1	Background .....	53
3.2	Materials and methods .....	55
3.2.1	Design and fabrication of the ExoPRIME microprobe .....	55
3.2.2	Characterization of the microprobes to validate LbL precursor .....	56
3.2.3	Confirmation of anti-CD63 antibody immobilization .....	57
3.3	Results and discussions .....	58
3.3.1	Structural characterization of the LBL deposition on microprobe surfaces ..	58
3.3.2	Validation of the antibody immobilization using fluorescence analysis .....	60
<b>CHAPTER 4 CALORIMETRIC SANDWICH-TYPE IMMUNOSENSOR FOR QUANTIFICATION OF TNF-<math>\alpha</math><sup>†</sup></b> .....		62
4.1	Background .....	62
4.2	Materials and methods .....	64

4.2.1	Principle of calorimetric immunosensing .....	64
4.2.2	Experimental set-up .....	65
4.2.3	Fabrication of immunosensor .....	66
4.2.4	Calorimetric immunoassay procedure .....	68
4.2.5	Numerical analysis of glucose concentration as a function of the volumetric flow rate .....	69
4.3	Results and discussions.....	70
4.3.1	COMSOL simulations of the glucose concentration profile.....	70
4.3.2	Standard calibration curve .....	72
4.3.3	Stability and reproducibility study .....	74
4.3.4	TNF- $\alpha$ concentration in cell culture medium .....	75
4.4	Conclusion .....	76
<b>CHAPTER 5 NUMERICAL OPTIMIZATION OF KEY DESIGN PARAMETERS OF A THERMOELECTRIC MICROFLUIDIC SENSOR FOR ULTRASENSITIVE DETECTION OF BIOCHEMICAL ANALYTES<sup>†</sup>.....</b>		<b>77</b>
5.1	Background .....	77
5.2	Methodology .....	80
5.2.1	Numerical simulations .....	80
5.2.2	Experimental set up for thermoelectric biosensor .....	87
5.3	Results and discussions.....	88
5.3.1	Experimental validation of the numerical model.....	88
5.3.2	Effect of microfluidics channel height.....	92
5.3.3	Effect of inlets flow rate ratio .....	94
5.3.4	The relationship between material thermal properties, heat sink, and thermoelectric signal .....	96
5.4	Conclusion .....	101

<b>CHAPTER 6 NUMERICAL ANALYSIS OF OPTIMAL DESIGN PARAMETERS FOR A CELL CO-CULTURE MICROFLUIDIC PLATFORM WITH AN INTEGRATED PRESSURE-CONTROLLED VALVE<sup>†</sup></b>	<b>102</b>
6.1 Background.....	102
6.2 Materials and methodology .....	104
6.2.1 Device design.....	104
6.2.2 Numerical modeling.....	105
6.2.3 Fabrication of cell co-culture microfluidic device.....	108
6.3 Results and discussions.....	113
6.3.1 Valve displacement as a function of fluid pressure inside the pressure chamber.....	113
6.3.2 Valve displacement as a function of valve thickness and PDMS elasticity	115
6.3.3 Valve deflection as a function of various PDMS base and curing agent crosslinking ratio.....	115
6.3.4 Statistical analysis.....	119
6.4 Conclusion .....	120
<b>CHAPTER 7 CONCLUSIONS AND RECOMMENDATIONS</b>	<b>121</b>
7.1 Conclusions.....	121
7.2 Future Work.....	124
<b>APPENDIX</b> .....	<b>125</b>
<b>BIBLIOGRAPHY</b> .....	<b>131</b>

## LIST OF TABLES

<b>Table 2-1:</b> Summary of a comparative study of existing conventional exosome isolation techniques .....	24
<b>Table 4-1:</b> Microfluidics dimensions and fluid flow model parameters. ....	70
<b>Table 6-1:</b> Fluid pressure (mm-H <sub>2</sub> O) required to deflect the valve 0.5 mm for various thicknesses and PDMS base to curing agent crosslinking ratio.....	117
<b>Table A 1:</b> Area under the curve ( $\mu\text{V-s}$ ) of thermoelectric response (0-2000 pg mL <sup>-1</sup> TNF- $\alpha$ ) that were used to create the standard calibration curve. ....	126
<b>Table A 2:</b> Inter and intra-calorimetric assay variation for devices with 250 pg mL <sup>-1</sup> TNF- $\alpha$ . ....	127
<b>Table A 3:</b> Global parameters defined for model .....	128
<b>Table A 4:</b> Parameters used to define the governing equations of the mathematical model.....	129
<b>Table A 5:</b> Material properties of water, glass, PDMS, and PMMA obtained from the COMSOL library. ....	130

## LIST OF FIGURES

<b>Figure 1-1:</b> Schematic of different types of extracellular vesicles.....	3
<b>Figure 1-2:</b> Schematic of the ExoPRIME microprobe as a sensitive bioanalytical platform for solid-phase purification of exosomes. <sup>54</sup> .....	8
<b>Figure 2-1:</b> Schematic diagram of exosome biogenesis, molecular composition, and properties.....	17
<b>Figure 2-2:</b> (A) Schematic of a double-filtration microfluidic device for isolation and detection of EVs. Based on size-exclusion, particles larger than 200 nm are excluded by the membrane with a pore size of 200 nm in the sample chamber, whereas particles smaller than 30 nm pass through the double-filtration device. EVs with a size between 30 and 200 nm are isolated and enriched in the isolation chamber. (B) Image of an assembled double-filtration device. (C) Schematic of direct ELISA for EV detection on-chip. The EVs isolated in the double-filtration device is labeled with biotinylated anti-CD63 antibodies, and then with streptavidin-HRP. The addition of TMB substrate enables blue color development in the double-filtration device. (D) The ELISA result is imaged using a smartphone and then transferred to a laptop for data analysis using ImageJ. Reproduced with permission from Liang et al., 2017 under Creative Commons Attribution License (CC BY 4.0), Copyright 2017, Springer Nature.....	29
<b>Figure 2-3:</b> The nano-interfaced microfluidic exosome platform (nano-IMEX). (A) Schematic of a single-channel PDMS/glass device, with the exploded-view highlighting the coated PDMS chip containing an array of Y-shaped micro-posts. (B) The surface of the channel and micro-posts coated with graphene oxide (GO) and polydopamine (PDA) as a nanostructured interface for the sandwich ELISA of exosomes with enzymatic fluorescence signal amplification. (C) Surface protein profiling of COLO-1 cell exosomes ( $10^6 \mu\text{L}^{-1}$ ) captured by CD81 mAb. Reproduced with permission from Zhang et al., 2016 under Creative Commons Attribution Non-Commercial 3.0 Unported License, Copyright 2016, Royal Society of Chemistry. ....	31

**Figure 2-4:** A) Schematic illustration of an acoustic-based separation microfluidic chip for separation of exosomes from whole blood. RBCs, WBCs, and PTLs are removed by the cell-removal module, and then, exosomes are separated by the exosome-isolation module. B) An optical image of the integrated acoustofluidic microfluidic chip. C) The periodic distribution of pressure nodes and the trajectory of particles with different diameters in each separation module. D, E) Isolation of EVs from whole blood using the cell-removal module. The images at outlet region when acoustic waves are (D) off and (E) on. Blood cells are pushed to bottom outlets when the acoustic field is on. The white stripe in the figure indicates the centerline location of the CCD image sensor (Scale bar: 500  $\mu\text{m}$ ). Reproduced with permission from Wu et al., 2017. Copyright 2017, National Academy of Sciences. .... 33

**Figure 2-5:** Operation and layout of integrated nanoDLD chips. (a) Schematic representation of a DLD pillar array defining the gap size  $G$ , pillar pitch  $\lambda$ , and row-to-row shift  $\delta$  parameters, which determine the geometric angle,  $\theta_{\text{max}}$ , along which larger particles are deflected. Particle trajectories are illustrated for particles with diameters  $D_P$ , above (blue) and below (yellow) the critical diameter  $D_C$  which depends on the geometry of the array. (b) Tilt view optical image of the top side of a 22 mm  $\times$  30 mm nanoDLD chip, showing the sample inlet and bump outlet via positions with corresponding directional flow paths for injected sample (red) and outgoing bumped particle (blue) fluids along with a common bus network. (c) Backlit optical image of a nanoDLD chip (backside) revealing the through-hole via positions of the sample inlet (red), bump outlet (blue), and zigzag outlet via bank (yellow). (d) Optical microscope image highlighting the zoom-in section labeled in (b) with superimposed flow paths for the sample inlet (red), zigzag mode (yellow), and bump mode particle (blue) trajectories. NanoDLD arrays are paired to common zigzag outlet vias or drains, where smaller particles  $D_P < D_C$  exit to the backside of the chip into a common reservoir and larger particles  $D_P \geq D_C$  empty into a common bump outlet bus en route for the bump outlet via. Scale bar = 400  $\mu\text{m}$ . (e) Cross-sectional chip schematic illustrating the process of sample injection with zigzag and enriched, bump-particle fluid isolation and collection in common reservoirs on the backside of the chip from the different via sets. (f) Optical microscope image showing the labeled zoom-in section of (b) representing the layout of four parallel nanoDLD arrays relative to the surrounding inlet bus, filters, zigzag outlet vias, and bump outlet bus features. Scale bar = 300  $\mu\text{m}$ . (g and h) Scanning electron microscopy (SEM) image zoom-in locations of (f) along the array outlet interface indicating the direction of larger  $D_P \geq D_C$  particles bumping at  $\theta \approx \theta_{\text{max}}$  toward the bump outlet bus (g) and smaller  $D_P < D_C$  particles toward the zigzag outlet via drains (h) as they exit the array. Scale bars = 5  $\mu\text{m}$ . (i) Tilt view cross-sectional SEM image of a  $G = 225$  nm array ( $\lambda = 400$  nm) with a pillar height of 1  $\mu\text{m}$ , typical features of devices used in this study. Scale bar = 400 nm. Reproduced with permission Smith et al., 2018. Copyright 2018, Royal Society of Chemistry. .... 35

**Figure 2-6:** (i) Schematic diagram illustrates the ACE (AC electrokinetic) direct immunoassay procedure. Undiluted whole blood, plasma, or serum sample is added directly to the chip. A 10- minute application of AC current to the chip affects dielectrophoretic separation and isolation of target nanoscale extracellular vesicles (EVs) and other particulates onto the chip electrodes. Unbound material is washed off the chip with 0.5 X PBS during an additional 10 minutes of AC current. After the current is stopped, EVs and nucleic acid targets can be analyzed by different methods, including the addition of fluorescent reporter antibodies and nucleic acid dyes that are applied to the chip, then incubated for the appropriate times. Following the final wash step, the chip is ready for direct imaging and analysis of the fluorescent signal. (ii) Whole blood from a pancreatic cancer patient is glypican-1 and CD63 positive in ACE Immunoassay. Panels A-C: Whole blood drawn from a patient with PDAC was applied to an ACE chip (A); application of current caused larger whole blood cells and particulates to migrate to low-field regions between electrodes (B). A buffer wash removed most cells and particulates from the chip (C). Panels D-F: Antibodies against glypican-1 and CD63 were incubated together on the chip, followed by fluorophore-conjugated secondary antibodies for detection (D, CD63, green; E, glypican-1, red; F, brightfield image). Panels G-I: As negative controls, primary antibodies were omitted, and the fluorophore-conjugated secondary antibodies alone did not label the electrodes (G, green channel; H, red channel; I, bright field image). Reprinted (adapted) with permission from Lewis et al., 2018. Copyright 2018, American Chemical Society. .... 39

**Figure 2-7:** (i) Illustration depicting the scheme of exosomes capture and analysis procedure using ExoChip. The blood is collected for serum extraction from healthy or diseased individuals and then exosomes are captured by flowing serum through a CD63 antibody-coated ExoChip. To visualize the captured exosomes, ExoChip is processed for membrane-specific dye (DiO) staining. (ii) Experimental strategy for exosomes immobilization and characterization using ExoChip, The ExoChip is designed to measure the levels of fluorescently stained exosomes through fluorescence intensity measurements using microplate readers and allows molecular characterization of Exosomes contents through a variety of standard assays including protein analysis (western blots) and mRNA/miRNA analysis (RT-PCR/miRNA open array). (iii) A working prototype model of PDMS-based ExoChip (three channel) depicting the flow of serum for exosomes capture in a typical experimental setup. (iv) Characterization of Exosomes captured using ExoChip, A: Fluorescence microscopy image of ExoChip channel depicting immobilization of exosomes in native forms after DiO staining. High magnification (400X) images of control one of the control chambers (B) and anti-CD63 coated chambers depicting exosomes capture (C). Per the light-microscopy resolution limits the exosomes as visualized were found to be in clusters which were also confirmed through confocal microscopy. D: A confocal microscopic image showing a group of smaller exosomes (depicted as dotted circles) forming a cluster (bar = 2 $\mu$ m). The native morphology of the exosome vesicles was revealed following EM analysis. Electron micrograph images showed the absence of any vesicle immobilizations in control ExoChip (E), whereas the anti-CD63 coated ExoChip (F) showed the presence of exosomes both in clusters as well as single vesicles (bar = 500nm). G: A magnified view of a single exosome vesicle as examined under EM depicting a cluster of exosomes (bar = 100nm). Reprinted (adapted) with permission from Kanwar et al., 2014. Copyright 2014, Royal Society of Chemistry..... 41



**Figure 2-8:** Schematic illustration of the proposed aptasensor with HRP accelerated dopamine polymerization and deposition for exosome detection (ExoAptaSensor). (A) (I) Exosomes anchored on sulfate/latex beads were captured by biotin-conjugated aptamer specific to CD63, followed by incubation with streptavidin-conjugated HRP for colorimetric reaction to convert colorless Dopamine (DA) into brown-black colored Polydopamine (PDA) in 10 min in Tris buffer (pH 8.5). This oxidation and polymerization process is accelerated under HRP catalysis and hydrogen peroxide (H<sub>2</sub>O<sub>2</sub>) as the oxidant. (II) Color developed by this aptasensor correlates to exosome concentrations and allows simple naked eye visualization. (III) Absorbance signals of the product can also be quantified at 400 nm. (B) Scheme shows the poly-deposition process of PDA onto surface proteins of exosomes in situ. (C), (D), (E), (F) illustrates Proof-of-concept study of ExoAptaSensor. (C) Color intensity of PDA deposition at the target site of HRP where the concentration of H<sub>2</sub>O<sub>2</sub> varied from 0% to 2%. (D) Color intensity measured at intervals of 0, 1, 2, 10-, 20-, 30- and 60-min using ImageJ. (E) Digital images were taken right after color development of exosome samples in solution using the CD63 ExoAptaSensor. Color intensity was dependent on exosome concentrations (10<sup>10</sup>, 10<sup>8</sup>, 10<sup>6</sup>, 10<sup>3</sup>, and 0 (blank) particles, respectively). (F) Absorbance spectra were obtained at wavelengths from 300 nm to 600 nm, with a peak at 400 nm correlates with the changes in exosome concentrations. This supports the ability of the developed colorimetric aptasensor for exosome detection. Reprinted from *Development of a simple, sensitive, and selective colorimetric aptasensor for the detection of cancer-derived exosomes*, Volume 169, Xu et al., 2020a, Page No. 112576, Copyright 2020, with permission from Elsevier..... 44

**Figure 2-9:** (a) Operation principle of the coaxial mixer. (b) ELISA analysis against CD63 and CA19-9 was performed after exosome capture from whole blood. (c) Left: Image of setup. Right: The pipe is lifted from the magnets showing the NPs captured at the junctions between the alternate polarization magnets. d Simulation of the magnetic gradient created between each pair of NdFeB magnets. Nanoparticle accumulation coincides with the high-intensity nodes. The tubing is represented with solid and dashed blue lines. Reproduced with permission from Sancho-Albero et al., 2020 under Creative Commons Attribution License (CC BY 4.0), Copyright 2020, Springer Nature..... 47

**Figure 2-10:** Schematic view of SPRi in combination with antibody microarray to capture and detect exosomes in the cell culture supernatant. Antibodies specific to exosome transmembrane proteins were printed on the gilded gold chip. The optical path from the laser passes through the coupling prism at a fixed angle of incidence, and the reflection is recorded by a CCD camera. Upon injection of sample into the flow cell, exosomes can be captured by antibodies on the chip, resulting in changes in the refractive index and therefore changes in the reflection intensities, which are monitored by the CCD camera. Reproduced with permission from Zhu et al., 2014 (article link: <https://pubs.acs.org/doi/10.1021/ac5023056>), Copyright 2014, American Chemical Society. Any future use of this content is subjected to permission from ACS Publications..... 48

- Figure 2-11:** (i) Schematics of complete detachable microfluidic analysis system with electrochemical aptasensor (DeMEA) for sequential analysis of cancerous exosomes. (ii) Clinical plasma samples analysis to quantify the exosomes derived from MCF-7 cancer cells using the developed DeMEA and ELISA. The results obtained from the DeMEA and ELISA are represented in (a) bar graph, (b) scatter graph. All measurements were carried out in triplicate, and error bars correspond to standard deviations from independent measurements ( $n = 3$ ). Reprinted from *Detachables microfluidic device implemented with electrochemical aptasensor (DeMEA) for sequential analysis of cancerous exosomes*, Volume 169, Kashefi-Kheyraadi et al., 2020, Page No. 112622, Copyright 2020, with permission from Elsevier. .... 51
- Figure 3-1:** ExoPRIME probe functionalization workflow.<sup>54</sup> ..... 56
- Figure 3-2:** SEM micrographs of the tips (left panels) and stem (middle panels) of polished plain needles (A, B) and LBL-coated microneedles (D, E), showing successful and efficient deposition polyelectrolyte bilayers. The right panels show the corresponding EDX spectra of plain (C) and LBL-coated (F) microneedles.<sup>54</sup> ..... 59
- Figure 3-3:** Fluorescent images confirming successful LBL assembly and Biotin immobilization on microneedles: (A) LbL+Biotin-EDC+Streptavidin+Biotin-FITC; (B) LbL+Biotin-FITC; (C) Biotin-FITC. (D) ImageJ analysis of the CTPF of A, B, C.<sup>54</sup> ..... 61
- Figure 4-1:** Principle of calorimetric immunosensing. The amount of heat released during the enzymatic reaction between the glucose oxidase conjugated detection antibody and glucose is proportional to the concentration of TNF- $\alpha$  in the biological sample<sup>83</sup> ..... 65
- Figure 4-2:** Schematic diagram of the setup for calorimetric immunosensing of TNF- $\alpha$ <sup>83</sup> ..... 66
- Figure 4-3:** (A) Microfluidic device for calorimetric detection of TNF- $\alpha$ . (B) Image of thin-film Sb/Bi thermopile sensor. The reaction zone was located above the measuring junctions<sup>83</sup> ..... 67
- Figure 4-4:** Glucose concentration profile along the width of the microchannel. Inlet 1 velocity is  $6.7 \times 10^{-4} \text{ m s}^{-1}$ . Inlet 2 flow velocity is: (A)  $6.7 \times 10^{-4} \text{ m s}^{-1}$ ; (B)  $1.67 \times 10^{-4} \text{ m s}^{-1}$ ; (C)  $0.84 \times 10^{-4} \text{ m s}^{-1}$ . (D) Graphical representation of glucose concentration along the width of the microchannel for various velocity flow ratios<sup>83</sup>. .... 71
- Figure 4-5:** (A) Standard calibration curve for calorimetric microfluidic immunosensor. (B) Thermopile voltage output for various concentrations of synthetic TNF- $\alpha$ .<sup>83</sup> ..... 73
- Figure 4-6:** (A) Stability study for the developed calorimetric biosensor. (B) The concentration of TNF- $\alpha$  in the cell culture medium of lipopolysaccharide treated and non-treated human astrocytes were measured using conventional microplate-based ELISA and calorimetric immunosensor ( $n=4$ ).<sup>83</sup> ..... 75

- Figure 5-1:** (a) Schematic of the microfluidic device with an integrated thermoelectric sensor. Hydrodynamically focused glucose introduced through Inlet 2 flows directly above the measuring junctions of the sensor. (b) Schematic of the aluminum holder. The reference junctions of the thermopile are in contact with the aluminum block that serves as a heat sink while the measuring junctions of the thermopile and the reaction zone are position directly above the air gap.<sup>230</sup> ..... 82
- Figure 5-2:** Glucose concentration profiles and locations of the bolus injection relative to the reaction zone at 0, 40, 80, and 120 seconds. The fluid flow rates for inlet 1 and inlet 2 were  $100\mu\text{L min}^{-1}$  and  $25\mu\text{L min}^{-1}$ , respectively.<sup>230</sup> ..... 89
- Figure 5-3:** A comparison between the numerical and experimental voltage signal of the thermopile sensor. The upper and lower channel walls of the device were fabricated out of glass. The fluid flow rates for inlet 1 and inlet 2 were  $100\mu\text{L min}^{-1}$  and  $25\mu\text{L min}^{-1}$ , respectively.<sup>230</sup> ..... 90
- Figure 5-4:** Mathematical simulations of thermopile voltage output as a function of microfluidic channel height ( $T_c$ ). The upper and lower channel walls of the device were fabricated out of glass. The fluid flow rates for inlet 1 and inlet 2 were  $100\mu\text{L min}^{-1}$  and  $25\mu\text{L min}^{-1}$ , respectively.<sup>230</sup> ..... 94
- Figure 5-5:** Numerical analysis of the effect of inlet flow rate ratio on the thermopile voltage output. The channel height was  $100\mu\text{m}$  and the upper and lower channel walls were formed out of glass.<sup>230</sup> ..... 95
- Figure 5-6:** Mathematical simulation of the temperature outputs at the (a) reference junctions and (b) measuring junctions of the thermopile in the presence and absence of aluminum heat sink. Channel height  $100\mu\text{m}$ , upper and lower channel wall fabricates out of glass.<sup>230</sup> ..... 97
- Figure 5-7:** Numerical simulation of voltage output as a function of material type. The channel height was  $50\mu\text{m}$ . The fluid flow rates for inlet 1 and inlet 2 were  $100\mu\text{L min}^{-1}$  and  $25\mu\text{L min}^{-1}$ , respectively. (a) Thermopile reference junctions at ambient temperature. (b) Thermopile reference junctions in contact with a heat sink.<sup>230</sup> ..... 99
- Figure 5-8:** Effect of substrate material on voltage output obtained using the 2-D model and neglecting the lateral heat dissipation. .... 100
- Figure 6-1:** Design of microfluidics cell co-culture platform. Pressure controlled valve separates the cell chambers (A). Upon release of the pressure, the valve moved to a vertical position and allows the exchange of signaling molecules between the cell lines.<sup>241</sup> ..... 105
- Figure 6-2:** (a) Schematic of the components of the cell co-culture device. (A) hydraulic pressure chamber, (B) PDMS valve, (C) channel wall, and (D) glass; (b) Schematic and dimensions of hydraulic valve.<sup>241</sup> ..... 106

<b>Figure 6-3:</b> PDMS microfluidic cell co-culture device fabricated using replica molding. <sup>241</sup> .....	109
<b>Figure 6-4:</b> Cell-co culture device fabricated by a photolithography technique using PDMS. (A) Design of the chrome-plated photomask, (B) Pattern transferred to silicon wafer after completion of the photolithography process, (C) Solidified PDMS fabricated chips. ....	111
<b>Figure 6-5:</b> Microfluidic cell co-culture device fabricated using stereolithography method: (A) SolidWorks design for the top (yellow) and bottom (black) channel walls, (B) & (C) Images of the fabricated lower channel wall of the device with integrated supports to prevent bending. ....	112
<b>Figure 6-6:</b> Valve displacement in the vertical direction as a function of (a) pressure exerted by the fluid inside the pressure chamber, and (b) thickness of the valve. Simulations were performed for the 10:1 elastomer base to crosslinker ratio. <sup>241</sup> .....	114
<b>Figure 6-7:</b> Pressure (mm-H <sub>2</sub> O) required for 0.5mm valve deflection as a function of valve thicknesses and PDMS elasticity. <sup>241</sup> .....	115
<b>Figure 6-8:</b> Simulation of the effect of PDMS elasticity in valve defections. Analyses were performed for a device that has a 30 mm pressure chamber height, 0.5 mm thick valve, and 10:1, 20:1, 40:1, and 50:1 crosslinking ratio of PDMS base and curing agent. <sup>241</sup> .....	116
<b>Figure 6-9:</b> Surface plot of the values of the fluid pressure (mm-H <sub>2</sub> O), valve thickness, and PDMS elasticity ratio that ensures 0.5 mm displacement of the valve. <sup>241</sup> .....	119
<b>Figure A 1:</b> Temperature distribution profile at the outer surface of the lower channel wall 0, 60, and 240 seconds after the introduction of the substrate. The channel height is 50µm and the upper and lower channel walls are fabricated from glass. (i) Reference junctions not in contact with a heat sink; (ii) reference junctions in contact with the aluminum heat sink. ....	125

## **ACKNOWLEDGMENTS**

First and foremost, I would love to express my gratitude to Allah- the Almighty, and most merciful - for giving me the guidance, strength, and the ability to carry out this work. I was fortunate enough to be supervised by an amazing mentor, Dr. Gergana Nestorova, who guided and cooperated with me not only in my research but also motivated me while in distress. It would not be an exaggeration to say that she is the kind of advisor that a doctoral candidate always dreams of. I would like to express my deepest gratitude to her for being so kind to me, without which I could never complete this work successfully.

I would like to thank my advisory committee members for their careful review and valuable advice. My cordial regards to Dr. Reis who has been a co-author in several peer-reviewed articles for his amazing guidance and cooperation. I want to thank my current and former lab partners- Daniel Nwokwu, Hope Hutson, Deriesha Gaines, and Thomas Holland who were very supportive as colleagues and cordial as friends. Furthermore, I thank Mr. Davis for teaching me the operating principles of various instruments at IFM. I am very grateful to my friends, Md Tanbin Hasan Mondal, and Mohammed Al-Evan Chowdhury for helping me to learn the fabrication processes and get educated in operating numerical modeling software.

I am forever grateful to my parents and my brother whose love and prayers have always been a major source of my strength and motivation. The accomplishment will not

be fulfilled if I do not mention my lovely caring wife, who continuously motivated me even when I was not sure about finishing this journey. Without her support and care every day, it would be an unfinished story.

Finally, I want to thank the Bangladeshi student community in Ruston, who made me feel at home, loved, and cared for me like a family which has been an absolute blessing for me at a place that is a thousand miles away from home.

# **CHAPTER 1**

## **INTRODUCTION**

### **1.1 Microfluidic biosensing**

Biosensors are defined as the analytical devices or units that involve the immobilization of a biological or chemical recognition element on a physiochemical transducer to detect or quantify analytes <sup>1</sup>. Microfluidics immunosensors offer multiple advantages that include increased reaction rate, decreased time for incubation of the reactants, and reduced reagents and samples consumption. Miniaturization and integration of the multiple assay components allow automation, precise control of the fluid velocity, increased reproducibility, and the possibility for high-throughput analysis <sup>2</sup>. With these advantages, the development of microfluidic biosensors provides the ability to integrate chemical and biological components into a single platform that opens the door for biosensing applications that provide portability, real-time detection, unprecedented accuracies, and simultaneous analysis of different analytes in a single on-chip device. Recent years have witnessed significant progress in the development of more efficient detection technologies for lab-on-a-chip immunoassays that provide increased sensitivity and specificity for point-of-care application. A wide range of detection technologies has been integrated with lab-on-a-chip biosensors for the quantification of analytes in biological and chemical samples. The optimal detection method provides high sensitivity coupled with low power consumption, simple

fabrication, and minimal sample preparation <sup>3</sup>. Fluorescence, chemiluminescence, and electrochemiluminescence techniques provide detection sensitivities in the ng-pg mL<sup>-1</sup> range <sup>4</sup>. Reported limits of detection in fluorescence immunosensors include 0.7 ng mL<sup>-1</sup> for troponin T <sup>5</sup>, 0.1pg mL<sup>-1</sup> for prostate-specific antigen (PSA) <sup>6</sup> and 0.05 ng mL<sup>-1</sup> for okadaic acid <sup>7</sup>. Electrochemical immunosensors offer superior sensitivity and versatility in the choice of substrate. High-sensitive detection of PSA was achieved at 3.3 pg mL<sup>-1</sup> <sup>8</sup> and the reported limit of detection for alpha-fetoprotein was 2 pg mL<sup>-1</sup> <sup>9</sup>. Paper-based immunoassay provides a fast and cost-effective technique for detection and quantification of molecular species. Some of the applications of paper-based immunoassays include HIV <sup>10</sup> and influenza virus detection <sup>11</sup>. While these detection methods are well-established, each of these techniques has limitations. Major drawbacks of the electrochemical detection technology are the effect of external factors such as pH, temperature, and ionic concentration on the performance of the assay e.g. handling and analyses of complex solutions <sup>12</sup>. Disadvantages of fluorescent immunosensors are the requirement for high-efficiency optical filters and detectors that presents an engineering challenge in the miniaturization of the excitation and detection apparatus without significantly compromising detection sensitivity <sup>13</sup>. Although paper-based microfluidics offers enormous potential for point-of-care devices, the overall sensitivity of the device needs to be improved <sup>14</sup>.

## **1.2 Extracellular vesicles**

Intercellular communication mediates the physiological development of tissues and organs <sup>15</sup>. This occurs via direct interaction of one cell with the neighboring one or via secretion of biological or chemical substances that mediate specific responses <sup>16</sup>.



Since their discovery over three decades ago, extracellular vesicles (EV) are attracting the interest of the scientific community due to their important role in cell-to-cell communication and their potential as a source of biomarkers<sup>17,18,19</sup>. EVs contain complex cargos that include proteins, lipids, nucleic acids, and miRNAs that are released by the cells into a variety of bodily fluids, e.g., blood, urine, saliva, synovial fluid, and cerebrospinal fluid<sup>20,21</sup>. According to their biogenesis and structures, EVs are categorized as apoptotic bodies, microvesicles, and exosomes (**Figure 1-1**).

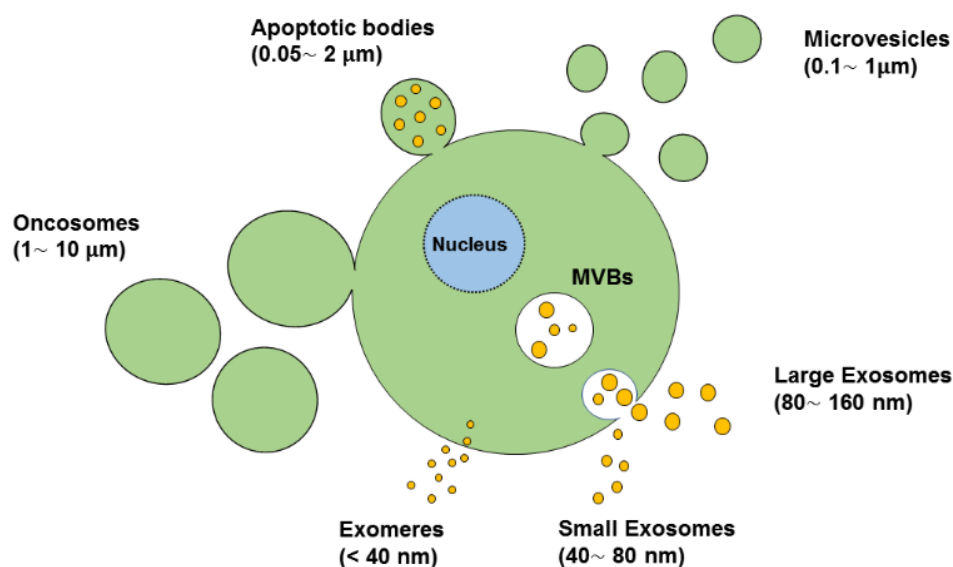


**Figure 1-1:** Schematic of different types of extracellular vesicles.

Exosomes are the smallest type of EVs (40 – 160 nm) and are released by endosomal multivesicular bodies (MVBs) via endocytic pathways<sup>22</sup>. Exosomes play a major role in cell-to-cell communication via the transfer of their cargo and influence the response of the recipient cell. Exosomal membranes are enriched in tetraspanins (CD63, CD9, and CD81) and the cargo (miRNA, protein) are used as biomarkers for disease diagnostics and prediction of therapeutic response<sup>23</sup>. Isolation and genetic analysis of

antigen-specific vesicles from the total exosome population are crucial for understanding the state of degenerating tissues that are otherwise inaccessible in the central nervous system<sup>24</sup>. Astrocyte-neuron communication is the key regulator of overall brain function, so exosomes from these cells serve as important indicators of the progression of neurological diseases in brain tissues<sup>25</sup>. The proteomic and nucleic acid cargo contained within the exosomes acts as a signal carrier that influences the physiological response of the recipient cells. They are considered a promising source of biomarkers for disease diagnosis including cancer, diabetic cardiomyopathy, arthritis, asthma, and neurodegeneration since their biological cargo reflects the pathophysiological condition of the host cell<sup>16, 26, 27, 28</sup>. Exosomes also hold massive potential as therapeutic agents due to their ability to protect nucleic acid and proteins from degradation. The explosion of new research data validates their immense potential in the areas of liquid biopsy and targeted therapeutics delivery<sup>20, 21, 22, 29</sup>.

### **1.3 Rationale**

Tumor necrosis factor- $\alpha$  (TNF- $\alpha$ ) is a cytokine that is associated with a range of pathological conditions and its biological levels are commonly measured for research and diagnostics purposes<sup>30</sup>. Increased serum level of TNF- $\alpha$  is measured in Alzheimer's disease<sup>31</sup>, cancer<sup>32</sup>, and inflammatory response<sup>33</sup>. Considering the clinical importance of TNF- $\alpha$ , its accurate and sensitive quantification in biological fluids is important for disease monitoring, diagnostics, and drug development. TNF- $\alpha$  is commonly measured using conventional immunoassays. However, tests performed in microtiter plates are time-consuming, suffer from intra- and inter-assay variations, and require multiple wash steps that are difficult to adapt in a high throughput setting. The sophisticated, expensive,

and bulky equipment and large sample volumes that are required per assay render traditional enzyme-linked immunosorbent technology unreliable for time-sensitive measurement of TNF- $\alpha$  in clinical settings<sup>34</sup>. A number of biosensors for detection of TNF- $\alpha$  have been developed that provide increased sensitivity, reduced sample volume and decreased cost per sample. Optical detection, such as fluorescence microscopy, has been employed for rapid quantification of TNF- $\alpha$  (45 pg mL<sup>-1</sup>) in serum<sup>35</sup> and cell culture medium (20 pg mL<sup>-1</sup>)<sup>36</sup>. TNF- $\alpha$  was quantified using electrochemical immunosensing in human saliva (3.1 pg mL<sup>-1</sup>)<sup>37</sup>, human serum (10pg mL<sup>-1</sup>)<sup>38</sup>, and electrochemical impedance spectroscopy (1pg mL<sup>-1</sup>) in non-diluted human serum samples<sup>39</sup>. The current lab-on-a-chip detection methods for TNF- $\alpha$  offer sensitivity, but they generally require sophisticated and bulky detection systems that cannot be readily incorporated into an integrated total analysis system. Calorimetric microfluidic systems with integrated miniaturized thermopile sensors are employed to measure small quantities of heat for biosensing applications. Since most bio-chemical reactions are accompanied by a change of heat, microfluidic calorimetry is employed in a wide range of applications. This detection method is universal and allows the measurements of reactions that are not compatible with other detection methods such as studies of single-cell metabolism<sup>40</sup>. Thermopile sensors were used to monitor the metabolic rate of bacteria<sup>41</sup>, cell culture for toxicity assessment<sup>42</sup>, DNA sequencing<sup>43</sup>, detection of enthalpy change caused by enzymatic reactions<sup>44</sup>, quantification of DNA damage<sup>42</sup>, and assessment of binding affinity<sup>45</sup>. Therefore, a calorimetric sandwich-type microfluidic immunoassay is developed and implemented for the detection and quantification of TNF- $\alpha$  using a thin-film antimony-bismuth thermopile that is attached to the lower channel wall of the

device. The sensor converts the temperature difference caused by the enzymatic reaction between glucose and glucose oxidase conjugated TNF- $\alpha$  detection antibody into an electric signal that is recorded by a nanovolt meter. The calorimetric technique can be used for the analysis of any kind of reaction that generates a measurable amount of heat. The microfluidic device requires less sample volume, the method does not need any complex sample preparation, and fabrication of expendable chips can result in reduced cross-contamination. Microfluidic calorimetry offers detection of label-free biochemical components by immobilizing the enzyme, DNA, or antibodies within a reaction area <sup>42,43</sup>.

As mentioned in section 1.2, exosomes hold massive potential as therapeutic agents, disease biomarkers, and drug delivery tools, therefore, selective capture and purification of exosomes carry great interest. All the current technologies of exosome isolation have limitations that prevent the application of exosomes in a clinical or laboratory setting, and therefore prevent the study of exosomes from reaching their full potential <sup>46</sup>. Multiple technologies that improve exosomal isolation have been developed, and the process has rapidly evolved in recent years. Methods of exosome isolation currently include ultracentrifugation and filtration, size-exclusion techniques, polymer precipitation, immunoaffinity, and microfluidics <sup>47</sup>. Most ultracentrifugation methods are coupled with filtration to increase total exosomal yield. This method can vary slightly from protocol to protocol but includes a series of ultracentrifugation steps at high speeds with long assay times. Ultracentrifugation generally has a low exosomal yield (< 5%), meaning that less than 5% of the total sample volume recovered in the final product consists of microvesicles and high rates of contamination due to tearing of the membranes and clumping <sup>48</sup>. A size-exclusion approach yields a purer exosome

subpopulation compared to ultracentrifugation because microvesicles are very small in size and the solid phase of the chromatography column removes cell lysate or other sources of contamination <sup>49</sup>. Although size-exclusion chromatography has a simpler protocol and involves more readily available equipment, it still has a low total yield (< 8%) and is a nonspecific capture method <sup>47</sup>. Polymer precipitation is the most common approach to exosome isolation. It requires little equipment, encompasses a simple protocol, and provides a relatively high total product yield (> 25%). This method, however, can only process a very small sample volume, has a long assay time (8 h or more), and carries the risk of compromising the structural integrity of the microvesicles isolated <sup>50</sup>. Immunoaffinity techniques largely involve the use of antibody-coated beads which are specific to the membrane proteins embedded in the lipid membrane of the exosomes and the approach can be used in almost any biological media. This method is highly specific and has a high total yield and purity at the time of capture (>99%). However, immunoaffinity capture-based techniques require additional exosomal enrichment step that is usually done by ultracentrifugation, polymer-precipitation, or size-exclusion chromatography <sup>47</sup>. Microfluidics strategies for exosome isolation integrate on a lab-on-a-chip platform already established purification methods including size-exclusion chromatography <sup>51</sup> and immunoaffinity <sup>52</sup>. The main goals of these techniques are target-specific capture while reducing contamination rates and increasing the total product yield. This method, however, has no standardized protocol and yields a variety of experimental results <sup>53</sup>.

To overcome various difficulties observed in traditional exosome purification technologies, a novel microprobe-based method has been developed for noninvasive and

site-specific exosome purification and genetic analysis. Stainless-steel exosome capture pins ( $130\ \mu\text{m} \times 4\ \text{mm}$ ) are functionalized with an anti-CD63 antibody that selectively binds to the corresponding tetraspanin (**Figure 1-2**). The technology is expected to have an important impact in the field of extracellular vesicle research as this immunocapture approach will enable selective purification of exosomes and will allow direct integration with standard systems for genomic analysis. A microprobe-based approach to exosome isolation eliminates the need for large, expensive equipment in the protocol and creates an affordable platform that is widely accessible by scientific and medical facilities. Microneedles are noninvasive and are therefore a preferred method of laboratory testing from a medical standpoint. This approach will reduce the lengthy, multistep procedures which currently encompass exosome isolation down to a single step.

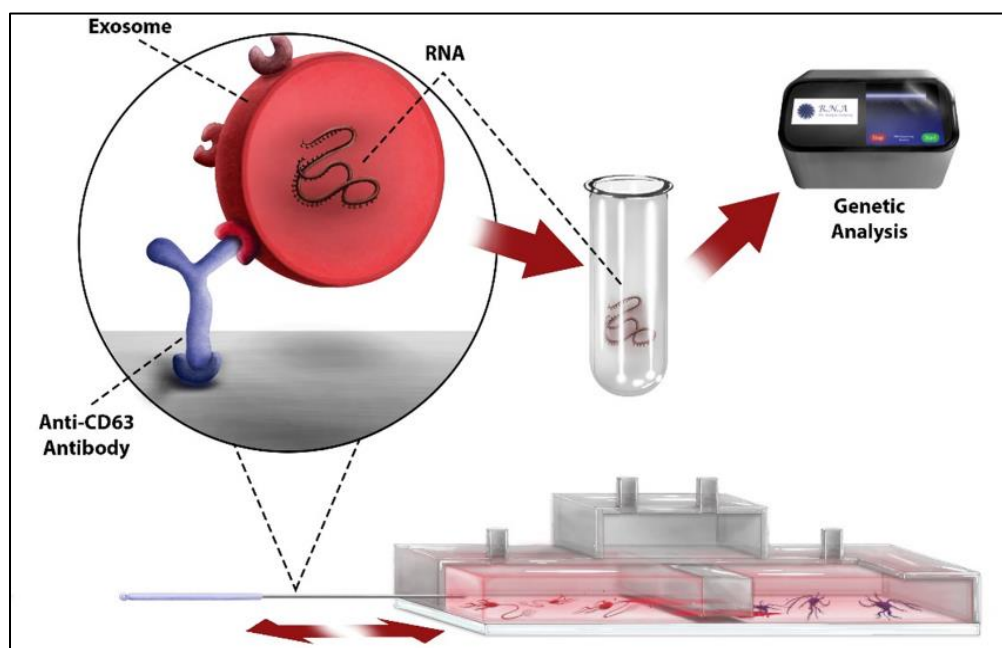


**Figure 1-2:** Schematic of the ExoPRIME microprobe as a sensitive bioanalytical platform for solid-phase purification of exosomes.<sup>54</sup>

Another important rationale of this work is to develop a microfluidic technology for the analysis of cell-to-cell and cell-extracellular matrix interactions is an important topic in biomedical engineering research. While conventional cell co-culture approaches, such as transwell-type co-culture plates, are successfully used for functional analysis of cell-to-cell communications, this technology does not permit a controlled exchange of fluids between two cell culture chambers <sup>55</sup>. Lab-on-a-chip platforms enable a real-time, on-chip analysis of the interaction between cells and their microenvironments. Microfluidics provides flexibility in the device design and better control of the experimental conditions that facilitate drug discovery studies <sup>56</sup>. Cell co-culture microdevices with an integrated valve enable precise control of the exchange of biochemical factors while minimizing sample variability and enhancing the sensitivity of the analysis <sup>57</sup>. Therefore, an innovative microfluidic cell co-culture platform with a pneumatically controlled valve has been reported. Additionally, various design parameters have been optimized using a numerical model developed in COMSOL Multiphysics to observe the valve deflection and the isolation of the two chambers. The proposed microfluidics platform offers a promising new tool for the assessment and characterization of the complex interaction of different cell types.

## **1.4 Objectives**

The main objectives of the study are summarized below:

- Experimental and numerical characterization of a microfluidic platform for thermoelectric immunodetection of biochemical analytes.
- Development of a cell co-culture microfluidic platform with and without a pneumatically controlled valve. Efforts are focused on fabrication using

3D printing and soft-lithography, and mathematical modeling to identify optimal design parameters.

- Demonstrate the feasibility of exosomes specific anti-CD63 antibody on the surface of stainless-steel microprobes for purification of exosomes.

## 1.5 Organization of the dissertation

The studies are organized in this dissertation as five standalone articles (four of them are already published as peer-reviewed journals and conference papers). Chapters 2 through 6 each represent one article, and chapter 7 is the overall summary of the findings and suggestions for future studies.

A literature review on the advancements in exosome isolation and analysis methods from various biological fluids is reported in chapter 2. The advantages and disadvantages of existing methods for isolation and detection methods of the exosomes and other extracellular vesicles are summarized. The applications of microfluidics in exosome isolation and analysis, their respective advantages and disadvantages have been presented. This chapter is currently under preparation for submission as a review article.

In chapter 3, the preparation and functionalization of stainless-steel microprobes with CD63 antibody is described for isolation of exosome subpopulations that express the same surface marker. The efficiency of the probe functionalization with polyelectrolytes and biotin was assessed using FESEM and fluorescence microscopy. This work is included in a journal article published in *Talanta* (*Elsevier*, *IF*: 6.057).

In chapter 4, a lab-on-a-chip thermoelectric immunoassay is reported for sensitive quantification of the inflammatory cytokine TNF- $\alpha$  with picomolar sensitivity. The feasibility of the platform was validated via accurate measurement of the concentration of



TNF-  $\alpha$  in astrocytes cell culture media. The immunoassay was performed in a microfluidic device with an integrated antimony/bismuth thermopile sensor. This novel immunosensing platform presented excellent accuracy along with other certain advantages of the microfluidic platform when compared to the commercially available absorbance-based ELISA method. This chapter was published in *Biosensors and Bioelectronics (Elsevier, IF: 10.618)*.

A three-dimensional numerical model of the microfluidic calorimetric immunosensor presented in chapter 4 is developed and analyzed to determine the effects of the operational parameters, geometry, and choice of the substrate materials on device sensitivity. This study is reported in chapter 5 along with the detailed numerical modeling obtained using COMSOL Multiphysics software. This numerical model was published in the *Journal of Thermal Science and Engineering Applications (ASME, IF: 1.47)*.

Chapter 6 discusses the design and parameters optimization of a microfluidic co-culture platform with an integrated pneumatic valve. This study includes the fabrication of microfluidic devices using three different microfabrication processes: replica molding, photolithography, and stereolithography. A 2-D numerical analysis is performed to identify the optimal design parameters to study the impacts of the height of the pressure chamber, the thickness of the valve, and the elasticity of the PDMS elastomer on the efficiency of the valve actuation. These results have been published in the *Conference proceedings of the International Mechanical Engineering Congress and Exposition (ASME IMECE 2020)*.

Chapter 7 summarizes the important conclusions and recommendations for future studies.

## CHAPTER 2

### ADVANCES IN MICROFLUIDICS FOR ON-CHIP ISOLATION AND MOLECULAR PROFILING OF EXOSOMES

#### 2.1 Background

Intercellular communication mediates the physiological development of tissues and organs <sup>15</sup>. This occurs via direct interaction of the cell with the neighboring one or via secretion of biological or chemical substances that mediate specific responses <sup>16</sup>. Since their discovery over three decades ago, EVs are attracting the interest of the scientific community due to their important role in cell-to-cell communication and their potential as a source of biomarkers <sup>17,19,58</sup>. EVs contain complex cargos that include proteins, lipids, nucleic acids, and miRNAs that are released by the cells into a variety of biological fluids, including blood, urine, saliva, synovial fluid, and cerebrospinal fluid <sup>20,59</sup>. According to their biogenesis and structures, EVs are categorized as apoptotic bodies, microvesicles, and exosomes (**Figure 1-1**). Exosomes are the smallest type of EVs (40 – 160 nm) and are released by endosomal multivesicular bodies (MVBs) via endocytic pathways <sup>22</sup>. The proteomic and nucleic acid cargo contained within the exosomes acts as a signal carrier that fuses with and influences the physiological response of the recipient cells. They are considered a promising source of biomarkers for disease diagnosis including cancer, diabetic cardiomyopathy, arthritis, asthma, and neurodegeneration since their biological cargo reflects the pathophysiological condition

of the host cell <sup>16,26,28,60</sup>. Exosomes also hold massive potential as therapeutic agents as well due to their ability to protect nucleic acid and proteins from degradation. The explosion of new research data validates their immense potential in the areas of liquid biopsy and targeted therapeutics delivery <sup>20,22,29,59</sup>.

The protein contents in exosomes include transmembrane proteins, lysosome-derived membrane proteins, E-cadherin, membrane-associated proteins, GTPases, heat shock proteins, lipid-related proteins, phospholipases, tetraspanins, and proteins associated with the multivesicular body (MVs) biogenesis <sup>61–64</sup>. Multiple studies suggest that proteomic analysis of exosomes provides critical information that can assist early detection and diagnosis of cancer, metabolic diseases, neurological disorders, and immune regulation <sup>65</sup>. Therefore, isolation of pure exosomal subpopulation from a biological fluid is crucially important to determine their pathophysiological functions. Current methods for exosomes isolation include ultracentrifugation <sup>66</sup>, size-exclusion chromatography <sup>67</sup>, ultrafiltration <sup>68</sup>, polymer-based precipitation <sup>69</sup>, and immunoaffinity capture <sup>70</sup>. This review provides a detailed discussion of the barriers in conventional exosome isolation and detection techniques and the most recent advancements and challenges in microfluidics-based methods for purification and on-chip detection of exosomes.

Several detection techniques have been employed for the analysis, size characterization, and molecular profiling of different exosomal subpopulations. Flow cytometry <sup>71</sup>, Scanning electron microscopy (SEM) <sup>72</sup>, transmission electron microscopy (TEM) <sup>73</sup>, dynamic light scattering (DLS) <sup>74</sup>, atomic force microscopy (AFM) <sup>75</sup>, enzyme-linked immunosorbent assay (ELISA) <sup>76</sup>, and nanoparticle tracking analysis (NTA) <sup>77</sup> are

commonly used in both clinical and research settings. The drawbacks of this method are the need to use expensive and complex equipment that limits the access of many labs to this type of analysis <sup>16</sup>.

To address the challenges of conventional technologies for the isolation and detection of exosomes, microfluidic platforms offer a promising approach for the efficient purification and molecular characterization of EVs. Microfluidic technology requires low sample volume and minimal consumption of expensive reagents. The dimensions of the microchip provide a high surface-to-volume ratio that enhances the reaction rate within the microchannels. Moreover, the lab-on-a-chip methods provide a fast, simple, highly sensitive, and cost-effective way for the isolation of exosomes compared to the conventional commercially available technologies <sup>16,78</sup>. Due to these tremendous characteristics, microfluidics has been implemented in cell analysis <sup>79,80</sup>, point-of-care diagnostics <sup>81,82</sup>, sensitive detection of biochemical analytes <sup>83</sup>, and molecular analysis <sup>84</sup>. The preparation of a pure exosomal population is crucial for the development of point-of-care tests for disease diagnosis and novel therapeutic agents <sup>65,85–87</sup>. In microfluidic devices, exosomes are mainly isolated based on the particle size <sup>88</sup>, immunoaffinity <sup>89</sup>, or electrical charge <sup>90</sup>, and the efficacy of separation can be increased by applying external hydrodynamic force <sup>91</sup>, acoustic field <sup>92</sup>, or electrical field <sup>93</sup>.

## 2.2 Exosome biogenesis, molecular cargo, and current state of exosomes-based research

### 2.2.1 Biogenesis of exosome

The exosomes were described initially as clusters of endosome-derived nanovesicles that are released into the extracellular microenvironment<sup>94</sup>. The biogenesis of exosomes starts in early endosomes (**Figure 2-1**). Matured or late-endosomes move to the cytoplasm, change their tube-like shape into spherical, and form the multivesicular bodies (MVBs). Inward budding results in the progressive accumulation of intraluminal vesicles (ILVs) inside the MVP. The development of the multivesicular endosomes can follow either of the following pathways<sup>16</sup>.

- MVBs fuse with lysosomes and degrade their content.
- MVBs fuse with the plasma membrane and release their content in the extracellular space.

For the first type, the MVBs are being hydrolyzed by the lysosomes. In the case of the second instance, the MVBs tend to fuse with the plasma membrane and release ILVs into the microenvironment. Once the ILVs are released into the extracellular space, they are called exosomes<sup>95</sup>. Studies indicated that the formation of ILVs and the process of exosome release are mediated by tetraspanins (CD9, CD63, CD81), glycan modification, and Rab guanosine triphosphatases (RAB 27A, RAB 27B, RAB 31, and RAB 11)<sup>16,29,96,97</sup>. The complex underlying biology of exosomes formation and what factors govern the transition of the MVBs to the exocytic pathway or the degradative pathway remain to be further characterized<sup>98</sup>.

### 2.2.2 Exosomes: carries of biological information

Exosomes contain a diverse cargo that includes proteins, DNA, mRNA, non-coding RNA, tRNA, and lipids <sup>16</sup>. The proteins are derived from various intracellular components such as MVBs, nuclei, mitochondria, cytosol, plasma membranes, and Golgi bodies <sup>29</sup>. Vesiclepedia and ExoCarta are databases used to catalog the protein content of exosomes from many organisms and cell types <sup>99</sup>. The main drawback of these databases is the lack of verification as all the information is recorded by the users. Therefore, several researchers have reviewed the protein contents of exosomes <sup>100,101</sup>. To summarize the literature, the proteins are mainly characterized as exosomal marker proteins (TSG101, HSP90 $\beta$ , HSC70, Alix), common proteins (CD9, CD63, CD81, CD82), and specific proteins (EpCAM) <sup>16,47</sup>. The exosomal marker proteins are found in the exosomes regardless of the cell origin due to their formation and regulation via the proteins carried by the endosomal sorting complexes required for transport (ESCRT) <sup>102,103</sup>. The common proteins (also known as the transmembrane proteins) belong to the tetraspanin family and are enriched with exosomes <sup>104</sup>. However, the tetraspanin proteins are also available in MVs and apoptotic bodies <sup>105</sup>. The specific protein, such as the epithelial cell adhesion molecule (EpCAM), is found in cancer-derived exosomes. EpCAM is a glycoprotein that expedites the homo-typical adhesion of cells. EpCAM has been identified in pseudo-stratified, transitional, and simple epithelia on the basolateral surfaces and recognized as a cargo protein in exosomes <sup>106</sup>. EpCAM is quantified to a certain degree in the normal epithelia of many organs and is highly overquantified in various types of carcinomas <sup>107</sup>. In addition to the protein contents, miRNA, mRNA, tRNA, nucleic acids, DNA, and lipids have also been identified in

exosomes<sup>108–114</sup>. The lipid contents in exosomes include saturated fatty acids, cholesterol, sphingomyelin, and phosphatidylserine<sup>115</sup>.

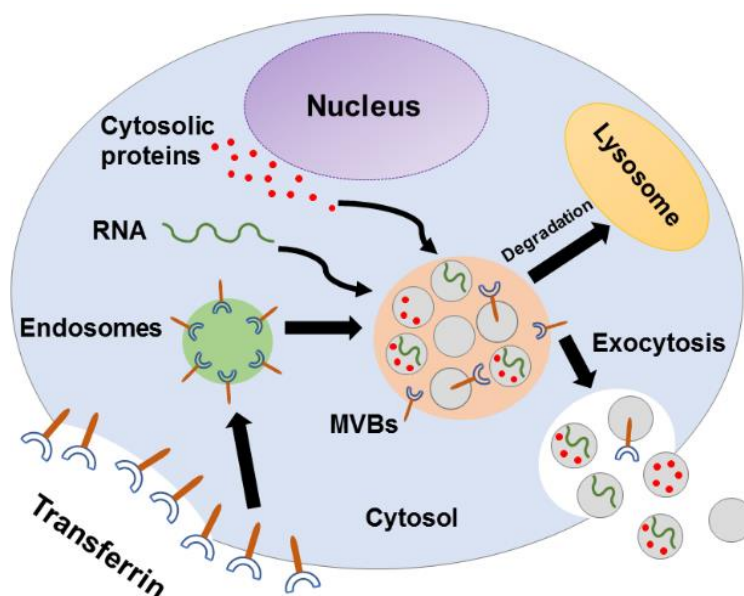


**Figure 2-1:** Schematic diagram of exosome biogenesis, molecular composition, and properties.

Exosomes play a crucial role in intercellular communication that is based on the exchange of genetic information between the donor and the recipient cells<sup>94</sup>. The genomic and proteomic expression levels of the exosomal cargo are altered in various pathophysiological conditions. Exosomes alter the tumor microenvironments of tumors by facilitating metastasis and influence the response of the cells of the immune system<sup>116</sup>. In addition to that, exosomes also take part in central nervous system communications in various pathophysiological conditions such as glioblastoma<sup>117</sup>. The composition of the vesicle membrane reflects the pathological condition of the parent cell and can be used as a biomarker for the detection of malignancies<sup>96</sup>. Over the last decade, there has been a growing interest in exosomes in the area of biotechnology. Exosomes hold huge potential as disease biomarkers for clinical diagnosis provided by the ease of access from a variety

of biological fluids and their cell-specificity. These EVs are potential tools for drug delivery due to their specificity and low immunogenic potential <sup>94</sup>.

### 2.2.3 Applications and challenges of exosome-based research

Exosomes contribute to the development of several pathological processes suggesting that they have the potential to serve as diagnostic biomarkers and therapeutic agents. Urinary exosomes contain cargoes such as miRNA29, mRNA, Aquaporin-2, and antimicrobial urinary tract proteins that can be used as biomarkers to diagnose renal fibrosis, diabetes mellitus, and urinary tract infection <sup>118–120</sup>. Exosomes released by uteroplacental (maternal-placental) contain hsa-miRNA-210 that can perform early detection of preeclampsia <sup>121</sup>. In this study, the authors found that the level of hsa-miR-210 was significantly higher in preeclampsia placentas, which could cause a minor increase of exosomal and a high elevation of Ago-bound miR-210 in circulation. Another study found the potential of the exosomal amyloid peptides and tau proteins as the biomarkers for Alzheimer's patients <sup>122</sup>. Tetraspanins expressed on the surface of exosomes released from tumor sites (CD9, CD63) can be used for the prognosis of the survival rate <sup>123</sup>. Exosomes reflect the physiological state of the donor cell and therefore demonstrate superior target sensitivity and specificity compared to other categories of biomarkers such as genomic and proteomic expression biomarkers <sup>22</sup>. Exosomes are promising nanocarriers for targeted drug delivery. Their cell-derived lipid bilayer is biocompatible and can deliver endogenous biological cargo to the recipient cell <sup>124</sup>. Since exosomes are derived from the patient's cells, they are not recognized and degraded by the immune system and have low toxicity <sup>125</sup>. Exosome-based drug delivery systems have been used across the blood-brain barrier for the treatment of neurodegenerative



disorders <sup>126</sup>. Chen et al. studied the effect of bone marrow mesenchymal stem cell (BMSC)-derived exosomes carrying miRNA-125b on ischemia-reperfusion injury (I/R) rats, where the researchers examined that the BMSC-derived exosomes carrying miRNA-125b protect against myocardial I/R by targeting SIRT7 and potentially can serve as a therapeutic method for myocardial I/R <sup>91</sup>. Another study revealed that mesenchymal stromal cells inhibit *in vitro* tumor growth when they were primed with paclitaxel (PTX), and later released in exosomes <sup>127</sup>. Kim et al. reported that the macrophage-derived exosomes loaded with potent anticancer agent paclitaxel (PTX) represent a novel nanoformulation (exoPTX) that showed superior anticancer efficiency in a mouse model of pulmonary metastases. The researchers developed and optimized an expression of PTX-loaded exosomes combined with aminoethylanisamide-polyethylene glycol (AA-PEG) to target the sigma receptor- a biomarker that is overexpressed by lung cancer cells. The AA-PEG-vectorized exosomes primed with PTX (AA-PEG-exoPTX) attained a high loading capacity, intensified ability to accumulate in cancer cells upon systemic administration, and improved therapeutic outcomes, which offers a potentially novel drug delivery platform for anticancer therapeutics for pulmonary metastasis <sup>128</sup>.

The most important requirement for the development of exosome-based diagnostic and drug delivery platforms is the development of rapid and specific exosome isolation techniques. It is often very difficult to apply a high-throughput process for their separation due to the inconsistencies in content and cell-specific uniqueness of exosomes. Current methods for exosomes separation do not produce a pure exosomal population and are often contaminated with other types of extracellular vesicles, proteins, and cellular debris. Additionally, they do not yield a population of exosomes that carry the same

surface marker, a requirement that is crucial to explore their full potential as clinical biomarkers. For example, the cerebrospinal fluid contains exosomes that carry vital information about the function of the central nervous system, and methods for purification that can noninvasively access and preconcentrate the vesicles would provide a major drive for the diagnosis of neurological disorders. Therefore, the development of a highly selective method for exosome separation is crucial for exosome-based research.

## **2.3 Conventional methods for isolation and detection of exosomes**

The main methods for exosomes isolation are based on the properties of the vesicles such as size, protein surface markers, and density. To focus more on the recent development of microfluidic technologies, this review will briefly summarize each conventional method for exosomes characterization and their drawbacks in the following sections.

### **2.3.1 Conventional isolation techniques**

#### **2.3.1.1 Ultracentrifugation**

The centrifugation technique separates biomolecules according to their size difference. Ultracentrifugation and differential centrifugation are considered the gold standard for exosome isolation <sup>65</sup>. Centrifugation at lower speed is applied to isolate larger vesicles and cellular debris (< 20,000 g) that is followed by ultracentrifugation (> 100,000 g) to separate exosomes from protein contaminants <sup>20</sup>. The ultracentrifugation method does not require sample pre-treatment and is the most common method in exosomes research accounting for 56% of all published papers in the literature <sup>129,130</sup>. The major drawbacks of this method are the requirement for special centrifugation

instruments coupled with low purity, poor repeatability, and lengthy protocols <sup>20,22</sup>.

Differential centrifugation has low exosome isolation efficiency (5 - 25%) and purity caused by contamination with protein aggregates <sup>131</sup>.

#### 2.3.1.2 Immunoaffinity-capture

Immunoaffinity-based separation of exosomes is based on the expression of a specific surface marker on the surface of the vesicles. An antibody immobilized on the surface of a platform is used for the selective capture of the exosomal subpopulation via antigen-antibody interaction. The most commonly used markers are the tetraspanins CD9, CD63, CD81, and CD82. Some recent accomplishments in exosome separation from bodily fluids are achieved by the immunoaffinity-based isolation method are presented in the literature <sup>132–134</sup>. The immunoaffinity-based isolation technique offers a high yield and purity, time-effectiveness and does not require special equipment <sup>135</sup>. Zarovni et al. have shown that antibody-based separation of exosomes provides 10 – 15 times better yield compared to the ultracentrifugation method. Isolation kits based on immunoaffinity-based separation are commercially available (e.g., ExoFACS™) <sup>136</sup>. However, this isolation technique is viable for exosome subpopulations with recognized biomarkers and cannot be used for all types of exosomes. Moreover, expensive reagents, and maintaining strict pH conditions also interfere with the application of this approach for large-scale exosome isolation <sup>16</sup>.

#### 2.3.1.3 Ultrafiltration

Ultrafiltration is one of the widely used size-based exosome isolation techniques that rely on particle size and molecular weight <sup>137</sup>. In this method, suspended solids and solutes of high molecular weight are trapped by the membrane while lower molecular

weight solutes and water pass through. Studies indicate that the ultrafiltration method is often combined with the ultracentrifugation method to obtain high purity of exosomes<sup>138,139</sup>. To describe the combined process more precisely, ultrafiltration is implemented to isolate large cells and EVs followed by an ultracentrifugation process to purify exosomes from proteins. The ultrafiltration separation technique has been employed to separate highly pure exosomes from urine samples<sup>140</sup>. Several other research groups have explored commercially available ultrafiltration-based exosome isolation kits (e.g. Amicon filter, and ExoMir) for successful isolation of exosomes from protein contaminants<sup>20,131</sup>. This size-based method carries multiple advantages over the widely used ultracentrifugation process such as a fast and simple process and no stipulation of using specific equipment. However, clogging and trapping of exosomes in the filters result in a low yield<sup>137</sup>. Although this problem can be resolved to some extent by washing the filters after each step, this can be time-consuming. Furthermore, the force exerted on the sample to propel through the filters may cause the deformation of the larger exosomes that results in distorting the isolation process<sup>141</sup>.

#### 2.3.1.4 Size-exclusion chromatography (SEC)

This size-based isolation technique is based on a conventional chromatography approach with a specially selected porous stationary phase which is often combined with ultracentrifugation or filtration methods for isolating exosomes from bodily fluids or proteins. Unlike the ultrafiltration method, SEC uses commercially available size-exclusion columns for the isolation technique. Before flowing through the column, large EVs and cell debris are separated by either ultrafiltration or ultracentrifugation. Commercially available size-exclusion columns are employed to isolate exosomes<sup>67,142</sup>.

One of the biggest advantages of SEC is its ability to sustain biological activity and integrity due to the means of gravitational force being used for isolation. However, ultracentrifugation is commonly used with SEC to obtain better purity of the isolate<sup>143,144</sup>. There are a variety of commercially available SEC-based kits that provide high purity, but their expensive price limits their application in the wide-scale separation process.

#### 2.3.1.5 Polymer-based precipitation

The precipitation-based exosome isolation technique is carried out by using a precipitation reagent to modify the solubility of exosomes. These reagents create exosome-containing residues for retrieval of exosomes using membrane filtration or standard centrifugation (~ 10,000 g). This is a relatively easy, instrument-free method where hydrophobicity of the exosomal membrane is utilized. Moreover, the polymer-based precipitation method provides a highly reproducible technique for high vesicles and RNA yield<sup>46</sup>. Various commercial precipitation-based exosomes separation kits are available on the market (e.g., Exo-spin<sup>TM</sup>, Exo-Quick<sup>TM</sup>, Total Exosome Isolation Reagent by Invitrogen<sup>TM</sup>, Exo-S, Exo-Q, and miRCURY<sup>TM</sup>). These commercial kits provide very good efficacy for low volume of the biofluids from serum, plasma, and cerebrospinal fluids (CSF)<sup>145</sup>. The critical drawback of this approach is that the precipitation reagents enable exosomal aggregation and co-precipitation of proteins<sup>20</sup>. Other disadvantages of precipitation-based separation include the high cost of the consumables, low specificity, and poor yield.

**Table 2-1:** Summary of a comparative study of existing conventional exosome isolation techniques

Isolation technique	Isolation principle	Parameters			Advantages	Disadvantages	Ref.
		Time	Yield	Purity			
Ultracentrifugation	Density-based	*	*	**	The gold standard, highly pure	Time-consuming (~5 h); low yield and purity; large sample volume required	65,146
Immunoaffinity-capture	Affinity-based	**	**	***	Highly specific and pure	Expensive; strict pH condition; constrained use	133,134
Size-exclusion chromatography	Size and molecular weight	**	**	**	Simple, rapid, high yield	Poor specificity; scaling problems	67,142,144
Polymer-based precipitation	Surface charge-based	**	***	**	Simple and user-friendly	Expensive; low specificity; poor purity; scaling problems	47,145
Ultrafiltration	Molecular weight and size-based	**	**	**	Rapid, simple, no specific instrument	Clogging; low yield, low specificity, time-consuming	138–141

Appraisal parameters are categorized by \*\*\*, \*\*, and \* imply very good, moderate, and poor performances respectively.

### 2.3.2 Detection and analysis of exosomes

#### 2.3.2.1 Flow cytometry

Flow cytometry is a widely used conventional detection method for detecting a large amount of EVs. The technique enables high throughput multiplex analysis of exosomal surface markers<sup>147</sup>. This detection technique is based on laser-based detection of fluorescence-labeled exosomes. A dedicated detector captures the resulting signal that is comprised of the emitted fluorescence and scattered light. Despite its advantages, the use of flow cytometry in exosome analysis is often avoided due to its low sensitivity and resolution<sup>148</sup>. To overcome the difficulties of this method, scientists have implemented a special type of flow cytometry, known as fluorescence-activated cell sorting (FACS), where the suspended exosomes are separated according to their specific and distinct fluorescence features<sup>149</sup>. Recent studies in the literature have shown the enactment of FACS for exosome analysis<sup>150–152</sup>. However, FACS requires sophisticated instruments which often may not be readily available and thus halts its ability to be implemented in lab-like low-resourceful settings<sup>22</sup>.

#### 2.3.2.2 ELISA

Enzyme-linked immunosorbent assay (ELISA) is a technique that uses labeled antibodies to measure the protein of interest in a biological sample. In a traditional format, the exosomes adhere to the surface of a 96-well plate. A primary antibody that is specific to the exosomal surface protein marker is introduced into the well to form an antigen-antibody complex with the exosomes. A secondary antibody labeled with an enzyme binds with the primary antibody and an enzyme-generated colorimetric signal is measured by a plate reader<sup>153</sup>. ELISA is one of the most commonly used techniques for

the detection of EVs due to the requirement of a very low sample volume <sup>154</sup>. In recent years, digital ELISA kits have emerged which offer immaculate sensitivity for a low volume of samples <sup>155,156</sup>.

#### 2.3.2.3 Tunable resistive pulse sensing (TRPS)

Tunable resistive pulse sensing (TRPS) is based on the principle that the movement of the non-conductive components in an electrolyte solution can cause a change in the electrical impedance vis-à-vis particle concentration, surface charge, and size of the particles <sup>157</sup>. This phenomenon is also known as the Coulter principle. TRPS offers great accuracy in determining the size, concentration, and surface charge of exosomes by determining the change in impedance or using a resistive pulse signal <sup>158,159</sup>.

#### 2.3.2.4 Dynamic light scattering (DLS) and nanoparticle tracking analysis (NTA)

Both DLS and NTA approaches are based on the Brownian motion principle to measure the size and concentration of the nanoparticles <sup>160</sup>. While the DLS method analyzes the relative change in the intensity of the scattered light induced by the Brownian motion of the bulk samples of suspended nanoparticles e.g., exosomes, NTA implements the Stokes-Einstein equation to calculate the hydrodynamic diameter of each nano component <sup>161,162</sup>. Due to their capabilities to discern nanoparticles of various sizes ranging from 1 to 1000 nm, both DLS and NTA have been widely used for the detection and analysis of exosomes. However, low throughput and inaccuracy of the results often create issues for heterogeneous samples that are prone to aggregation <sup>160</sup>.

All the isolation and detection techniques of the exosomes discussed above have been successfully implemented for the detection and characterization of exosomes. There are a few drawbacks of these conventional techniques which include the requirements of



sophisticated instruments, implementation of separate techniques for isolation and analysis, the isolation of non-specific exosomes, and EVs <sup>163</sup>. All these difficulties have made it challenging to implement these isolation and detection techniques as diagnostic tools in clinical settings.

## **2.4 Microfluidics-based methods for exosomes isolation**

### **2.4.1 The application of the microfluidics platforms in exosome research**

Recent years have witnessed the emergence of microfluidics for capturing and analysis of the EVs including exosomes from various bodily fluids by successfully resolving the issues associated with the conventional methods. Microfluidics offers multiple advantages over the conventional techniques that include low sample volume for precious samples, the ability for multiplexing, cost-effectiveness, and the integration of sensors that provide precise control over the fluid <sup>164,165</sup>. Lab-on-a-chip technology has a high potential for clinical applications due to throughput, reduced cross-contamination, and combined technique for an exosomes isolation-detection process <sup>166</sup>. The following sections will summarize currently available microfluidics-based approaches for exosome isolation and detection.

### **2.4.2 Microfluidic based exosome isolation techniques**

#### **2.4.2.1 Filtration**

In microfluidic technology, filtration is one of the commonly used reagent-free methods for the separation of exosomes from various biofluids. Filtration is performed by using nanoporous membranes or nanopillar arrays incorporated in a microfluidic device <sup>78</sup>. Membrane-based filtration of extracellular vesicles from a blood sample using

microscale technology was first successfully demonstrated by Davies et al. Pressure-driven and electrophoresis-driven filtration were performed using an *in situ* prepared nanoporous membrane using a mouse's whole blood sample. This approach demonstrated an isolation capacity of 3  $\mu\text{L}$  and 240  $\mu\text{L}$ , respectively, with a recovery yield of  $\sim 1.5\%$  in both cases <sup>167</sup>. However, the microfluidic device clogged after the extraction of 4  $\mu\text{L}$  filtrate, which was resolved by the electrophoresis method that provides higher purity and better throughput. Electrophoresis-driven filtration was also implemented by Cho et al. to isolate extracellular vesicles from mouse plasma. The authors developed a process to separate proteins using a dialysis membrane which also trapped the EVs on the membrane surface. This process provided a better throughput, higher yield, and fewer protein impurities ( $\sim 84\%$  compared to ultracentrifugation) <sup>93</sup>. With the development of microfluidics in exosome research, scientists have implemented an advanced double-filtration technique to isolate exosomes from urinary samples where the membrane with a larger pore size ( $\sim 200\text{ nm}$ ) was used to retain large EVs and protein samples whereas small EVs were trapped on the second membrane surface (pore size  $\sim 30\text{ nm}$ ) while smaller proteins passed through <sup>168</sup> (**Figure 2-2**). This double filtration approach was also implemented on a "lab-on-a-disc" Exodisc method, which produced high throughput and recovery yield as well as lowered the protein impurities ( $\sim 96\%$  compared to ultracentrifugation) <sup>88</sup>. Pillar-based filtration is another method of isolating exosomes that incorporates one or more arrays of pillar-based structures to migrate larger molecules and isolate exosomes using a reversed flow. This technique has been implemented for the isolation of exosomes from biofluids with fast processing time ( $\sim 10\text{ min}$ ) and good yield ( $\sim 60\%$ ) <sup>169,170</sup>. However, the recovery yield gradually decreases with larger sample

volumes which are considered as the saturation effect<sup>78</sup>. Moreover, this process requires off-chip downstream analysis to isolate exosomes with greater efficiency and purity.

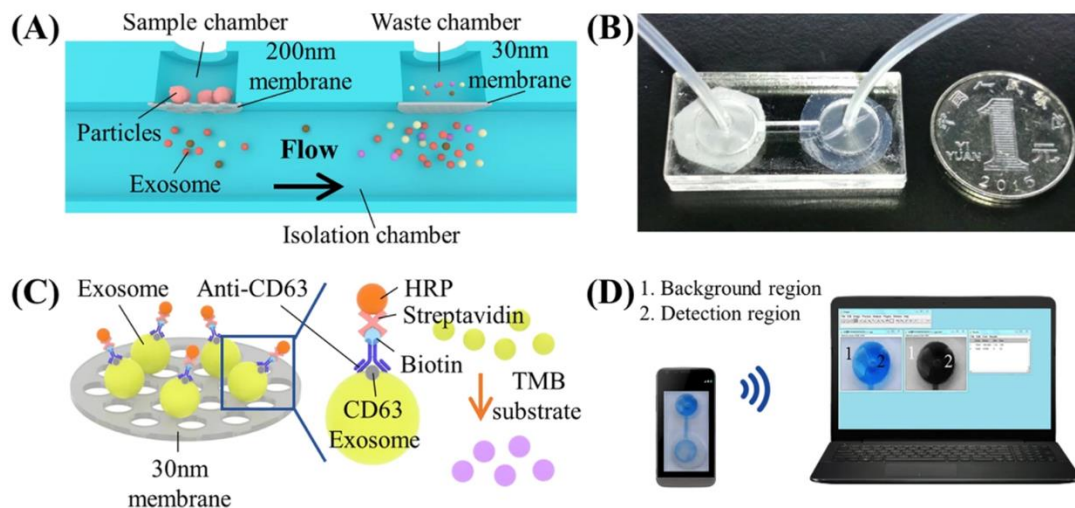


**Figure 2-2:** (A) Schematic of a double-filtration microfluidic device for isolation and detection of EVs. Based on size-exclusion, particles larger than 200 nm are excluded by the membrane with a pore size of 200 nm in the sample chamber, whereas particles smaller than 30 nm pass through the double-filtration device. EVs with a size between 30 and 200 nm are isolated and enriched in the isolation chamber. (B) Image of an assembled double-filtration device. (C) Schematic of direct ELISA for EV detection on-chip. The EVs isolated in the double-filtration device is labeled with biotinylated anti-CD63 antibodies, and then with streptavidin-HRP. The addition of TMB substrate enables blue color development in the double-filtration device. (D) The ELISA result is imaged using a smartphone and then transferred to a laptop for data analysis using ImageJ. Reproduced with permission from Liang et al., 2017 under Creative Commons Attribution License (CC BY 4.0), Copyright 2017, Springer Nature.

#### 2.4.2.2 Immunoaffinity-based separation

Efficient isolation of exosomes in microfluidic devices using an immunoaffinity-based approach requires the selection of antibodies. It is the most common microfluidics-based exosome isolation method. One of the earlier works represented an easy and fast immunoaffinity-based isolation of exosomes using anti-CD63 antibody from serum using a microfluidic device with herringbone grooves<sup>171</sup>. Later, Kanwar et al. used the same

antibody functionalized microfluidic chip for isolation of exosomes from serum sample and proposed the name of the kit as “ExoChip”. ExoChip was fabricated from PDMS and the surfaces were modified with anti CD63 antibody for successful isolation of exosomes<sup>89</sup>. To perform ultrasensitive isolation and analysis of exosomes, a 3D nanostructure (comprised of graphene oxide and polydopamine) coated microfluidic device was used to capture exosomes from plasma samples using an anti-CD81 antibody (**Figure 2-3**)<sup>172</sup>. Results implemented that the addition of the nanointerface increased the exosome isolation efficiency with reasonable yield compared to the other existing methods. A more recent study performed by Zhang et al. presented a herringbone mixer-based microfluidic chip that can directly separate exosomes from plasma using an immunoaffinity-based approach. This method enabled successful capture of pancreatic cancer-specific, Glypican-1 expressing exosome subpopulation with good yield while avoiding non-specific bindings<sup>173</sup>. However, immunoaffinity-based capture requires careful selection of antibody, and the purity of the isolated exosomes needs improvement.

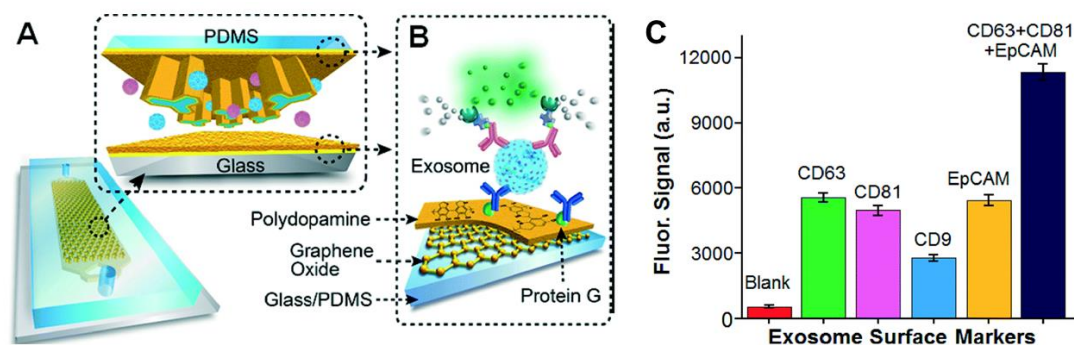


**Figure 2-3:** The nano-interfaced microfluidic exosome platform (nano-IMEX). (A) Schematic of a single-channel PDMS/glass device, with the exploded-view highlighting the coated PDMS chip containing an array of Y-shaped micro-posts. (B) The surface of the channel and micro-posts coated with graphene oxide (GO) and polydopamine (PDA) as a nanostructured interface for the sandwich ELISA of exosomes with enzymatic fluorescence signal amplification. (C) Surface protein profiling of COLO-1 cell exosomes ( $10^6 \mu\text{L}^{-1}$ ) captured by CD81 mAb. Reproduced with permission from Zhang et al., 2016 under Creative Commons Attribution Non-Commercial 3.0 Unported License, Copyright 2016, Royal Society of Chemistry.

#### 2.4.2.3 Acoustic fluid-based isolation

Acoustofluidics is the combination of microfluidics and acoustics methods for the separation of various bioparticles depending upon their size differences, density, membrane composition, and acoustic properties. This isolation method offers both a reagent-free and contact-free approach. In this process, continuous acoustic streaming enables acoustic forces of various magnitudes based on the particle sizes that act on the same plane as the microsensor. The performance of acoustofluidic devices is based on the principle that particles in an acoustic field experience radiation forces that alienate them from the pressure antinodes, and as a result, pushing the particles toward the pressure nodes along with a counteracting Stokes drag force<sup>165</sup>. The drag force is proportional to the radius while the acoustic radiation force is proportional to the volume. Hence, larger particles (e.g., blood cells) get deflected from their paths more than smaller particles

(e.g., exosomes) subjected to acoustic waves. Acoustofluidics has been implemented successfully by different research groups to separate cells, particles, and nanoscale vesicles from biological fluids <sup>92,174</sup>. Wu et al. have developed a novel acoustofluidic platform for the successful isolation of exosomes directly from an undiluted human blood sample. The integrated device had two sequential surface acoustic wave-based microfluidic modules- one to remove cells, and the other for the isolation of exosomes **(Figure 2-4)**. Using this novel method, the authors achieved about 98% purity in the isolated exosomes from just 100  $\mu$ L of the blood sample with high yield in 25 minutes, which was faster than the conventional centrifugation approach <sup>92</sup>. In one of the more recent studies, Z. Wang et al. implemented acoustofluidics to successfully separate traumatic brain injury (TBI) related exosomes from blood plasma. The study indicated that TBI-induced exosome samples contained an increased amount of glial fibrillary acidic protein (GFAP). To evaluate that the isolated exosomes were indicative of TBI diagnosis, pre-TBI and post-TBI samples were labeled with fluorescent dyes and neuron intake studies were performed which concluded that the TBI-induced samples had higher intake rates compared to the healthy samples. More researchers are getting involved during recent years in using acoustic-fluid based exosome isolation techniques for cancer detection, liquid biopsy, and brain injury due to its capability of isolating highly pure exosomes in a very short time by using very low volume of samples <sup>176</sup>.

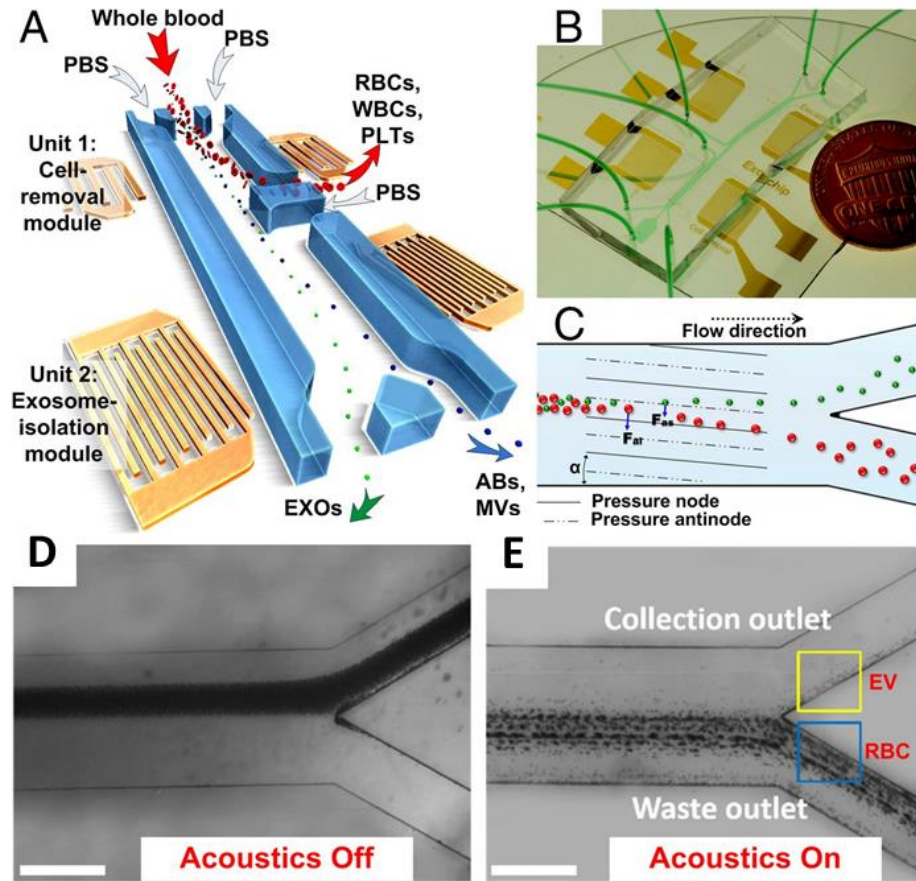


**Figure 2-4:** A) Schematic illustration of an acoustic-based separation microfluidic chip for separation of exosomes from whole blood. RBCs, WBCs, and PTLs are removed by the cell-removal module, and then, exosomes are separated by the exosome-isolation module. B) An optical image of the integrated acoustofluidic microfluidic chip. C) The periodic distribution of pressure nodes and the trajectory of particles with different diameters in each separation module. D, E) Isolation of EVs from whole blood using the cell-removal module. The images at outlet region when acoustic waves are (D) off and (E) on. Blood cells are pushed to bottom outlets when the acoustic field is on. The white stripe in the figure indicates the centerline location of the CCD image sensor (Scale bar: 500  $\mu\text{m}$ ). Reproduced with permission from Wu et al., 2017. Copyright 2017, National Academy of Sciences.

#### 2.4.2.4 Deterministic lateral displacement (DLD)

The deterministic lateral displacement (DLD) method acts upon the principle that the flow path of the particles larger or smaller than the critical size is altered while providing a natural flow path for the rest of the particles<sup>177</sup>. This continuous-flow

separation technique allows the particles larger than the critical size to displace laterally while the smaller particles flow through the fluid streamline. For the DLD approach, a gradient of nano-pillar arrays having specific critical sizes for particle separation is arranged within the microfluidic channels with proper spacing between the pillars. DLD has been implemented for separating cells, particles, and bioparticles from various fluids and biofluids with very high resolution ( $\sim 10$  nm)<sup>178–180</sup>. An array of pillars with a 2  $\mu$ m gap between each one was fabricated and implemented for the separation of 51 nm diameter nanoparticles, which was found to be effective for the isolation of particles ranging from 51 nm to 1500 nm<sup>181</sup>.



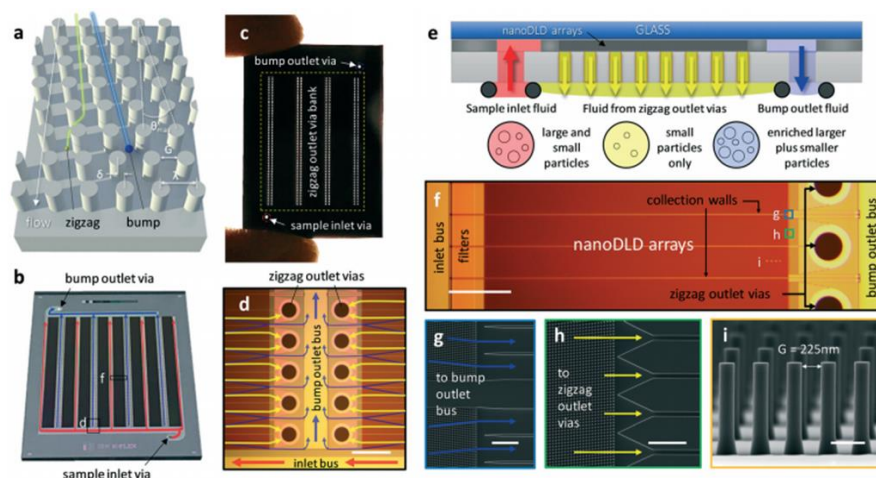


**Figure 2-5:** Operation and layout of integrated nanoDLD chips. (a) Schematic representation of a DLD pillar array defining the gap size  $G$ , pillar pitch  $\lambda$ , and row-to-row shift  $\delta$  parameters, which determine the geometric angle,  $\theta_{\max}$ , along which larger particles are deflected. Particle trajectories are illustrated for particles with diameters  $D_P$ , above (blue) and below (yellow) the critical diameter  $D_C$  which depends on the geometry of the array. (b) Tilt view optical image of the top side of a  $22\text{ mm} \times 30\text{ mm}$  nanoDLD chip, showing the sample inlet and bump outlet via positions with corresponding directional flow paths for injected sample (red) and outgoing bumped particle (blue) fluids along with a common bus network. (c) Backlit optical image of a nanoDLD chip (backside) revealing the through-hole via positions of the sample inlet (red), bump outlet (blue), and zigzag outlet via bank (yellow). (d) Optical microscope image highlighting the zoom-in section labeled in (b) with superimposed flow paths for the sample inlet (red), zigzag mode (yellow), and bump mode particle (blue) trajectories. NanoDLD arrays are paired to common zigzag outlet vias or drains, where smaller particles  $D_P < D_C$  exit to the backside of the chip into a common reservoir and larger particles  $D_P \geq D_C$  empty into a common bump outlet bus en route for the bump outlet via. Scale bar =  $400\text{ }\mu\text{m}$ . (e) Cross-sectional chip schematic illustrating the process of sample injection with zigzag and enriched, bump-particle fluid isolation and collection in common reservoirs on the backside of the chip from the different via sets. (f) Optical microscope image showing the labeled zoom-in section of (b) representing the layout of four parallel nanoDLD arrays relative to the surrounding inlet bus, filters, zigzag outlet vias, and bump outlet bus features. Scale bar =  $300\text{ }\mu\text{m}$ . (g and h) Scanning electron microscopy (SEM) image zoom-in locations of (f) along the array outlet interface indicating the direction of larger  $D_P \geq D_C$  particles bumping at  $\theta \approx \theta_{\max}$  toward the bump outlet bus (g) and smaller  $D_P < D_C$  particles toward the zigzag outlet via drains (h) as they exit the array. Scale bars =  $5\text{ }\mu\text{m}$ . (i) Tilt view cross-sectional SEM image of a  $G = 225\text{ nm}$  array ( $\lambda = 400\text{ nm}$ ) with a pillar height of  $1\text{ }\mu\text{m}$ , typical features of devices used in this study. Scale bar =  $400\text{ nm}$ . Reproduced with permission Smith et al., 2018. Copyright 2018, Royal Society of Chemistry.

A novel nano-DLD platform was reported by Wunsch et al. as an isolation platform for colloids and exosomes ranging from 20 nm to 110 nm by fabricating an array of pillars consisted of gap sizes between 25 nm and 235 nm. A drawback of this platform was the very low fluidic volume rate ( $\sim 0.2 \mu\text{L h}^{-1}$ ) that was caused due to the integration of high hydrodynamically-resistive attributes<sup>182</sup>. To overcome the issue, the same research group developed another microfluidic device consisting of 1000 parallel nano-DLD arrays (**Figure 2-5**) which resulted in an increase in the fluidic rate up to  $900 \mu\text{L h}^{-1}$  presenting the immense potential of the platform for exosome separation and analysis applications<sup>178</sup>. Additionally, the platform showed superior exosome recovery efficiency ( $\sim 50\%$ ) compared to the other previously reported DLD platforms. Although DLD is a very promising label-free and easily implementable exosome isolation method, concerns related to low separation purity due to clogging are yet to be addressed.

#### 2.4.2.5 Electroactive isolation technique

Electroactive isolation of different nanoparticles and exosomes is dependent on the principle of separating particles based on their cellular compositions, diameters, cytosolic conductivity, variation in dielectric constants, and membrane capacitance by applying a non-uniform electric field either by generating alternating current across the electrode arrays or by fabricating hurdles in the fluidic channel<sup>183,184</sup>. The electric field produces a continuous rotating flow pattern inside the microfluidic device that can result in the separation of particles by moving them either out of the plane or near the electrode<sup>185</sup>. Two kinds of electroactive methods have been implemented by the researchers, also known as electrokinetic filtration and dielectrophoresis, to isolate exosomes based on the factors mentioned above. An electrokinetic filtration-based microfluidic device was first

introduced by Davies et al. to drive the negatively charged exosomes from mouse blood samples across the membrane and move the other particles in the opposite direction. Later, Cho et al. implemented a microfluidic device with commercially available porous membranes to isolate exosomes from diluted plasma while the protein and other larger molecules were electrokinetically filtrated through the membrane. This device was able to remove  $\sim 84\%$  of the protein contents in less than 30 minutes with a 65% of recovery rate that provided approximately 8 times higher than the conventional ultracentrifugation technique<sup>93</sup>. However, electrokinetic filtration causes bubbles formation on the electrodes that can result in restricting the flow through the microfluidic channel. The other form of the electroactive isolation method, dielectrophoresis, is dependent on the dielectric constants of the particles. Insulator-based dielectrophoretic microfluidic device has been reported for label-free isolation of exosomes subpopulation by generating low DC voltage ( $10 \text{ V cm}^{-1}$ ) across the pipette's length<sup>186</sup>. This device showed great promise in capturing exosomes inhibiting closer to the pipette tip with an increase in the recovery rate over time. Ibsen et al. developed a lab-on-a-chip dielectrophoresis device to isolate glioblastoma exosomes from plasma samples in just 30 minutes by applying AC voltage of 18 Vpp and 15 kHz. The on-chip isolation was conducted by developing a dielectrophoretic high-field region combining the silicon dioxide layer and the fabricated electrodes, which attracted the exosomes and excluded the larger particles. To validate the captured exosomes on the microelectrodes, authors implemented SEM and *in situ* immunofluorescence along with the specific CD63 and TSG101 antibodies<sup>187</sup>. The same platform has also been implemented to isolate exosomes from both serum and plasma from Pancreatic Ductal Adenocarcinoma (PDAC) patients with  $\sim 99\%$  sensitivity and  $\sim$

82% specificity (**Figure 2-6**)<sup>188</sup>. Dielectrophoresis-based exosome isolation is a very promising high throughput method that can be implemented in clinical settings by improving the flow velocity inside the microfluidic channel to increase the separation efficiency of exosomes from various complex bodily fluids.

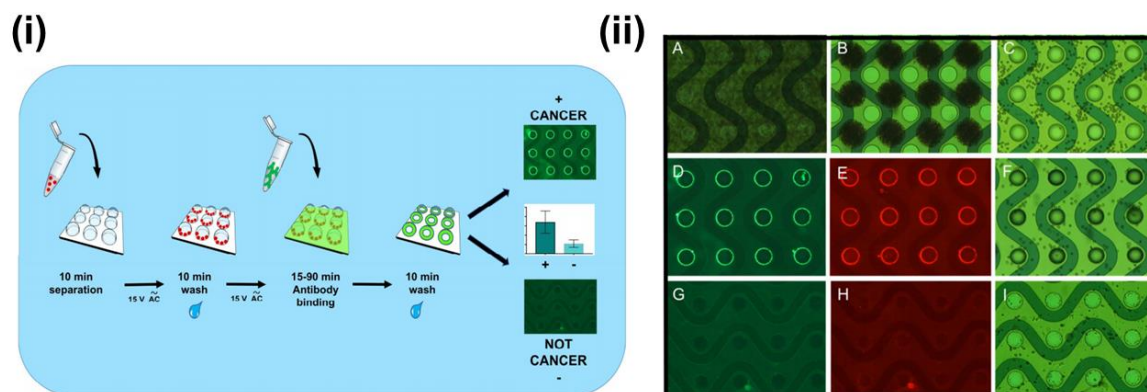


**Figure 2-6:** (i) Schematic diagram illustrates the ACE (AC electrokinetic) direct immunoassay procedure. Undiluted whole blood, plasma, or serum sample is added directly to the chip. A 10- minute application of AC current to the chip affects dielectrophoretic separation and isolation of target nanoscale extracellular vesicles (EVs) and other particulates onto the chip electrodes. Unbound material is washed off the chip with 0.5 X PBS during an additional 10 minutes of AC current. After the current is stopped, EVs and nucleic acid targets can be analyzed by different methods, including the addition of fluorescent reporter antibodies and nucleic acid dyes that are applied to the chip, then incubated for the appropriate times. Following the final wash step, the chip is ready for direct imaging and analysis of the fluorescent signal. (ii) Whole blood from a pancreatic cancer patient is glypican-1 and CD63 positive in ACE Immunoassay. Panels A-C: Whole blood drawn from a patient with PDAC was applied to an ACE chip (A); application of current caused larger whole blood cells and particulates to migrate to low-field regions between electrodes (B). A buffer wash removed most cells and particulates from the chip (C). Panels D-F: Antibodies against glypican-1 and CD63 were incubated together on the chip, followed by fluorophore-conjugated secondary antibodies for detection (D, CD63, green; E, glypican-1, red; F, brightfield image). Panels G-I: As negative controls, primary antibodies were omitted, and the fluorophore-conjugated secondary antibodies alone did not label the electrodes (G, green channel; H, red channel; I, bright field image). Reprinted (adapted) with permission from Lewis et al., 2018. Copyright 2018, American Chemical Society.

## 2.5 Microfluidics-based exosome detection/analysis techniques

### 2.5.1 Fluorescence

Fluorescence is the most commonly used detection method of exosomes in microfluidics-based isolation and analysis. There are numerous examples of fluorescence

analysis of exosomes combined with different isolation methods. Kanwar et al. reported integrated on-chip exosome isolation and analysis platform, ExoChip, which involved specific antibodies to isolate exosomes from various body fluids (**Figure 2-7**).

Subsequently, the captured exosomes were stained with fluorescent dye followed by the quantification using plate reader <sup>89</sup>.

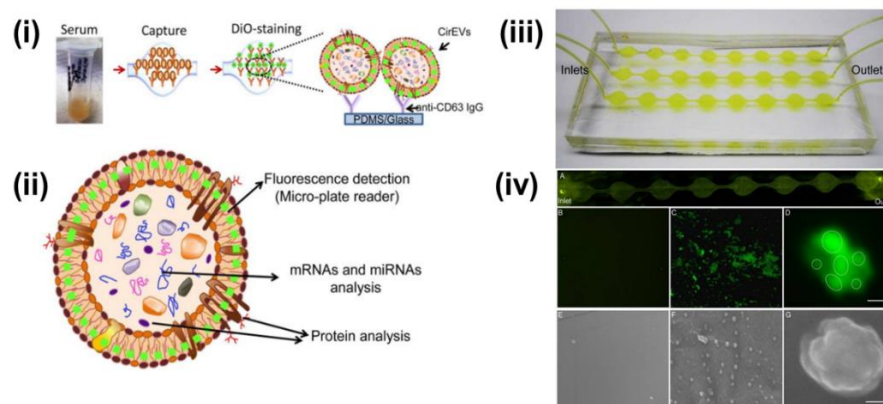


**Figure 2-7:** (i) Illustration depicting the scheme of exosomes capture and analysis procedure using ExoChip. The blood is collected for serum extraction from healthy or diseased individuals and then exosomes are captured by flowing serum through a CD63 antibody-coated ExoChip. To visualize the captured exosomes, ExoChip is processed for membrane-specific dye (DiO) staining. (ii) Experimental strategy for exosomes immobilization and characterization using ExoChip, The ExoChip is designed to measure the levels of fluorescently stained exosomes through fluorescence intensity measurements using microplate readers and allows molecular characterization of Exosomes contents through a variety of standard assays including protein analysis (western blots) and mRNA/miRNA analysis (RT-PCR/miRNA open array). (iii) A working prototype model of PDMS-based ExoChip (three channel) depicting the flow of serum for exosomes capture in a typical experimental setup. (iv) Characterization of Exosomes captured using ExoChip, A: Fluorescence microscopy image of ExoChip channel depicting immobilization of exosomes in native forms after DiO staining. High magnification (400X) images of control one of the control chambers (B) and anti-CD63 coated chambers depicting exosomes capture (C). Per the light-microscopy resolution limits the exosomes as visualized were found to be in clusters which were also confirmed through confocal microscopy. D: A confocal microscopic image showing a group of smaller exosomes (depicted as dotted circles) forming a cluster (bar = 2μm). The native morphology of the exosome vesicles was revealed following EM analysis. Electron micrograph images showed the absence of any vesicle immobilizations in control ExoChip (E), whereas the anti-CD63 coated ExoChip (F) showed the presence of exosomes both in clusters as well as single vesicles (bar = 500nm). G: A magnified view of a single exosome vesicle as examined under EM depicting a cluster of exosomes (bar = 100nm). Reprinted (adapted) with permission from Kanwar et al., 2014. Copyright 2014, Royal Society of Chemistry.

Recently, a homogeneous magneto-fluorescent exosome (hMFEX) nanosensor has been developed for rapid and on-site tumor-derived exosomes analysis<sup>189</sup>. This

integrated approach was able to detect the tumor-derived exosomes with high specificity having the limit of detection of  $6.56 \times 10^4$  particles  $\mu\text{L}^{-1}$  which demonstrates the excellent potential of high clinical diagnostic efficacy of the hMFEX nanosensor<sup>189</sup>. Another more recent study reported a fluorescence analysis method to quantify and differentiate between the normal and metastatic Sentinel lymph node (SLN) derived exosomes captured using silicon nanoparticles-based exosome probes (SiNPs@EXO)<sup>190</sup>. Fluorescence analysis depicted that fluorescence signal in metastatic SLNs reached a peak within 30 minutes and stayed up to 3 hours, whereas, normal SLNs attained the peak in about an hour followed by a sudden decrease in the signal<sup>190</sup>. This integrated tool showed amazing potential for predicting lymphatic metastasis of tumors by targeting SLNs.

### 2.5.2 Colorimetric

Colorimetric detection is based on the principle of identifying a sample by comparing the color depth of a chromogenic material. Colorimetric detection has been integrated with microfluidics by many researchers to visualize the capture and analysis of exosomes. Vaidyanathan et al. reported a microfluidic platform with functionalized electrodes specific for capturing exosomes. The electrode surface was responsible for generating nanoscale fluid flow, and the absorbance measurement of the colorimetric solution was used to detect and quantify exosomes with high specificity. This platform showed superior sensitivity compared to other fluid dynamics-based approaches<sup>191</sup>. Another sensitive and selective colorimetric aptasensor was successfully implemented for the detection of cancer-derived exosomes facilitated by the polymerization of horseradish peroxidase (HRP)-accelerated dopamine (DA) and *in situ* deposition of polydopamine



(PDA) <sup>192</sup>. For this study, the target exosomes were firstly isolated by latex beads, followed by bio-recognition using a specific CD63 aptamer, which was conjugated to horseradish peroxidase (HRP) through biotin-streptavidin binding <sup>192</sup> (**Figure 2-8**). Colorimetric detection was completed in 10 minutes via enzymatic catalysis which produced dark colored polydopamine (PDA) as a result of the enzymatic reaction between DA and monoamine oxidase that was quantified using absorbance measurement. The color depth correlated to the CD63 amount and the limit of detection (LOD) was found as  $7.7 \times 10^3$  particle mL<sup>-1</sup>, increasing the LOD by 3-5 orders of magnitude from conventional Dot-blot methods <sup>192</sup>.

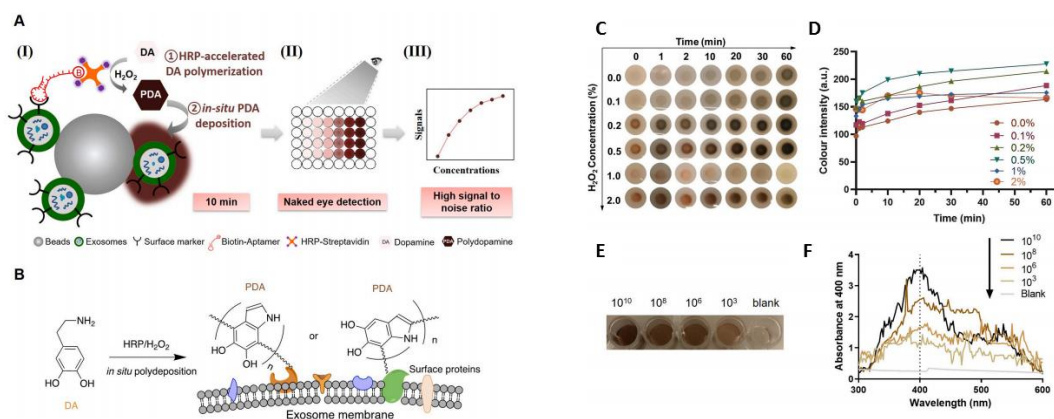


**Figure 2-8:** Schematic illustration of the proposed aptasensor with HRP accelerated dopamine polymerization and deposition for exosome detection (ExoAptaSensor). (A) (I) Exosomes anchored on sulfate/latex beads were captured by biotin-conjugated aptamer specific to CD63, followed by incubation with streptavidin-conjugated HRP for colorimetric reaction to convert colorless Dopamine (DA) into brown-black colored Polydopamine (PDA) in 10 min in Tris buffer (pH 8.5). This oxidation and polymerization process is accelerated under HRP catalysis and hydrogen peroxide (H<sub>2</sub>O<sub>2</sub>) as the oxidant. (II) Color developed by this aptasensor correlates to exosome concentrations and allows simple naked eye visualization. (III) Absorbance signals of the product can also be quantified at 400 nm. (B) Scheme shows the poly-deposition process of PDA onto surface proteins of exosomes in situ. (C), (D), (E), (F) illustrates Proof-of-concept study of ExoAptaSensor. (C) Color intensity of PDA deposition at the target site of HRP where the concentration of H<sub>2</sub>O<sub>2</sub> varied from 0% to 2%. (D) Color intensity measured at intervals of 0, 1, 2, 10-, 20-, 30- and 60-min using ImageJ. (E) Digital images were taken right after color development of exosome samples in solution using the CD63 ExoAptaSensor. Color intensity was dependent on exosome concentrations (10<sup>10</sup>, 10<sup>8</sup>, 10<sup>6</sup>, 10<sup>3</sup>, and 0 (blank) particles, respectively). (F) Absorbance spectra were obtained at wavelengths from 300 nm to 600 nm, with a peak at 400 nm correlates with the changes in exosome concentrations. This supports the ability of the developed colorimetric aptasensor for exosome detection. Reprinted from *Development of a simple, sensitive, and selective colorimetric aptasensor for the detection of cancer-derived exosomes*, Volume 169, Xu et al., 2020a, Page No. 112576, Copyright 2020, with permission from Elsevier.

Another research group proposed a highly sensitive plasmonic colorimetric biosensor for exosome quantification. The two-step sensing technique involved exosome-induced competitive reaction and etching of gold nanobipyramid@MnO<sub>2</sub> nanosheet

nanostructures (Au NBP@MnO<sub>2</sub> NSs)<sup>193</sup>. A competitive reaction induced by exosomes translated the signal of exosomes into the amount of alkaline phosphatase, which simplified the experimental process and amplified the signal. On the other hand, the etching of Au NBP@MnO<sub>2</sub> NSs by ascorbic acid altered the refractive index of Au NBPs, accompanied by the blue shift of the longitudinal localized surface plasmon resonance peak. Aided by the signal amplification of the competitive reaction and outstanding refractive index sensitivity of the colorimetric substrates, this process demonstrated high sensitivity within  $8.5 \times 10^2$  to  $8.5 \times 10^4$  particles  $\mu\text{L}^{-1}$  of exosomes along with a detection limit of  $1.35 \times 10^2$  particles  $\mu\text{L}^{-1}$ , providing proof of superior sensitivity of exosomes detection than previously reported colorimetric methods<sup>193</sup>.

### 2.5.3 Magnetic based methods

Traditional nuclear magnetic resonance (NMR) is widely used to perform chemical analysis but cannot be readily implemented for the detection of exosomes due to their very small sizes. Because of their ultrasmall sizes, exosomes demonstrate a very low signal-to-noise ratio (SNR) in micro-nuclear magnetic resonance ( $\mu\text{NMR}$ ), which was first reported by Issadore et al. as a modified version of NMR exclusively for capturing small particles such as exosomes<sup>194</sup>. To improve the process, Shao et al. developed a microfluidics-based  $\mu\text{NMR}$  device that could simultaneously quantify the exosomes and the protein contents inside them. The exosomes were isolated using immunomagnetic nanoparticles (IMNPs) followed by filtrating the IMNP-labeled exosomes<sup>195</sup>. The presence of INMPs converts the complexes found in the IMNP-captured exosomes into super magnetic, therefore, increased the SNR of the process. This reported platform showed very good detection sensitivity coupled with high

reproducibility <sup>195</sup>. Recently, Sancho-Albero et al. reported a continuous-flow microfluidic device for the isolation and analysis of exosomes from the whole blood sample, fetal bovine serum (FBS), and PBS of pancreatic cancer (PC) patients integrating CD9-mediated magnetic capture (**Figure 2-9**). The identity of the tetraspanins was verified by the coexpression of a second exosomal protein CD63 quantified by a CD63 ELISA test. Finally, exosomes from the whole blood of PC patients were captured and the exosomal CA19-9 protein levels were evaluated. The results show the potential of exosome separation and analysis as a marker of PC progression <sup>196</sup>. However, the main challenge for the  $\mu$ NMR detection method remains the complexity of this technique for point-of-care diagnosis.

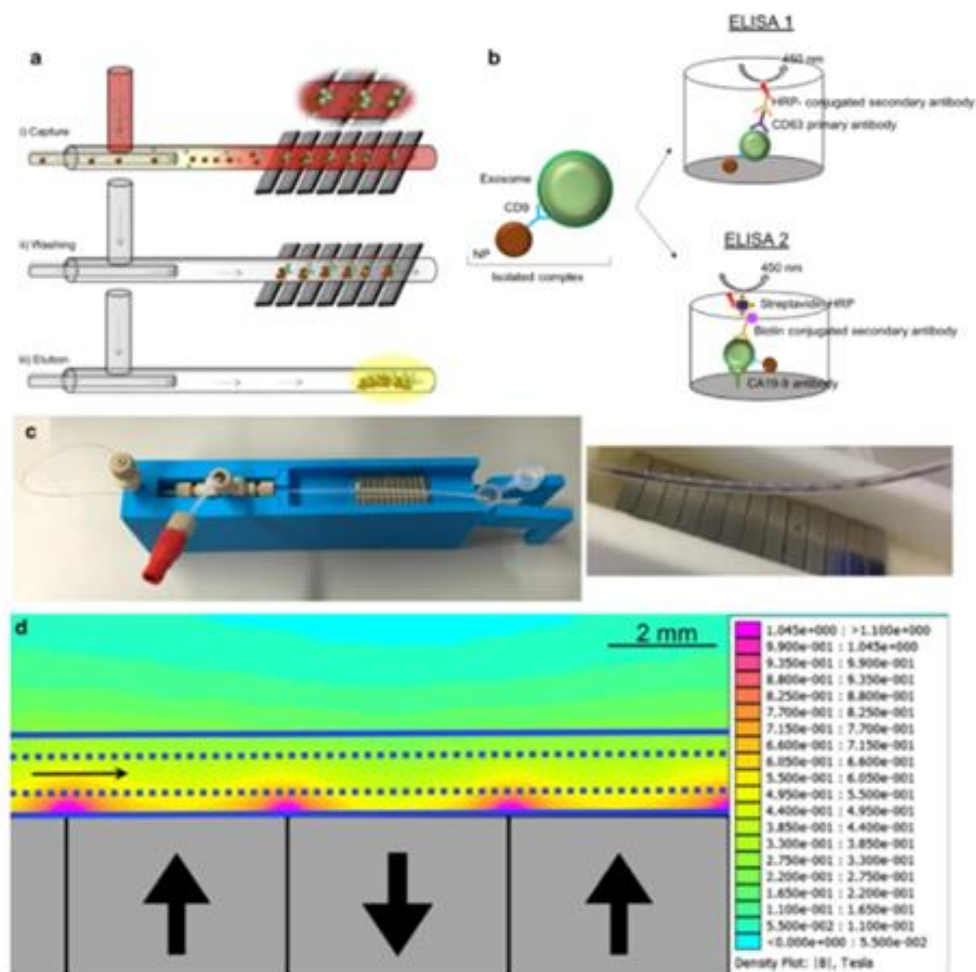


**Figure 2-9:** (a) Operation principle of the coaxial mixer. (b) ELISA analysis against CD63 and CA19-9 was performed after exosome capture from whole blood. (c) Left: Image of setup. Right: The pipe is lifted from the magnets showing the NPs captured at the junctions between the alternate polarization magnets. d Simulation of the magnetic gradient created between each pair of NdFeB magnets. Nanoparticle accumulation coincides with the high-intensity nodes. The tubing is represented with solid and dashed blue lines. Reproduced with permission from Sancho-Albero et al., 2020 under Creative Commons Attribution License (CC BY 4.0), Copyright 2020, Springer Nature.

#### 2.5.4 Surface plasmon resonance (SPR)

Surface plasmon resonance (SPR) is defined as a type of resonant oscillation of the electrons caused by the electric field components of the incident light at the interface between a negative and a positive dielectric constant material. This oscillation is prone to any sensitive change in the boundary conditions which is often employed by the

researchers to detect various biomolecules<sup>197,198</sup>. Microfluidics-based SPR is an emerging method of exosome isolation due to its cost-effectiveness, portability, and the ability of very fast label-free detection. One of the pioneering works regarding this method presented an on-chip SPR sensor that was able to isolate and quantify various exosomal proteins. The authors modified the gold surface with the antibodies and used antibody microarrays to capture exosomes which led to a change in the refractive index<sup>199</sup> (**Figure 2-10**). Using this method, they were able to quantify and analyze various exosomal proteins simultaneously.

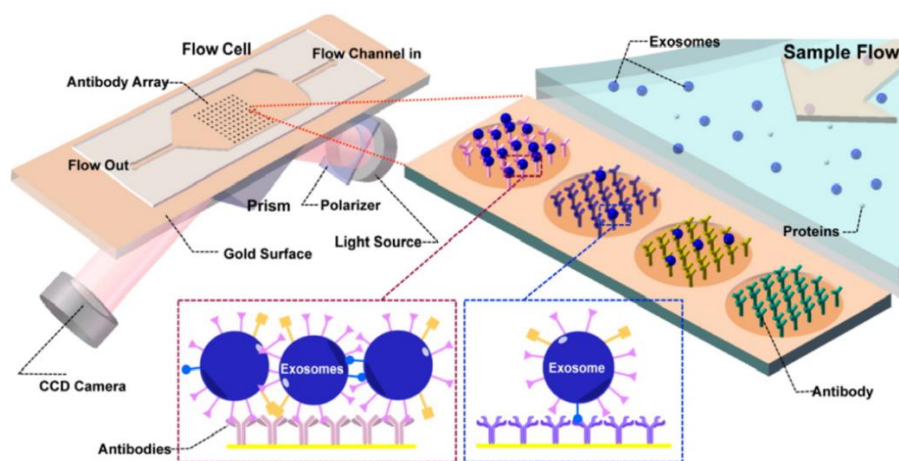


**Figure 2-10:** Schematic view of SPRi in combination with antibody microarray to capture and detect exosomes in the cell culture supernatant. Antibodies specific to exosome transmembrane proteins were printed on the gilded gold chip. The optical path from the laser passes through the coupling prism at a fixed angle of incidence, and the reflection is recorded by a CCD camera. Upon injection of sample into the flow cell, exosomes can be captured by antibodies on the chip, resulting in changes in the refractive index and therefore changes in the reflection intensities, which are monitored by the CCD camera. Reproduced with permission from Zhu et al., 2014 (article link: <https://pubs.acs.org/doi/10.1021/ac5023056>), Copyright 2014, American Chemical Society. Any future use of this content is subjected to permission from ACS Publications.

Recently, W. Chen et al. reported a novel label-free real-time surface plasmon resonance imaging (SPRi) biosensor based on the hydrogel-AuNp supramolecular sphere (H-Au) for very sensitive and specific detection and quantification of prostate cancer cell-derived exosomes. Before the detection, the localized surface plasmon resonance (LSPR) effect of AuNPs and the signal amplification effect of the mass cumulative hydrogel were integrated with highly specific aptamer<sup>200</sup>. This developed sensor showed an extraordinary wide linear range of detection between  $1.00 \times 10^5$  and  $1.00 \times 10^7$  particles  $\text{mL}^{-1}$  and has a limit of detection of  $1.00 \times 10^5$  particles  $\text{mL}^{-1}$ <sup>200</sup>. Additionally, the SPRi signal maintained a very strong correlation with the t-PSA value measured by the clinically implemented chemiluminescence immunosensors. Therefore, this microfluidics-based SPR biosensor revealed exceptional feasibility for human serum analysis and would carry a great potential in biomolecular analysis and point-of-care diagnosis.

#### 2.5.5 Electrochemical

Electrochemical process is a highly apposite detection method for biomolecular analysis including exosomes due to very simple protocol, ease of integration with the microfluidics platforms, and high sensitivity<sup>201</sup>. In electrochemical detection, the antibody or aptamer element attaches specifically with exosomes, therefore, generating an electrochemical signal altered by the exosomes which are used to quantify and analyze the exosomes<sup>202,203</sup>. Electrochemical detection has been used for the successful detection of various biomarkers and biomolecules, including exosomes<sup>204,205</sup>. One of the pioneering works by Zhou et al. reported an aptamer-based electrochemical biosensor for quantitative detection and analysis of exosomes by immobilizing the aptamers specific to

exosome tetraspanin protein, CD63, onto gold electrodes and integrating this into a microfluidic platform. The concentration of exosome was quantified by measuring the signal generated when combining the methylene blue (MB)- labeled probe strand and the exosome-specific aptamer. Signal output decreased in presence of exosomes as they tend to displace the probe strands <sup>202</sup>. This reported biosensor was able to detect  $1 \times 10^6$  particles  $\text{mL}^{-1}$  of exosomes, which replicated an approximately 100-fold improvement in the limit of detection (LOD) in comparison with the commercial immunosensors based on anti-CD63 antibodies <sup>202</sup>. Recently, another research group has reported a detachable microfluidic device integrated with an electrochemical aptasensor (DeMEA) for highly sensitive and in-situ quantitative detection of cancerous exosomes <sup>206</sup> (**Figure 2-11**). The authors immobilized an aptamer specific to the epithelial cell adhesion molecules onto the gold-plated electrode for very specific detection of the cancerous exosomes. Additionally, a microfluidic vortexer was integrated using 3D printed magnetic housing to escalate the collisions between the exosomes and sensing surface using hydrodynamically generated transverse flow <sup>206</sup>. The reported platform exhibited high sensitivity and high specificity with an opportunity to consequently culture exosomes for downstream analysis by utilizing the detachable nature of the device. Moreover, the DeMEA displayed an ultra-low limit of detection of 17 exosomes  $\mu\text{L}^{-1}$  over a wide dynamic range ( $1 \times 10^2$  to  $1 \times 10^9$ ) exosomes  $\mu\text{L}^{-1}$  in less than 50 minutes <sup>206</sup>.



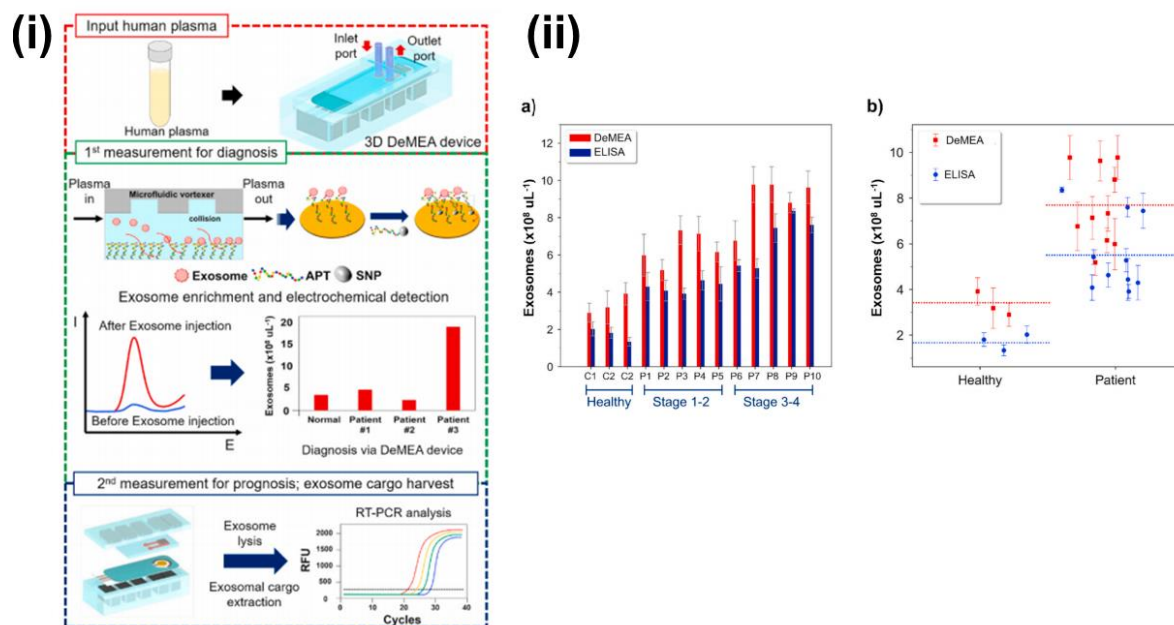


**Figure 2-11:** (i) Schematics of complete detachable microfluidic analysis system with electrochemical aptasensor (DeMEA) for sequential analysis of cancerous exosomes. (ii) Clinical plasma samples analysis to quantify the exosomes derived from MCF-7 cancer cells using the developed DeMEA and ELISA. The results obtained from the DeMEA and ELISA are represented in (a) bar graph, (b) scatter graph. All measurements were carried out in triplicate, and error bars correspond to standard deviations from independent measurements ( $n = 3$ ). Reprinted from *Detachable microfluidic device implemented with electrochemical aptasensor (DeMEA) for sequential analysis of cancerous exosomes*, Volume 169, Kashefi-Kheyraadi et al., 2020, Page No. 112622, Copyright 2020, with permission from Elsevier.

## 2.6 Conclusions and discussions

This chapter summarizes the biological functions of exosomes and their roles as various disease biomarkers as well as in point-of-care diagnostics. Additionally, the conventional isolation and detection methods have also been discussed with their respective advantages and disadvantages. In the latter half of the chapter, microfluidics-based exosome isolation and detection methods, their basic principles, the reasons behind the emergence of microfluidics-based exosome capture and analysis, their respective advantages and disadvantages, and the latest advancements in microfluidics-based

exosome isolation and detection have been discussed in detail. Although microfluidics provides a rapid and more accurate quantification and analysis of exosomes from various biofluids compared to the conventional techniques, the biggest challenge is to perform high-throughput exosome separation with high purity, minimal damage, and high yield. Due to the heterogeneous nature of the exosomes, it is often very difficult to obtain highly pure exosomes that result in lowering the accuracy. With the ongoing efforts from the researchers for integration of exosomes isolation and detection methods with the microfluidics platform, it is expected that the next major step in this field will be the emergence of point-of-care devices for applications in clinical settings.

## CHAPTER 3

# DEVELOPMENT OF ANTIBODY FUNCTIONALIZED PROBE FOR SELECTIVE PURIFICATION OF EXOSOMES<sup>†</sup>

### 3.1 Background

As discussed previously in chapter 2, The clinical applications of exosomes have not been fully realized due to technical challenges associated with traditional and newer methods for exosome isolation. Inefficient purification techniques lead to the extraction of heterogeneous extracellular vesicles that have different sizes, surface proteins, or cellular origins. Selective isolation of surface-protein marker-specific exosomal subpopulations for subsequent genetic analysis is critical in studies to evaluate their clinical relevance <sup>101</sup>. For example, CD63-positive exosomes are present at a higher level in malignant cells compared to healthy ones <sup>141</sup>, while exosomes secreted in cerebrospinal fluid carry specific markers such as Alix, syntenin-1, heat shock proteins, and tetraspanins <sup>68</sup> that may provide crucial information for neurodegenerative disorders. Exosomal membranes are enriched in tetraspanins (CD63, CD9, and CD81) that are used as biomarkers for disease diagnostics and prediction of therapeutic response

---

<sup>†</sup> This chapter or portions thereof has been published in **Talanta** under the title “**ExoPRIME: Solid-phase immunoisolation and OMICS analysis of surface-marker-specific exosomal subpopulations**”. Volume 236 (2022). DOI: [10.1016/j.talanta.2021.122870](https://doi.org/10.1016/j.talanta.2021.122870). The current version has been formatted for this dissertation.

The challenge to develop a purification technique that can selectively isolate exosomes rapidly, reproducibly, efficiently, for clinical and research applications has been recognized in the scientific community. Multiple technologies that improve exosomal isolation have been developed by exploiting the biochemical properties of exosomes, and the process has rapidly evolved in recent years<sup>47,182</sup>. While these conventional techniques have advantages and disadvantages, they all purify a population of exosomes that express different surface markers. A rapid, and antigen-selective technology that provides high-purity exosomal subpopulation will accelerate extracellular vesicles research and the development of exosome-based products and applications. The Dynabeads® magnetic separation technology is highly specific and has a highly concentrated yield and purity at the time of capture, in addition to ensuring the integrity of isolated exosomes<sup>136</sup>. However, the pH and ionic concentrations of the reagents required to elute the exosomes from the stationary phases for downstream analysis can easily alter the properties of most of the exosome products, rendering them inadequate as best-practice models for exosome utilization. The greatest limitation to widespread adoption of the immunoaffinity-based method is its high reagents cost that limits the sample volume being analyzed. To overcome the identified technical challenges, traditional exosome purification technologies are sometimes used in combination in an attempt to provide a simple, fast, efficient, and affordable technique for the solid phase isolation of exosomes. A novel ultrafast-isolation system called EXODUS employs a nanoporous membrane to rapidly isolate and concentrate exosomes from biofluids via acoustofluidic streaming<sup>176</sup>. Despite advantages over existing methods, the negative oscillatory pressure applied to the sample could lead to reduced integrity of the exosomes

in the sample. To date, no one has successfully developed a microprobe-based method for direct and high-throughput purification of intact exosomes.

In this study, we developed a method for immobilization of CD63 antibody-conjugated to streptavidin for the purification of surface marker-specific exosomes (**Figure 1-2**). The ExoPRIME tool provides a **P**recise **R**apid **I**nexpensive **M**ild (non-invasive) and **E**fficient (i.e., **PRIME**) alternative for exosome isolation and analysis. The current prototype: (1) is a portable and affordable platform that does not require large, expensive equipment, (2) operates *in situ* and eliminates the time-consuming, multistep protocol for additional pre-concentration steps of the biological specimen, (3) enables selective isolation of exosomes with a high-spatial-resolution, (4) provides flexibility in parameters selection to scale yield and speed, (5) permits reusability of the specimen multiple times, and (6) could allow integration with microfluidics-based standard systems for genomic and proteomic analysis of exosomal cargoes. Thus, this direct, single-step ExoPRIME Microprobe Technology holds promise for real-time exosome sample collection which can be applied for exosome enrichment and analysis of clinical specimens.

## 3.2 Materials and methods

### 3.2.1 Design and fabrication of the ExoPRIME microprobe

The novel ExoPRIME microprobe technology provides direct, *in situ* enrichment of intact exosomes based on immunoaffinity, without compromising their structure by avoiding the shear strain during centrifugation. We employed a multidisciplinary approach that includes thin-film immobilization, nanoscience, and immunobiology, to design, fabricate, and characterize a “smart microprobe” for purification of the antigen-

specific exosome. The ExoPRIME tool consists of an inert Serin™ stainless steel microneedle ( $300\ \mu\text{m} \times 30\ \text{mm}$ ) functionalized with an antibody (anti-CD63) that selectively binds to the corresponding tetraspanin embedded in the lipid bilayer of the exosomes. After incubation in a biofluid, the exosome capture efficiency is assessed via a fluorescent assay. Layer-by-layer (LbL) assembly was applied to create the precursor layer of six alternating polyethyleneimine/polyacrylic acid bilayers [PEI/PAA]<sup>6</sup> for the immobilization of biotin to the stainless-steel surface of the probe. 1-Ethyl-3-(3-dimethylaminopropyl) carbodiimide (EDC) mediated chemical linkage of amine-modified biotin to the carboxyl group of the PAA and was followed by the biotin-streptavidin covalent linkage of the CD63 antibody (**Figure 3-1**).

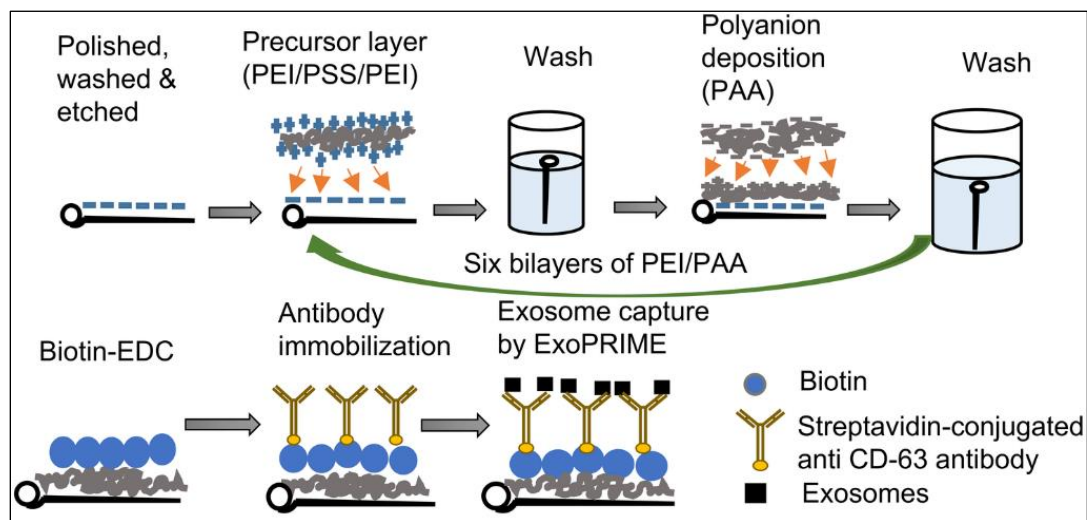


**Figure 3-1:** ExoPRIME probe functionalization workflow.<sup>54</sup>

### 3.2.2 Characterization of the microprobes to validate LbL precursor

Hitachi S-4800 field-emission scanning electron microscope (FESEM) that is located at the IFM facilities in Louisiana Tech University was used to characterize the layer-by-layer assembly functionalization of the polyelectrolytes on the microprobe surfaces. At first, the sample was attached to a 5mm sample plate. Then the sample was

loaded inside the specimen exchange chamber of the instrument and carefully placed in the holder receiver. Once the specimen was placed, the gate valve between the main chamber and the specimen exchange chamber was closed, and the sample was ready to image. For the imaging of the microprobes, secondary electron (SE) image signal, normal probe current, and ultra-high resolution (UHR) focusing mode was selected. For normal imaging, the vendor instructed beam acceleration voltage is 1-5 kV, which was maintained to image the microprobe samples. 3 kV and 5 kV beam acceleration voltages were used to image the needles. Beam alignment was performed in both low and high magnification modes (400X, and 2000X respectively) to obtain the best possible images. A control experiment was performed with a plain microprobe using the same specifications. To further investigate the functionalization process, EDX was used along with FESEM on both plain and functionalized microprobes. EDX analysis confirms traces of the elements of the polyelectrolytes for the functionalized needles which are not found in the plain needles

### 3.2.3 Confirmation of anti-CD63 antibody immobilization

Nikon Eclipse TE2000-U inverted microscope was used to evaluate the binding reaction between biotin with captured streptavidin. Polyelectrolyte functionalized microprobes were immersed and incubated for 1 hour at 37°C inside the stock biotin solution followed by rinsing in 10mM MES buffer and air drying. After that  $2 \mu\text{g mL}^{-1}$  anti-CD63 antibody solution, which was conjugated to streptavidin, was prepared from 1mg/mL stock anti-CD63 antibody (with streptavidin) in PBS buffer with 1:1000 dilution. Later, the needles were dipped into the solution for 2 hours, rinsed with PBS buffer, and air-dried. To evaluate the binding reaction between biotin with captured

streptavidin, needles with immobilized streptavidin were immersed in 0.4 M ( $258 \mu\text{g } \mu\text{L}^{-1}$ ) fluorescence-labeled biotin (biotin-FITC). The needles were incubated (after covering with aluminum foil to avoid photobleaching) into the solution at room temperature for 30 minutes, washed with PBS buffer, and air-dried. Later, the microprobes were studied under a fluorescence microscope using excitation/emission 490nm/516nm and exposure time 100 msec. Two control experiments were performed by omitting the streptavidin and the LbL precursor layers respectively.

### 3.3 Results and discussions

#### 3.3.1 Structural characterization of the LBL deposition on microprobe surfaces

The efficiency of the thin film deposition was assessed via scanning electron microscopy (SEM) coupled with energy-dispersive x-ray spectroscopy (EDX). Images obtained with a Hitachi S-4800 field-emission scanning electron microscope (FESEM) are shown in **Figure 3-2** and confirms that the film adsorption protocol provides efficient and stable deposition of polyelectrolyte precursor layers, for subsequent immobilization of biotin and streptavidin-conjugated anti-CD63 antibody. A control experiment was performed using a plain microneedle using the same imaging settings. The SEM images of the LbL-coated microneedle (**Figure 3-2B, E**), compared to the control samples (**Figure 3-2A, D**), show a denser material that appears as froth-like coverages on the faces and borders, while the conical outline of the microneedle is still maintained in both instances. The slight roughness observed on the control samples is a result of the sandpaper polishing and chemical etching, but devoid of polyelectrolyte bilayers. Both EDX spectra (**Figure 3-2C**) confirm the presence of the metallic constituents of stainless steel; iron, chromium, carbon, and other alloying elements such as nickel, manganese,



and silicon<sup>207</sup>. Additionally, in the LbL-coated sample (**Figure 3-2F**), we see traces of hydrocarbons (much higher carbon, oxygen) and nitrogen – consistent with the chemical composition of the polyelectrolytes used for the coating, supporting the SEM results. These experiments were performed with multiple arrays of microneedles, and they all showed the feasibility and reproducibility of the LBL assembly process.

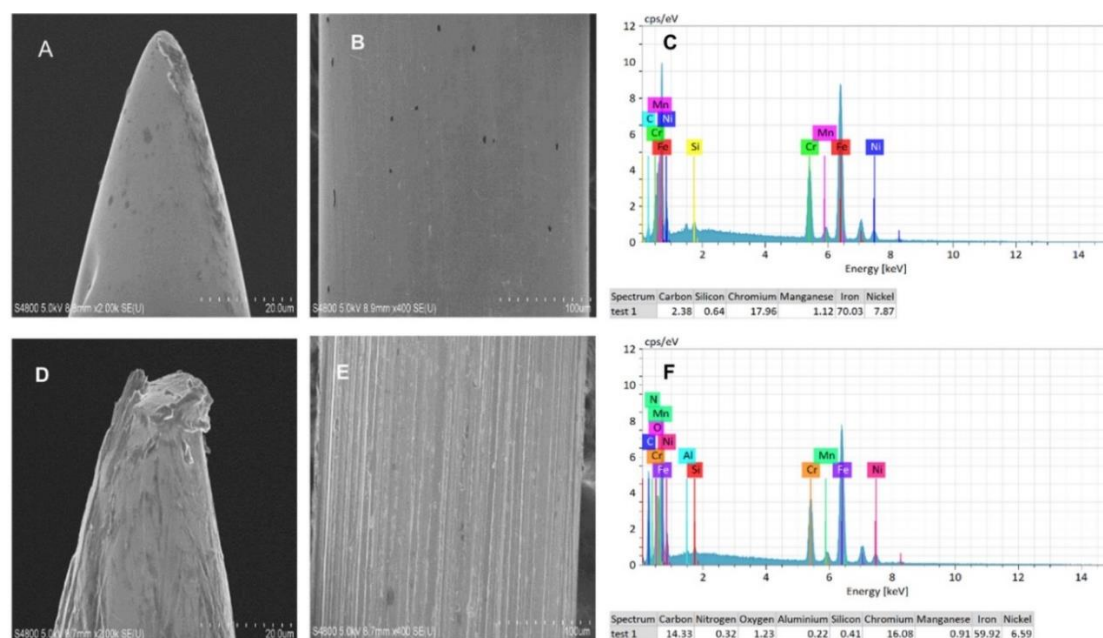


**Figure 3-2:** SEM micrographs of the tips (left panels) and stem (middle panels) of polished plain needles (A, B) and LbL-coated microneedles (D, E), showing successful and efficient deposition polyelectrolyte bilayers. The right panels show the corresponding EDX spectra of plain (C) and LbL-coated (F) microneedles.<sup>54</sup>

### 3.3.2 Validation of the antibody immobilization using fluorescence analysis

Efficient and selective capture of CD63+ (or other antigen-presenting) subpopulation of exosomes is an essential parameter for the accurate identification of exosomal biomarkers. The anti-CD63 antibody selectively binds to the surface protein marker expressed by exosomes. CD63 was selected for this study because its overexpression has clinical implications in tumorigenesis and metastasis. The efficiency

of biotin immobilization was assessed using fluorescein (FITC)-labeled biotin (**Figure 3-3**). Streptavidin-functionalized needles were incubated in biotin-conjugated FITC solution (**Figure 3-3A, D**) and imaged under a Nikon Eclipse TE2000-U inverted fluorescence microscope, 20x objective. Two different negative control experiments were performed to evaluate the non-specific binding of biotin to the stainless-steel surface of the needle (B) and the polyelectrolyte precursor layer (C). The relatively high corrected total probe fluorescence (CTPF) observed in the fully functionalized microneedle (A, D), and the almost non-existent fluorescence in the two negative control samples (B, C, D), confirm the strong attachment of the fluorescence-labeled biotin (biotin-FITC) to the LBL-coated and streptavidin-functionalized microneedle. Although FITC has been reported to promote adsorption of FITC-labelled proteins <sup>208</sup>, the less pronounced fluorescence by biotin-FITC in the negative controls further emphasized the importance of the LbL base and EDC-cross-linked avidin in the LbL-biotin chemistry in determining the functionality of the probe.

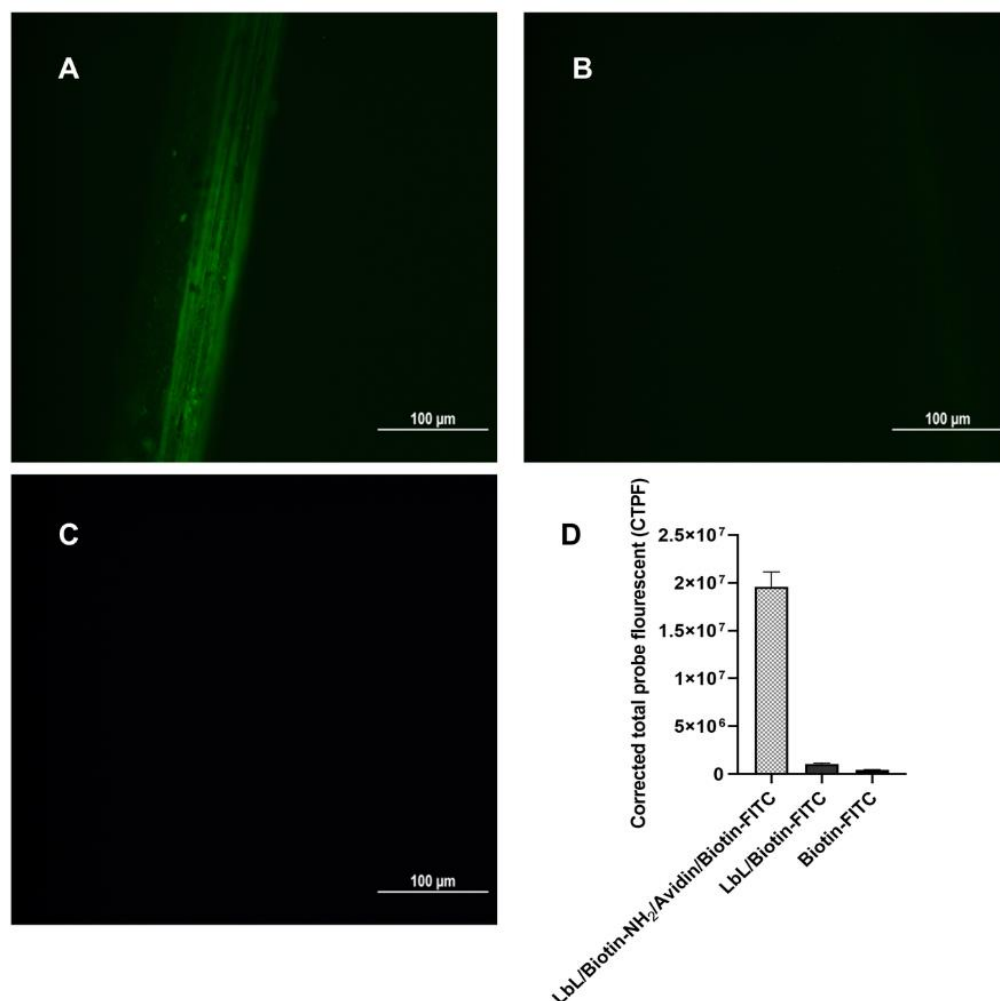


**Figure 3-3:** Fluorescent images confirming successful LBL assembly and Biotin immobilization on microneedles: (A) LbL+Biotin-EDC+Streptavidin+Biotin-FITC; (B) LbL+Biotin-FITC; (C) Biotin-FITC. (D) ImageJ analysis of the CTPF of A, B, C.<sup>54</sup>

## CHAPTER 4

# CALORIMETRIC SANDWICH-TYPE IMMUNOSENSOR FOR QUANTIFICATION OF TNF- $\alpha$ <sup>†</sup>

### 4.1 Background

Recent years have witnessed significant progress in the development of more efficient detection technologies for lab-on-a-chip immunoassays that provide increased sensitivity and specificity for point-of-care applications. Microfluidics immunosensors offer multiple advantages that include increased reaction rate, decreased time for incubation of the reactants, and reduced reagents and samples consumption. Miniaturization and integration of the multiple assay components allow automation, precise control of the fluid velocity, increased reproducibility, and the possibility for high-throughput analysis <sup>2</sup>. A wide range of detection technologies has been integrated with lab-on-a-chip biosensors for the quantification of analytes in biological and chemical samples. The optimal detection method provides high sensitivity coupled with low power consumption, simple fabrication, and minimal sample preparation <sup>3</sup>. Fluorescence, chemiluminescence, and electrochemiluminescence techniques provide detection sensitivities in the ng-pg mL<sup>-1</sup> range <sup>4</sup>. While these detection methods are well-

---

<sup>†</sup> This chapter has been published previously in **Biosensors and Bioelectronics** under the title as it is in chapter title. Volume 126 (2019), DOI: [10.1016/j.bios.2018.10.028](https://doi.org/10.1016/j.bios.2018.10.028). The current version has been formatted for this dissertation.

established, each of these techniques has limitations. Major drawbacks of the electrochemical detection technology are the effect of external factors such as pH, temperature, and ionic concentration on the performance of the assay <sup>12</sup>.

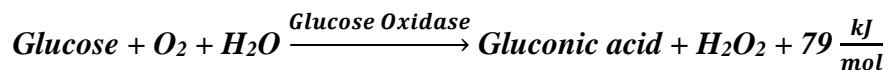
Calorimetric microfluidic systems with integrated miniaturized thermopile sensors are employed to measure small quantities of heat for biosensing applications. Here we report a calorimetric sandwich-type microfluidic immunoassay for detection and quantification of TNF- $\alpha$  using a thin-film thermopile that is attached to the lower channel wall of the device. The calorimetric immunosensor was fabricated using xurography, an inexpensive, rapid prototyping method for the manufacture of high aspect ratio microfluidic devices. Compared to other emerging low-cost benchtop technologies like 3D printers or laser cutters, “razor writing” of thin films is an attractive alternative for the fabrication of point-of-care devices. The described method uses a cutting plotter to create microstructures from adhesive tape in less than 3 minutes without photolithographic processes or chemicals. Simplicity and low cost of device fabrication that does not require special facilities such as clean rooms or specialized laboratory equipment for photolithographic processing of materials are advantages derived from this manufacturing technology. The sensor converts the temperature difference caused by the enzymatic reaction between glucose and glucose oxidase conjugated TNF- $\alpha$  detection antibody into an electric signal that is recorded by a nanovolt meter. The total amount of heat that is generated is proportional to the concentration of the analyte. The sensor is small in size (8mm $\times$ 8mm), light in weight, consists of 60 antimony-bismuth (Sb-Bi) thermocouple junctions and is relatively simple to fabricate. The miniaturized thermopile offers rapid response time and provides a self-generating signal that does not require

external power. The sensor operates without any control of external temperature because of its high common-mode thermal noise rejection ratio. The major advantages of the calorimetric immunosensor are the elimination of the control of light and signal development timing, a common requirement for conventional microplate-based TNF- $\alpha$  assays. Since calorimetric measurements are based on the detection of the heat released during an enzymatic reaction, the immunoassay can be performed with a wide range of enzyme-conjugated detection antibodies. The assay is performed in a flow-through system and unbound antibodies are washed away by the fluid in the microchannel. The design of the system allows the substrate to be introduced multiple times after the signal returns to baseline level to increase the statistical significance of the results.

## 4.2 Materials and methods

### 4.2.1 Principle of calorimetric immunosensing

Calorimetric quantification of TNF- $\alpha$  was successfully demonstrated in a microfluidic device with an integrated thin-film Sb-Bi thermoelectric sensor with a theoretical Seebeck coefficient of  $7.14 \mu\text{V mK}^{-1}$ . The technique is based on sandwiched immunodetection using a pair of matched antibodies that recognize different epitope sites of the TNF- $\alpha$  cytokine. The antibody-analyte complex was immobilized within the measuring junctions of the thermoelectric sensor. A fixed concentration of glucose (55 mM) was injected through a sample loop into the fluid flowing within the microfluidic device. The oxidation of glucose to gluconic acid by glucose oxidase generates  $79 \text{ kJ mol}^{-1}$  of energy<sup>209</sup>.



The enzymatic reaction increases the localized temperature at the measuring junctions of the thermopile in respect to the reference junctions and is proportional to the concentration of TNF- $\alpha$  that is measured in the cell culture medium of human astrocytes (Figure 4-1).

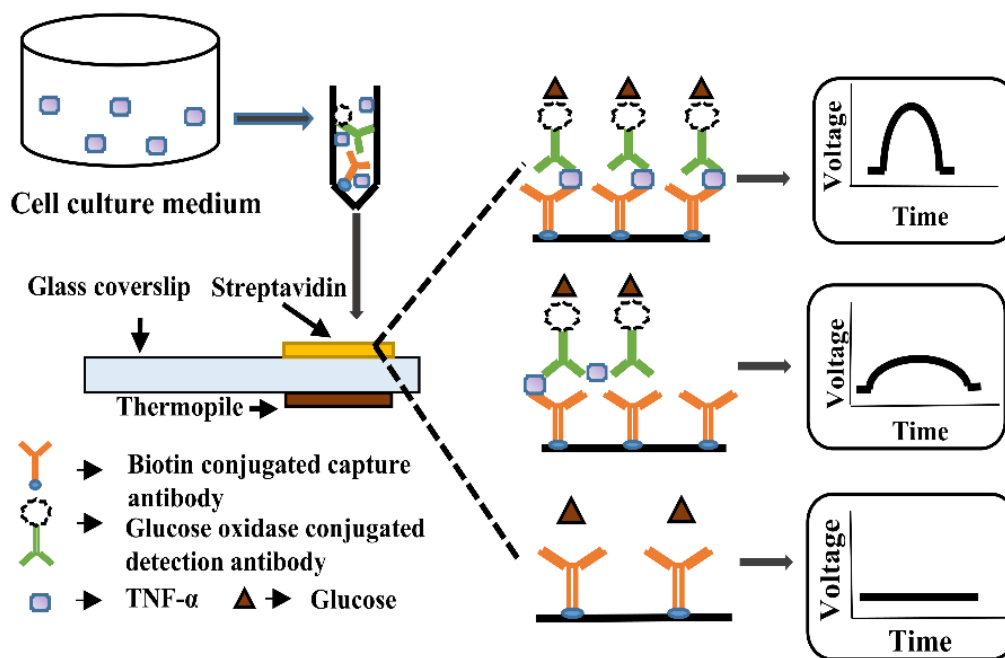


**Figure 4-1:** Principle of calorimetric immunosensing. The amount of heat released during the enzymatic reaction between the glucose oxidase conjugated detection antibody and glucose is proportional to the concentration of TNF- $\alpha$  in the biological sample<sup>83</sup>.

#### 4.2.2 Experimental set-up

A schematic of the calorimetric system for immunosensing is shown in **Figure 4-2**. Two syringe pumps (Harvard Apparatus, Holliston, MA) independently inject sodium acetate buffer through 0.01-inch internal diameter Teflon tubing (Upchurch Scientific, Oak Harbor, WA). A sample loop that has a volume of 13  $\mu$ L was loaded with 55mM glucose that was introduced into the inlet 2 buffer stream via a 6-port injection valve (V-451, Upchurch Scientific, Oak Harbor, WA). The thermal signature of the

enzymatic reaction is detected and converted by the thermopile sensor to an electric signal that was measured with a nanovolt meter (Agilent, model #34430A Loveland, CO). The output signal was recorded and processed using LabView SignalExpress software (National Instruments, Austin, TX). To prevent external electromagnetic interferences with the signal recording, the device and the nanovolt meter instrument were housed in a Faraday cage.

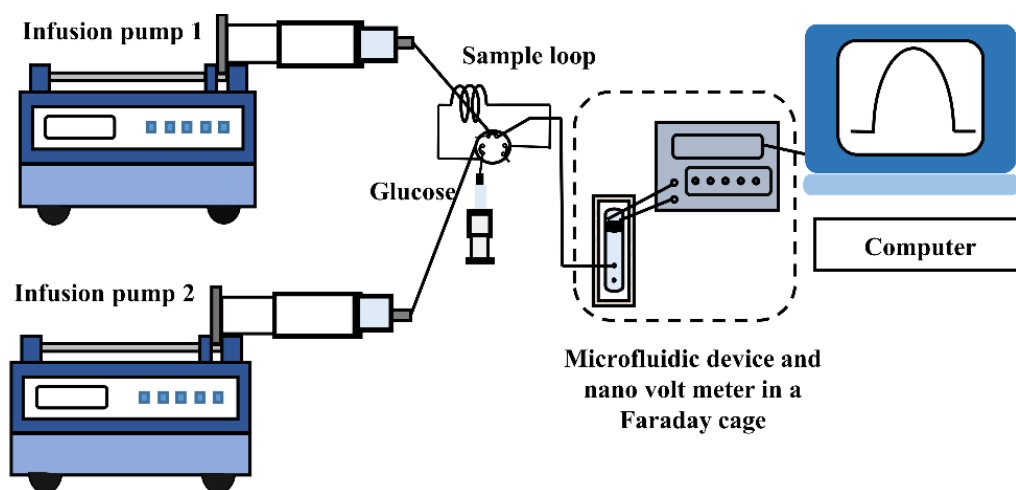


**Figure 4-2:** Schematic diagram of the setup for calorimetric immunosensing of TNF- $\alpha$  <sup>83</sup>.

#### 4.2.3 Fabrication of immunosensor

The microfluidic device has two inlets and a single outlet for independent injection of glucose and 50mM acetate buffer (pH 5.5) and was fabricated using a rapid-prototyping technique (**Figure 4-3A**). The channel of the device was designed using Adobe Illustrator software (Adobe, San Jose, CA) and was cut out of 100 $\mu$ m thick Kapton® tape using a cutting plotter (Graphtec America Inc, Santa Ana, CA). The dimensions of the channel were 65mm×12mm×0.1mm. The upper and lower channel walls consisted of 75mm×25mm×1mm microscope glass slide (VWR, Radnor, PA) and 75mm×25mm×0.17mm glass cover slip (Electron Microscopy Sciences, Hatfield, PA),



respectively. Streptavidin was immobilized to the lower channel wall of the device via a layer-by-layer self-assembly technique. The glass coverslip was cleaned with a 2% Micro 90 cleaning solution (Sigma Aldrich, St. Louis, MO). Five layers of alternating polyethyleneimine (50% w/v) and polyacrylic acid (35% w/v) (Sigma Aldrich, St. Louis, MO) were applied to a carboxylated layer of the surface of the device. EZ-Link™ NHS-PEG4 Biotinylating Kit (ThermoFisher Scientific, Waltham, MA) was used to functionalize the surface with streptavidin. The sensor (**Figure 4-3B**) was fabricated on 100µm polyimide tape using a Denton model DV-502B metal evaporation system (Denton Vacuum, Moorestown, NJ)<sup>43</sup> and was attached to the outer surface of the lower channel wall with a silver thermal compound (Arctic Silver Inc., Visalia, CA).

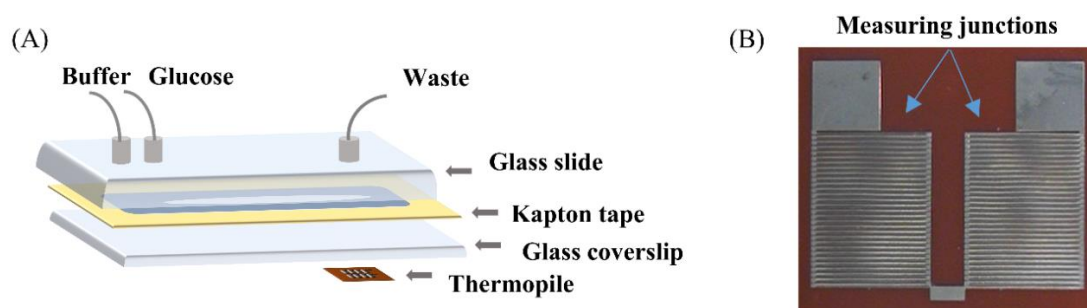


**Figure 4-3:** (A) Microfluidic device for calorimetric detection of TNF- $\alpha$ . (B) Image of thin-film Sb/Bi thermopile sensor. The reaction zone was located above the measuring junctions<sup>83</sup>.

#### 4.2.4 Calorimetric immunoassay procedure

Human TNF- $\alpha$  matched antibody pair kit (ab213467, Abcam, MA) was used for the quantification of the analyte. The capture antibody was conjugated to biotin while the detection antibody was labeled with glucose oxidase using a glucose oxidase conjugation kit (ab102887, Abcam, MA) according to the vendor guidelines. Cell culture supernatant from lipopolysaccharide (LPS) treated and non-treated human astrocytes (ScienCell

Research Laboratory, Carlsbad, CA) was collected, centrifuged at 2,000 g for 10 minutes to remove cell debris and stored at -20°C. A standard calibration curve was created using serial dilutions of synthetic TNF- $\alpha$  (0-2000 pg mL<sup>-1</sup>). Twenty  $\mu$ L of biotin linked capture antibody (2 $\mu$ g mL<sup>-1</sup>) and glucose oxidase conjugated detection antibody (0.5  $\mu$ g mL<sup>-1</sup>) were mixed with 20 $\mu$ L of synthetic TNF- $\alpha$  and incubated on an orbital shaker for 1 hour at medium speed. The same protocol was followed for the analysis of biological samples from cell culture supernatant from human astrocytes. The complex of the antibodies and the analyte was immobilized to the lower channel wall of the device via the biotin-streptavidin covalent bond. The dimensions of the reaction zone were 8mm $\times$ 3mm and were located directly above the measuring junctions of the sensor. Sodium acetate buffer was introduced through inlets 1 and 2 of the microfluidic device with a flow rate of 100 $\mu$ L min<sup>-1</sup> and 25 $\mu$ L min<sup>-1</sup> respectively. Glucose (55mM) was loaded into a 13 $\mu$ L sample loop and injected into the buffer stream of inlet 2 via an injection valve. The heat generated by the enzymatic reaction between the glucose and the glucose oxidase conjugated detection antibody increased the temperature at the measuring junctions of the thermopile. The magnitude of the voltage signal was calculated by integrating the area under the curve (AUC) versus the time profile using the Riemann Sums trapezoid rule. A standard calibration curve was generated by plotting the concentration of synthetic TNF- $\alpha$  versus the average AUC of the thermoelectric response. To evaluate the accuracy of the developed immunosensor, the concentration of cytokine in the cell culture supernatant was measured using human TNF- $\alpha$  ELISA kits (ab46087, Abcam, MA) according to the vendor's guidelines.

#### 4.2.5 Numerical analysis of glucose concentration as a function of the volumetric flow rate

The concentration of glucose along the width of the microchannel was modeled as a function of inlet 1 and inlet 2 fluid velocity. The simulations were performed using COMSOL Multiphysics 5.2a software. The developed two-dimensional stationary model was based on a microchannel with dimensions 65mm×12mm. The simulation results were obtained using the laminar reacting flow module coupled with the transport of diluted species module. The velocity distribution along the microchannel was assumed to follow Newtonian laminar flow. The fluid was considered incompressible with no-slip boundary conditions applied at all the walls. To run the simulation, a physics-controlled mesh with a finer element size was chosen. The dimensions of the microchannel and the fluid velocity parameters used in the simulations are listed in **Table 4-1**. The velocity of inlet 1 was constant while the velocity of inlet 2 was decreased to investigate its effect on the glucose distribution profile.

**Table 4-1:** Microfluidics dimensions and fluid flow model parameters.

Channel length	65mm
Channel width	12mm
Internal diameter of inlet and outlet	0.254mm (0.01 inch)
Glucose diffusion coefficient	$6.7 \times 10^{-10} \text{ m}^2 \text{ s}^{-1}$
Inlet 1 fluid velocity	$6.7 \times 10^{-4} \text{ ms}^{-1}$
Flow ratio	1,2, 4
Inlet 2 glucose velocity	$6.7 \times 10^{-4} \text{ ms}^{-1} / \text{Flow ratio}$
Reaction rate	$3 \times 10^{-7} \text{ mol m}^{-3} \text{ s}^{-1}$
Inlet temperature	293.15K
Outlet Pressure	0 atm
Mesh	Finer element size

### 4.3 Results and discussions

#### 4.3.1 COMSOL simulations of the glucose concentration profile

The COMSOL model has been used to characterize the distribution of the substrate along the width of the microchannel as a function of inlet 2 fluid velocity. The concentration of glucose within the reaction zone was proportional to the volumetric flow rate of inlet 2 and the ratio of the fluid velocities between both inlets (**Figure 4-4**).

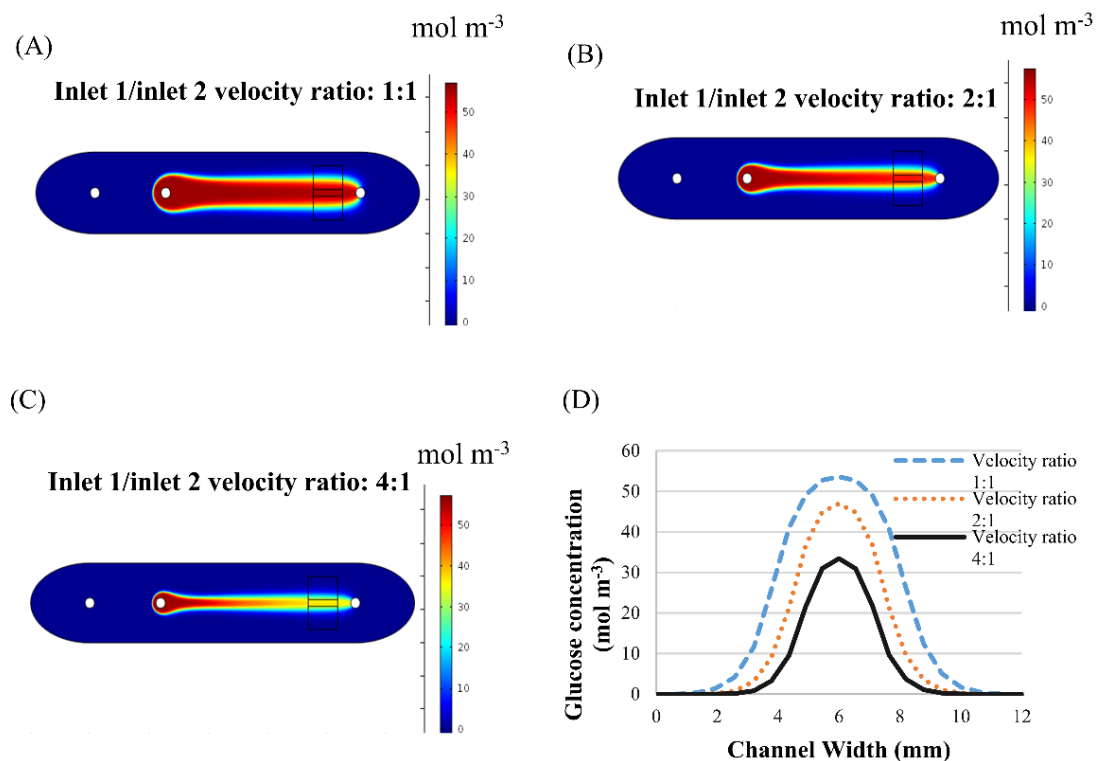


**Figure 4-4:** Glucose concentration profile along the width of the microchannel. Inlet 1 velocity is  $6.7 \times 10^{-4} \text{ m s}^{-1}$ . Inlet 2 flow velocity is: (A)  $6.7 \times 10^{-4} \text{ m s}^{-1}$ ; (B)  $1.67 \times 10^{-4} \text{ m s}^{-1}$ ; (C)  $0.84 \times 10^{-4} \text{ m s}^{-1}$ . (D) Graphical representation of glucose concentration along the width of the microchannel for various velocity flow ratios<sup>83</sup>.

The buffer supplied through inlet 2 was hydrodynamically focused within the measuring junctions of the thermopile by the fluid introduced through inlet 1. Change in the velocity ratio between both inlets affected the width of the glucose stream above the reaction zone. An increase in inlet 2 velocity resulted in a wider concentration profile of the substrate (**Figure 4-4A and B**). As a result, the substrate's variable width above the measuring junctions of the thermopile leads to an increase in the amount of heat that dissipates to the reference junctions of the sensor. The heating of the reference junctions leads to a decrease in the temperature difference and reduced voltage output of the sensor. The optimal flow rates ratio of 1:4 (**Figure 4-4C and D**) ensures that the substrate

was focused within the reaction zone and minimized the heat dissipation towards the reference junctions of the sensor. In the experiments, the concentration of glucose was in excess and was not a limiting factor for the enzymatic reaction.

#### 4.3.2 Standard calibration curve

Synthetic TNF- $\alpha$  (0 pg mL<sup>-1</sup>, 125 pg mL<sup>-1</sup>, 250 pg mL<sup>-1</sup>, 1000 pg mL<sup>-1</sup>, and 2000 pg mL<sup>-1</sup>) was serially diluted and incubated with the anti-TNF- $\alpha$  capture and glucose-oxidase conjugated detection antibodies to generate the standard calibration curve. Glucose was injected four times and the average area under the curve (AUC) of the voltage signal was calculated for each TNF- $\alpha$  concentration (**Table A 1 in Appendix**). The correlation coefficient (R) was estimated to be 0.9942 that indicates an excellent correlation between the response of the microfluidic calorimetric immunosensor and the concentration of the analyte (**Figure 4-5A**). The thermopile voltage increased as the concentration of the cytokine increased. The thermoelectric response showed a linear relationship with the TNF- $\alpha$  concentration in the range of 0 to 2000 pg mL<sup>-1</sup>. The thermopile response for various concentrations of TNF- $\alpha$  is shown in **Figure 4-5B**. A low-level signal was measured in the negative control experiments. It is hypothesized that the thermopile responds to small temperature changes caused by the friction between the buffers supplied by the inlets of the device.

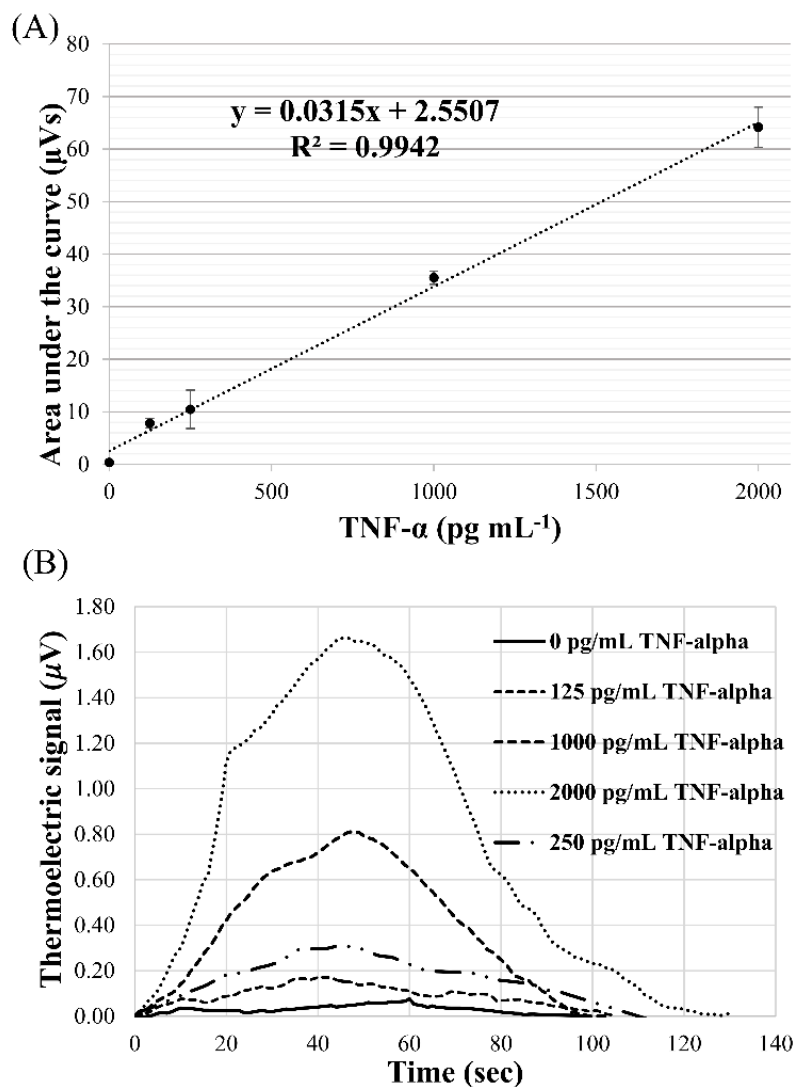


**Figure 4-5:** (A) Standard calibration curve for calorimetric microfluidic immunosensor. (B) Thermopile voltage output for various concentrations of synthetic TNF- $\alpha$ .<sup>83</sup>

The limit of detection (LOD) and limit of quantification (LOQ) of the calorimetric immunosensor were estimated from the slope of the calibration curve (0.0315) and the standard deviation of the blank (0.133) according to the following equations:

$$\text{LOD} = 3.3 \cdot \sigma / S$$

$$\text{LOQ} = 10 \cdot \sigma / S,$$

where  $\sigma$  is the standard deviation of the blank response and  $S$  is the slope of the calibration curve. The LOD of the calorimetric immunosensor was  $14 \text{ pg mL}^{-1}$  and the LOQ was  $42 \text{ pg mL}^{-1}$ . The detection and quantification limits of the fabricated microfluidic immunosensor are close to the values reported for the commercial absorbance-based ELISA kit of  $10 \text{ pg mL}^{-1}$  and  $30 \text{ pg mL}^{-1}$  respectively. The fabricated calorimetric microfluidic immunosensor has a lower LOD than those of previously reported fluorescent microfluidic sensors for quantification of TNF- $\alpha$  in serum ( $45 \text{ pg mL}^{-1}$ )<sup>35</sup> and in cell culture medium ( $20 \text{ pg mL}^{-1}$ )<sup>36</sup>.

#### 4.3.3 Stability and reproducibility study

The storage stability at  $4^{\circ}\text{C}$  of the calorimetric biosensor was evaluated over two weeks. The response to glucose ( $55 \text{ mM}$ ) showed no changes in the average enzymatic activity at the end of the period (**Figure 4-6A**).

Reproducibility analysis of within- and between assay variation was performed using three immunosensing devices ( $250 \text{ pg mL}^{-1}$  TNF- $\alpha$ ). The coefficient of variation between the assays was 0.99%. The intra-assay coefficient of variation for three different devices was 0.72%, 0.24%, and 0.47% respectively (**Table A 2 in Appendix**). Potential sources that add to the assay variation include minor differences in the Seebeck coefficient of the thermoelectric sensor, the position of the antibody/analyte complex within the junctions of the thermopile, as well as variations of the enzyme labeling efficiency of the detection antibody.



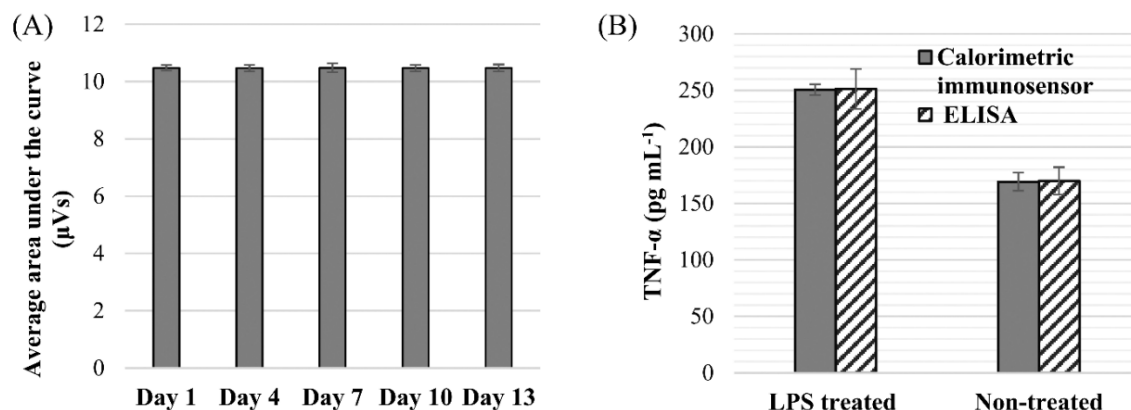


**Figure 4-6:** (A) Stability study for the developed calorimetric biosensor. (B) The concentration of TNF- $\alpha$  in the cell culture medium of lipopolysaccharide treated and non-treated human astrocytes were measured using conventional microplate-based ELISA and calorimetric immunosensor (n=4).<sup>83</sup>

#### 4.3.4 TNF- $\alpha$ concentration in cell culture medium

The feasibility of applying the sensor for analysis of biological samples was investigated via quantification of TNF- $\alpha$  in cell culture media samples and comparison of the levels measured using the microfluidic immunosensor and conventional ELISA. The equation of the standard calibration curve was used to calculate the concentration of TNF- $\alpha$  in the cell culture medium of non-treated and lipopolysaccharide (100 ng mL<sup>-1</sup>) treated human astrocytes using the calorimetric technique. The levels of the cytokine were measured using a conventional ELISA kit and the results were compared to assess the accuracy of the microfluidic platform (**Figure 4-6B**). The concentration of TNF- $\alpha$  in the cell culture medium of lipopolysaccharide treated and non-treated human astrocytes were measured using conventional microplate-based ELISA and calorimetric immunosensor (n=4). The concentration of TNF- $\alpha$  in lipopolysaccharide treated cells was 252 pg mL<sup>-1</sup> and 251 pg mL<sup>-1</sup> for absorbance ELISA and microfluidic immunosensor respectively. The levels of TNF- $\alpha$  in non-treated astrocytes measured using conventional

ELISA ( $170 \text{ pg mL}^{-1}$ ) and the microfluidic device ( $169 \text{ pg mL}^{-1}$ ) have less than 1% variation. The developed biosensor exhibited good selectivity as TNF- $\alpha$  determinations agreed well with the standard immunoassay analysis. The microfluidic immunosensor had lower inter-assay variability in comparison to absorbance-based microplate immunoassay. There was no significant difference between the results obtained by the two methods and therefore the proposed immunosensor can be reasonably applied for the analysis of biological samples.

#### **4.4 Conclusion**

This work describes the design, fabrication, and feasibility of a calorimetric immunosensor that uses thin-film thermopile to accurately determine the concentration of TNF- $\alpha$  in biological samples. The microfluidic device can detect low levels of heat and utilizes a glucose oxidase conjugated antibody as a novel method for sensitive detection of TNF- $\alpha$ . The assay is based on a sandwich-type immunoreaction where the enzymatic reaction between the substrate and the enzyme generates heat that is converted to an electrical signal by the sensor. The calorimetric immunosensor had a low limit of detection of  $9.88 \text{ pg mL}^{-1}$ . This novel calorimetric method for quantification of TNF- $\alpha$  could be easily extended for sensitive detection of various analytes in biological samples.

## CHAPTER 5

### NUMERICAL OPTIMIZATION OF KEY DESIGN PARAMETERS OF A THERMOELECTRIC MICROFLUIDIC SENSOR FOR ULTRASENSITIVE DETECTION OF BIOCHEMICAL ANALYTES<sup>†</sup>

#### 5.1 Background

Microfluidic technology enables rapid, sensitive, and accurate quantification and detection of analytes <sup>212</sup>. Microdevices are characterized by a large surface-to-volume ratio that allows precise, fully automated fluidic control and capability for high-throughput analysis <sup>213,214</sup>. Furthermore, lab-on-a-chip technology has reduced the cost of biochemical analysis by more than 90% compared to the commercially available enzyme-based quantification methods <sup>215</sup>. The fabrication of highly sensitive microfluidic platforms requires a detailed understanding of the interaction between fluid and microchannel materials and the selection of design parameters that provide superior accuracy, efficiency, and limit of detection <sup>216,217</sup>. The complexity of the micro- and nanoscale processes makes it difficult to experimentally investigate the impact of a single mechanism. Therefore, numerical simulations enable the assessment of the effect of single or multiple parameters on the performance of the platforms under study. Modeling

---

<sup>†</sup> This chapter or portions thereof has been published previously in the **ASME Journal of Thermal Science and Engineering Applications** under the title as it is in chapter title. Volume 13 (2021), DOI: [10.1115/1.4047826](https://doi.org/10.1115/1.4047826). The current version has been formatted for this dissertation.

of the thermophysical characteristics of the system allows the selection of the optimal design factors that provide enhanced performance <sup>218,219</sup>.

Calorimetric microfluidic platforms have been used for the detection of and quantification of biochemical processes. An integrated thermoelectric sensor measures the heat released during the enzymatic or chemical reaction and converts it to an electric signal. This technology uses small sample volumes, provides quick response times, and has a simplified detection approach. Due to the remarkable common-mode thermal noise rejection capabilities, thin-film thermopiles are suitable for sensing very small temperature changes <sup>220</sup>. Moreover, calorimetry is compatible with most biochemical processes as most of these reactions are exothermic or endothermic and are associated with temperature change. Microscale thermoelectric devices have been employed to measure temperatures in the range of mK- $\mu$ K for characterization of the thermodynamic properties of biomolecules <sup>221</sup> and metabolites measurement <sup>222</sup>. Thermoelectric sensors have been successfully used for quantification of TNF- $\alpha$  <sup>83</sup>, modified nucleobases <sup>214</sup>, monitoring the metabolic rate of bacteria <sup>41</sup>, detection of enzymatic reactions <sup>44</sup>, measurement of DNA and protein binding affinity <sup>45</sup>, detection of nucleotide incorporation <sup>43</sup>, and DNA hybridization events <sup>223</sup>. Because the calorimetric detection method is universal, it can be applied for assays that cannot be performed using other techniques <sup>224</sup>.

Microfluidic calorimeters are characterized by large surface-to-volume ratios and have increased heat and mass transfer efficiencies. However, the suitability of ultra-low sample volume thermoelectric sensors suffers from their low volume-specific sensitivity. A central challenge in using microfluidic systems for thermoelectric measurements is

optimizing the design parameters of the device that includes flow rate, sample volume, and microchannel material properties to increase the sensitivity and specificity of the platform <sup>225</sup>. Parasitic heat transfer in microcalorimetry results in heat loss to the substrate that decreased the overall heat transfer to the thermoelectric sensor. Numerical and experimental analysis using a glass fabricated device confirmed that depositing the thermopile sensor directly on a lower channel wall decreases the thermal resistance between the heat source and thermopile and increases the rate of heat transfer per temperature change by 6.5 times <sup>226</sup>. The effect of thermal asymmetry on thermopile sensitivity was modeled and experimentally validated. The results from this study suggest that there is an optimal thermopile position within the microchannel and this position is influenced by the flow ratio <sup>227</sup>. Numerical simulations indicated that a decrease in signal-to-noise ratio with increasing chamber height is caused by the changes in the sensitivity gradient inside the reaction chamber <sup>228</sup>. A microfluidic calorimeter with an integrated thermopile was modeled to investigate the effect of flow rates on glucose oxidase enzymatic reaction. This study confirmed that flow rates were inversely related to convective heat loss and, therefore, reduced the thermopile response <sup>229</sup>. The relationship between the fluid velocity, sample volume, and the signal output in a thermoelectric microfluidic device was analyzed. Results indicated that the signal duration and magnitude had an inverse relation with the fluid flow rate. As fluid velocity increases, the ratio of convective heat loss to conductive heat transfer towards the measuring junction of the sensor increased. Since more of the generated heat is lost to the moving fluid, the maximum temperature over the measuring junctions is decreased <sup>220</sup>.

In this chapter, a detailed, three-dimensional numerical modeling of a continuous-flow microfluidic thermoelectric biosensor is presented. The critical design parameters that provide the maximum signal output are discussed. The governing equations for the numerical analysis and the design of the device are presented and the simulation results were compared with the experimental measurements that were recently published<sup>83</sup> and reported in **CHAPTER 4**. The cumulative effect of multiple factors on the heat distribution within the microchannel and the rate of heat transfer to the sensor were simulated using the “laminar flow”, “transport of the diluted species”, and “heat transfer” modules in COMSOL Multiphysics 5.4. Conjugate heat transfer analysis was performed to identify the optimal parameter combination that provides maximum sensitivity. The factors that heavily determine the performance characteristics of the thermal microfluidic device include channel height, physical properties of the device materials, inlets flow rates ratio, and the presence of a heat sink in contact with the reference junctions of the thermopile.

## 5.2 Methodology

### 5.2.1 Numerical simulations

The microfluidic continuous-flow thermal sensing platform, the thermopile, and the aluminum holder used as a heat sink are shown in **Figure 5-1**. The device had two inlets and a single outlet. The reaction zone for the enzymatic reaction between glucose and glucose oxidase was positioned directly above the measuring junctions of the thin-film antimony-bismuth (Sb-Bi) thermopile. Water flow was simulated in inlet 1 while a 13 $\mu$ L glucose bolus injection (55mM) was simulated in inlet 2 (**Figure 5-1a**). In this numerical model, water was used as a replacement of phosphate buffer solution pumped

through inlet 1, which was used for the experiments, due to the similarities in fluid properties. The chemical reagents are transported in the microfluidic device via the motion of fluids that can be efficiently controlled by flow-focusing inside the microchannel. The inlet 2 flow rate affects the sample transient time and the duration of the signal, while the fluid velocity ratio between the two inlets focuses the glucose stream hydrodynamically over the measuring junctions of the thermopile. The enzyme (glucose oxidase) that defines the reaction zone (8mm×3mm) is positioned on the inner surface of the lower channel wall directly above the measuring junctions of the sensor. The substrate (glucose) was introduced through inlet 2 and hydrodynamically focused to flow over the measuring junctions of the sensor. The enzymatic reaction occurs when the substrate reaches the enzyme-defined reaction zone. The thickness of the upper channel wall was 1 mm, and the thickness of the lower channel wall was 175μm. The thermoelectric sensor (8mm×8mm×100μm) had 60 thermocouple junctions and a theoretical Seebeck coefficient of 7.14μV mK<sup>-1</sup> (**Figure 5-1a**).

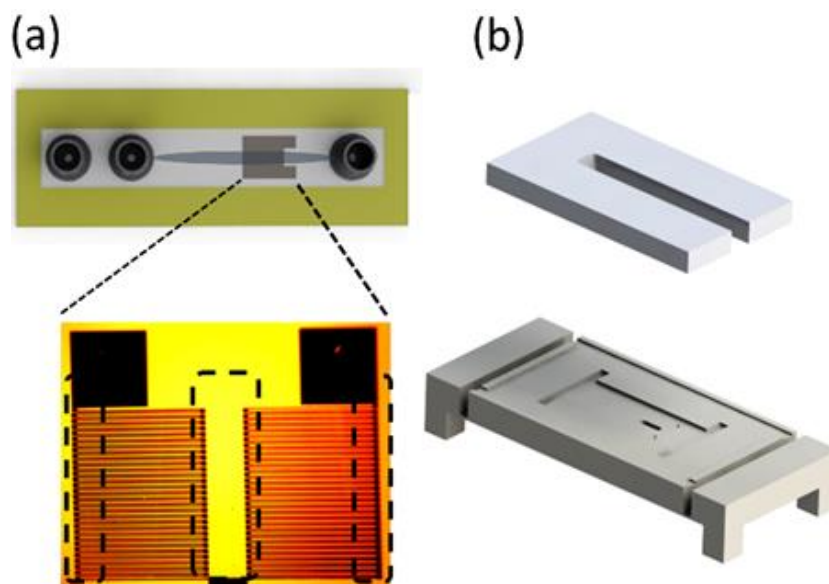


**Figure 5-1:** (a) Schematic of the microfluidic device with an integrated thermoelectric sensor. Hydrodynamically focused glucose introduced through Inlet 2 flows directly above the measuring junctions of the sensor. (b) Schematic of the aluminum holder. The reference junctions of the thermopile are in contact with the aluminum block that serves as a heat sink while the measuring junctions of the thermopile and the reaction zone are position directly above the air gap.<sup>230</sup>

The thermopile was positioned to the outer surface of the lower channel wall.

The measuring junctions of the thermopile are located underneath the reaction zone and the hydrodynamically focused glucose stream provided by inlet 2. The reference junctions of the sensor were positioned below the water stream supplied by inlet 1. The design of the device and the thermopile ensures that the heat generated by the enzymatic reaction is transferred through the lower channel wall to the thermopile measuring junctions by conductive heat transfer. When the heat reaches the thermopile, the temperature of the measuring junctions increases relative to that of the reference junctions and generates a Seebeck voltage.

Two categories of simulations were performed: one where the reference junctions were in contact with a heat sink that maintained a constant temperature of 293.15 K, and



one simulation without a heat sink. A schematic diagram of the aluminum heat sink is shown in **Figure 5-1b**. While the heat sink maintains a constant temperature at the reference junctions, it also absorbs the heat that dissipated from the reaction zone and impacts the magnitude of the thermoelectric output of the sensor. The heat released by the enzymatic reaction increased the temperature of the measuring junctions relative to the reference junctions. The temperature difference between the junction sets was converted to a voltage by the thermopile. The theoretical voltage output was determined using the simulated temperature difference and the theoretical Seebeck coefficient of the thermopile.

COMSOL Multiphysics 5.4 was used to solve continuity, Navier-Stokes, and energy equations for both fluid and solid subdomains simultaneously. The enzymatic reaction between glucose oxidase conjugated detection antibodies and glucose occurred within the reaction zone and generated heat. Therefore, the heat source for the study was a function of the glucose oxidase and glucose concentrations, the reaction rate constant, and the rate of heat generation. A summary of the parameters' nomenclature used in the governing equations is given in **Table A 4 in the Appendix**. The values of the parameters used in the equations are listed in **Table A 3** and the characteristic material properties are included in **Table A 5**.

The time-dependent simulations of the temperature distribution and glucose profile were performed for 240 seconds. A step function was used to increase the glucose concentration at  $t=0$  to 55mM followed by a step down to  $c_g=0$  concentration after 13 $\mu$ L was introduced into the inlet 1 fluid stream. The inner surface of the microchannel was modeled with non-slip boundary conditions according to the continuum assumption

applicable for microscale fluid flow. The “laminar flow” module was conjugated with the “transport of diluted species” and “heat transfer” modules in COMSOL. The “transport of diluted species” module was used to simulate the flow of glucose within the microchannel. The “heat transfer” module was used to calculate the temperature difference between the measuring junctions and the reference junctions of the thermopile.

The working fluid, water, was assumed to be incompressible, and continuum flow (Knudsen number  $< 10^{-3}$ ) of the fluid was considered. Therefore, the Navier-Stokes equation and the continuity equation were solved with the laminar flow interface. To account for the conservation of momentum and conservation of mass, it was assumed that the device was perfectly insulated. The governing equations (Navier-Stokes and continuity, respectively) for fluid flow are as follows:

$$\rho_f \frac{\partial u}{\partial t} + \rho_f U \cdot \nabla(U) = -\nabla p + \nabla \cdot [\mu(\nabla U + \nabla U^T)] + F_b \quad (\text{Eq. 3-1})$$

$$\nabla \cdot U = 0 \quad (\text{Eq. 3-2})$$

The fluid velocity at the inlets was set to be a non-zero value to drive the fluid inside the microchannel according to the following equation:

$$u_{in} = \frac{u_m}{\rho_f} \quad (\text{Eq. 3-3})$$

The outlet of the device was maintained at atmospheric pressure ( $p = 0$ ):

$$p_{out} = 0 \quad (\text{Eq. 3-4})$$

The diffusion flux of the diluted species was included with the convective flux due to the bulk fluid motion inside the microchannel. Therefore, diffusive and convective mass transports were considered to account for the flow of glucose inside the microchannel:

$$\frac{\partial c_g}{\partial t} = \nabla \cdot (D_g c_g) - U \cdot \nabla c_g \quad (\text{Eq. 3-5})$$

The device was modeled as perfectly insulated and the rate of thermal radiation was assumed to be negligible. According to the first law of thermodynamics, the equation for conservation of total internal energy of an infinitesimal volume of fluid was expressed as:

$$\frac{\partial}{\partial t} \left[ \rho \left( \Delta E + \frac{1}{2} u^2 \right) \right] + \nabla \cdot \left[ \rho U \left( \Delta E + \frac{1}{2} u^2 \right) \right] = -\nabla \cdot q + \nabla \cdot (\sigma \cdot U) + \rho U \cdot F_b \quad (\text{Eq. 3-6})$$

The rate of change in energy per unit volume and the convection of energy due to fluid flow was defined on the left side of the equation. The total heat flux, the work done by the surface forces, and the total work done by the body forces were defined on the right side of the equation. Expressing the total stress tensor,  $\sigma$ , in terms of pressure ( $p$ ) and the viscous stress tensor ( $\tau$ ), were obtained as follows:

$$\nabla \cdot (\sigma \cdot U) = -\nabla \cdot (pU) + \nabla \cdot (\tau U) \quad (\text{Eq. 3-7})$$

Substituting the value for the work done due to the surface forces in **Eq. 3-6** yields:

$$\frac{\partial}{\partial t} \left[ \left( \rho \frac{1}{2} u^2 \right) \right] + \nabla \cdot \left[ \left( \rho U \frac{1}{2} u^2 \right) \right] = -\nabla \cdot q + U(\nabla \cdot p) + U \cdot (\nabla \cdot \tau) + \rho U \cdot F_b \quad (\text{Eq. 3-8})$$

**Eq. 3-8** can be expressed in terms of enthalpy according to the following equation:

$$\rho \frac{\partial h}{\partial t} + \rho U \cdot \nabla h = -\nabla \cdot q + U \cdot \nabla p + \frac{\partial \rho}{\partial t} + \tau \cdot \nabla U + Q \quad (\text{Eq. 3-9})$$

The heat source was defined as a function of the reaction rate constant, the concentration of glucose and glucose oxidase within the reaction zone, and the reaction energy.

$$Q = k_g \times c_{Gox} \times c_g \times E_g \quad (\text{Eq. 3-10})$$

The conduction heat flux vector,  $q$ , was defined from Fourier's conduction law as:

$$q = -k\nabla T \quad (\text{Eq. 3-11})$$

The conservation of the enthalpy equation was expressed in terms of temperature,  $T$ , and pressure,  $p$  as follows:

$$dh = c_p dT + \frac{1}{\rho} [1 - T\beta] dp \quad (\text{Eq. 3-12})$$

Replacing the enthalpy value in **Eq. 3-9** yields the temperature equation as:

$$\rho c_p \frac{\partial T}{\partial t} + \rho c_p U \cdot \nabla T = \nabla \cdot (k\nabla T) + \beta T \left( \frac{\partial p}{\partial t} + U \cdot \nabla p \right) + \tau \cdot \nabla U + Q \quad (\text{Eq. 3-13})$$

Since the working fluid was assumed to be incompressible, the pressure term in **Eq. 3-13** can be eliminated. Considering this condition, the equation for temperature was finally simplified to:

$$\rho c_p \frac{\partial T}{\partial t} + \rho c_p U \cdot \nabla T = \nabla \cdot (k\nabla T) + \tau \cdot \nabla U + Q \quad (\text{Eq. 3-14})$$

The simulations were performed for 13  $\mu\text{L}$  of 55 mM glucose that was introduced through inlet 2 while inlet 1 carried a water solution. The temperature difference between the measuring and reference junctions was converted to a voltage output using the theoretical Seebeck coefficient value of the antimony-bismuth (Sb-Bi) thermopile sensors ( $\alpha = 7.14 \mu\text{V mK}^{-1}$ ) according to the following equation:

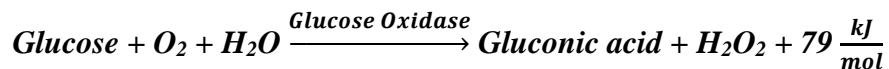
$$\Delta V = \alpha \Delta T \quad (\text{Eq. 3-15})$$

A step function that describes the glucose concentration was defined to ensure that the flow of glucose stopped after the sample was introduced in the microfluidic channel, at which point a glucose-free water solution continued to be injected into inlet 2 using the same flow rate as the glucose stream, similar to the bolus injection used in the actual

experimental procedure. This was done to ensure that the accuracy of the model can be evaluated, and the simulation results can be compared with the experimental values. A parametric sweep was performed for a comparative analysis of the various parameters.

### 5.2.2 Experimental set up for thermoelectric biosensor

The integration of the microfluidic device with a fluid delivery platform and the data acquisition system was described in a previously published work. The microfluidic thermoelectric platform was successfully used for accurate quantification of TNF- $\alpha$  concentration<sup>83</sup>. Briefly, the detection antibody was conjugated to glucose oxidase and the antibody-analyte complex was immobilized at the inner surface of the lower channel wall, directly above the measuring junctions of the thermopile sensor. Glucose (55mM) was injected through a 13 $\mu$ L sample loop into the inlet 2 fluid stream and was converted by the enzyme to gluconic acid and hydrogen peroxide. The enzymatic reaction generates heat at a rate of 79 kJ mol<sup>-1</sup><sup>209</sup>:



The flow rate for inlet 1 (water) and inlet 2 (glucose) were 100 $\mu$ L min<sup>-1</sup> and 25 $\mu$ L min<sup>-1</sup>, respectively. The reference junctions of the sensor were maintained in contact with an aluminum heat sink to maintain a constant temperature. The heat of the enzymatic reaction increased the temperature of the measuring junctions relative to the reference ones. The thermopile converted the temperature difference into an electric signal that was recorded by a nanovolt meter.

### 5.3 Results and discussions

#### 5.3.1 Experimental validation of the numerical model

Experimental study <sup>83</sup> was used to verify the proposed three-dimensional numerical model for time-dependent analyses of temperature distribution within the microchannel of the device. The simulation results indicated an excellent correlation with the experimental data in predicting the maximum voltage output. The microfluidic channel had a rectangular cross-section (65mm×12mm) and was fabricated using rapid prototyping by sandwiching a patterned adhesive tape between the upper and lower channel walls. A thin-film thermopile was attached to the outer surface of the lower channel wall and the reference junctions of the device were maintained in contact with an aluminum heat sink. Both the experimental and the theoretical analyses were performed in a device that had upper (75mm×25mm×1 mm) and lower (75mm×25mm×170 μm) walls formed out of glass material. The device had 2 inlets and a single outlet. The microfluidic channel height was 100 μm and 13 μL of glucose (55mM) was introduced through inlet 2. A phosphate-buffer saline solution was introduced through inlet 1 and inlet 2 after the glucose bolus injection.

The pattern of fluid flow inside the microchannel is determined using a dimensionless constant, Reynolds number. Examining the velocity profiles for the various cases studied the maximum velocity in the microfluidic channel was 10 mm sec<sup>-1</sup> corresponding to local Reynolds number of 10<sup>-4</sup> indicating a laminar flow. The simulations and the experimental studies were performed for a total of 240 seconds to allow for the heat within the reaction zone to dissipate and the signal to return to a baseline level. The time-dependent concentration of glucose within the microchannel was

assessed on the bottom of the channel (XY-plane) at 0, 40, 80, and 120 seconds after the injection of glucose (**Figure 5-2**). The maximum thermopile output in the experimental results is reached 80 seconds from the injection of the substrate within the fluid flow.

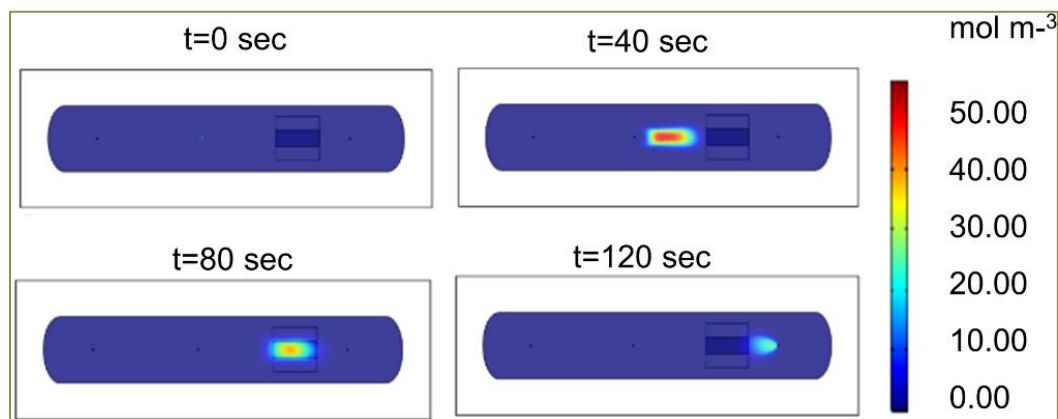


**Figure 5-2:** Glucose concentration profiles and locations of the bolus injection relative to the reaction zone at 0, 40, 80, and 120 seconds. The fluid flow rates for inlet 1 and inlet 2 were  $100\mu\text{L min}^{-1}$  and  $25\mu\text{L min}^{-1}$ , respectively.<sup>230</sup>

The theoretical voltage output of the sensor reached a maximum value of  $1.66\mu\text{V}$  at 80 seconds after the injection of the glucose in the channel of the device. The experimental value of the thermopile response obtained using the same parameters was  $1.67\mu\text{V}$ . The numerical simulations show a good correlation between the simulated and experimental position of the glucose flow relative to the reaction zone (**Figure 5-3**). The predicted and the experimental values for the peak height and signal duration are in close agreement. The standard error of the area under the curve for the experimental measurements was less than 1% of the signal response. The average temperature change derived from the Seebeck coefficient, and the voltage output of the sensors was  $0.26\text{mK}^{83}$ .

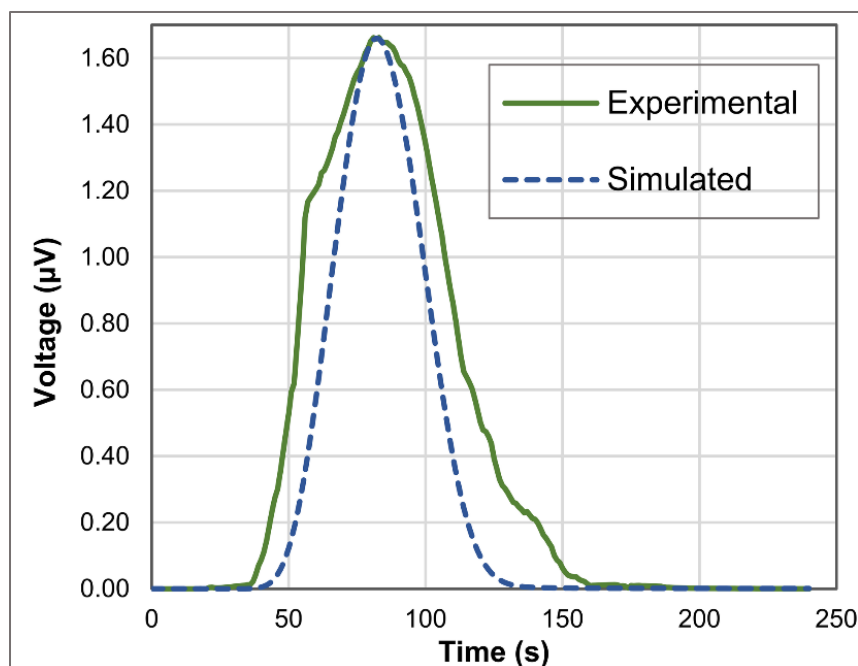


**Figure 5-3:** A comparison between the numerical and experimental voltage signal of the thermopile sensor. The upper and lower channel walls of the device were fabricated out of glass. The fluid flow rates for inlet 1 and inlet 2 were  $100\mu\text{L min}^{-1}$  and  $25\mu\text{L min}^{-1}$ , respectively.<sup>230</sup>

The model considers that the enzymatic reaction occurs within the fluid directly above the measuring junctions of the thermopile sensor. By controlling the ratio of the flow rates of the two inlets, the second inlet (i.e., the middle flow) can be hydrodynamically focused to flow directly over the measuring junctions. Since the glucose is only present as bolus injection in the second inlet, the chemical reaction between the glucose and glucose-oxidase bound-antibodies only occurs over the measuring junctions. Likewise, the outer flow over the reference junctions provided sufficient convective heat transfer to keep the reference junction at a constant temperature (i.e., room temperature of the water in the device). The experimental studies were performed at the surface of the lower channel wall. The enzyme was immobilized directly above the thermoelectric sensor and the substrate was introduced within the fluid flow. In



the experimental studies, a solution containing the glucose-oxidase conjugated antibodies is immobilized to the glass channel wall directly above the measuring junctions of the thermopile (i.e., the middle of the thermopile). The sensor is attached to the opposite (flipped) side of the lower channel wall <sup>83</sup>. The mathematical model replicates the environment by applying an exothermic reaction condition on a designated surface on the inner side of the bottom channel surface directly above the measuring junctions of the thermopile. The hydrodynamically focused flow carrying the substrate (as mentioned previously) maintains the width of the reaction zone constant over the measuring junctions. It is noted that the designated “reaction zone” used in the model is wider than the hydrodynamically focused flow (in all cases studied) so that an inaccurate forced condition is not present in the experimental study would not affect the results. This accounted for the increased width of the experimental signal relative to the simulated results. The developed 3D model was subsequently used for investigating the impact of the channel height, fluid velocity, physical properties of the device material, and heat sink on the thermopile output.

A time-step independence study was conducted with time-steps varying from 0.25sec to 5sec over a window between 0 and 240sec. The time-step independence study shows that for a time-step of 1sec (the value used for this study which provides an excellent correlation in finding the peak voltage difference) a peak voltage difference value is obtained that diverges from the converged value (seen at the smaller time steps) by less than 1% by reducing the simulation time by more than half. An increase in the time step from 0.25s to 5s results in increasing the peak voltage value by 2.8%. Therefore, the choice of the time step as 1sec for this study is justified as it provides an

accurate correlation with the experimental study and at the same time requires a reasonable amount of simulation time. The model under study incorporated a physics-controlled finer mesh specifically around the physics modeled in this study and the Multiphysics tools used to create the model simulations (laminar fluid flow, mass transport of diluted species, and heat transfer in a fluid/solid). Because of this, the software automatically selects tighter meshes (i.e., smaller elements) in areas where a higher resolution is needed (e.g., entrance and exit effects of fluid flow, regions where exothermic reactions occurred, etc.).

### 5.3.2 Effect of microfluidics channel height

The simulation analysis of the effect of channel thickness (50  $\mu\text{m}$ , 100  $\mu\text{m}$ , 150  $\mu\text{m}$ , and 200  $\mu\text{m}$ ) was performed for a microfluidic device that had upper and lower channel walls formed of glass. The flow rate for inlets 1 and 2 was 100  $\mu\text{L min}^{-1}$  and 25  $\mu\text{L min}^{-1}$  respectively. An increase in the channel height from 50  $\mu\text{m}$  to 200  $\mu\text{m}$  resulted in a decrease of the predicted signal from 2.45  $\mu\text{V}$  to 0.73  $\mu\text{V}$ . An increase in channel height affected the thermopile voltage output signal in two ways: by lowering the amplitude of the signal and by increasing the duration (i.e., width) of the signal response. This study assesses the impact of the parameters that will maximize the area under the curve (AUC) of the voltage signal. The two effects on the voltage signal that varying the channel height have opposed each other; a decrease in the amplitude would result in a lower AUC, whereas an increase in the signal duration would increase the AUC. Through the analyses of the numerical model, it was determined that the loss in AUC from a decrease in the signal amplitude exceeds any gains brought on by the increase in signal duration. Because of this, the primary focus of this study was to analyze the signal

amplitude as the desired metric to optimize. The increase of the channel height results in a larger cross-sectional surface area that leads to a reduced velocity of the glucose solution inside the reaction zone. This contributes to a longer response time of the thermopile sensor with a decrease in the magnitude of the voltage output (**Figure 5-4**). Additionally, the decrease of the channel height reduces the residence time of the heat within the reaction zone and decreases the rate of lateral heat dissipation from the measuring junctions towards the reference junctions of the thermal sensor. Therefore, the thermoelectric voltage is increased.

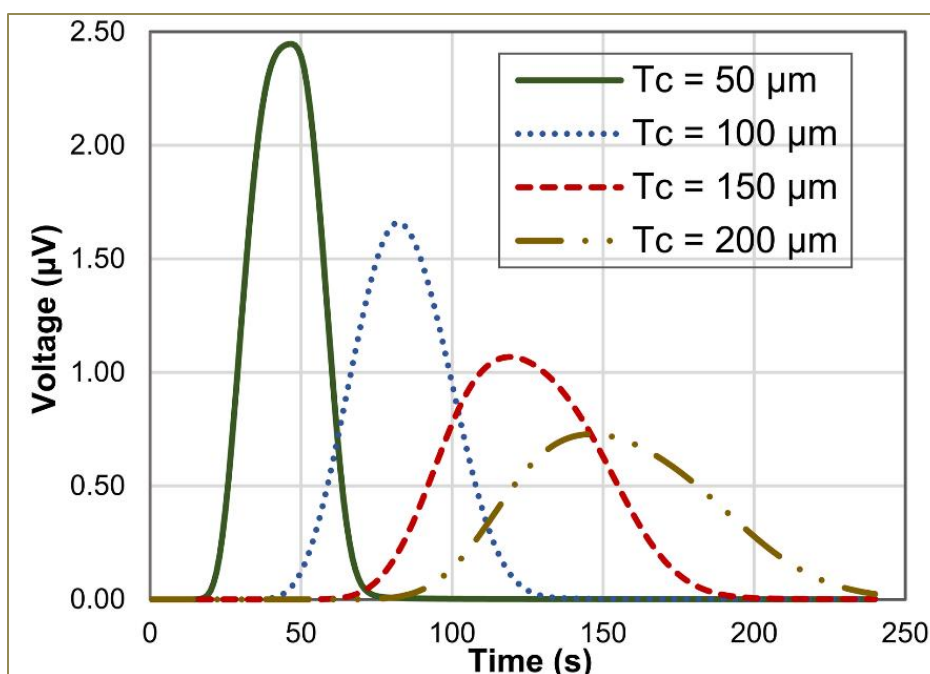


**Figure 5-4:** Mathematical simulations of thermopile voltage output as a function of microfluidic channel height ( $T_c$ ). The upper and lower channel walls of the device were fabricated out of glass. The fluid flow rates for inlet 1 and inlet 2 were  $100\mu\text{L min}^{-1}$  and  $25\mu\text{L min}^{-1}$ , respectively.<sup>230</sup>

### 5.3.3 Effect of inlets flow rate ratio

The optimal fluid flow rate ratio between inlet 1 and inlet 2 ensures that the fluid introduced at inlet 2 (glucose) is hydrodynamically focused within the reaction zone just above the measuring junctions of the thermopile. Color-dye experiments indicated that the width of the inlet 2 flow is affected by the flow rate ratio between inlet 1 and inlet 2. These experimental results confirmed that the width of the glucose stream increased from 3mm to 4mm as the fluid flow rate ratio between inlet 1 and inlet 2 decreased from 4:1 to 2:1 (data not shown). Numerical simulations were performed to analyze the change in the duration and magnitude of the thermopile output as a function of the fluid velocity between inlet 1 and inlet 2. Inlet 1 flow rate was maintained constant at  $100\mu\text{L min}^{-1}$  while the flow rate of inlet 2 was reduced from  $50\mu\text{L min}^{-1}$  to  $25\mu\text{L min}^{-1}$ . An increase in

the flow rate increased the sample's transient time to the reaction zone. The changes in the width of the reaction area impact the distance between the enzymatic reaction (heat source) and the reference junctions of the thermopile that are in contact with the heat sink. Therefore, reducing the lateral thermal diffusion affected the amount of heat that dissipated to the reference junctions. A decrease in the thermal difference between the junction sets causes a reduction in the voltage (**Figure 5-5**).

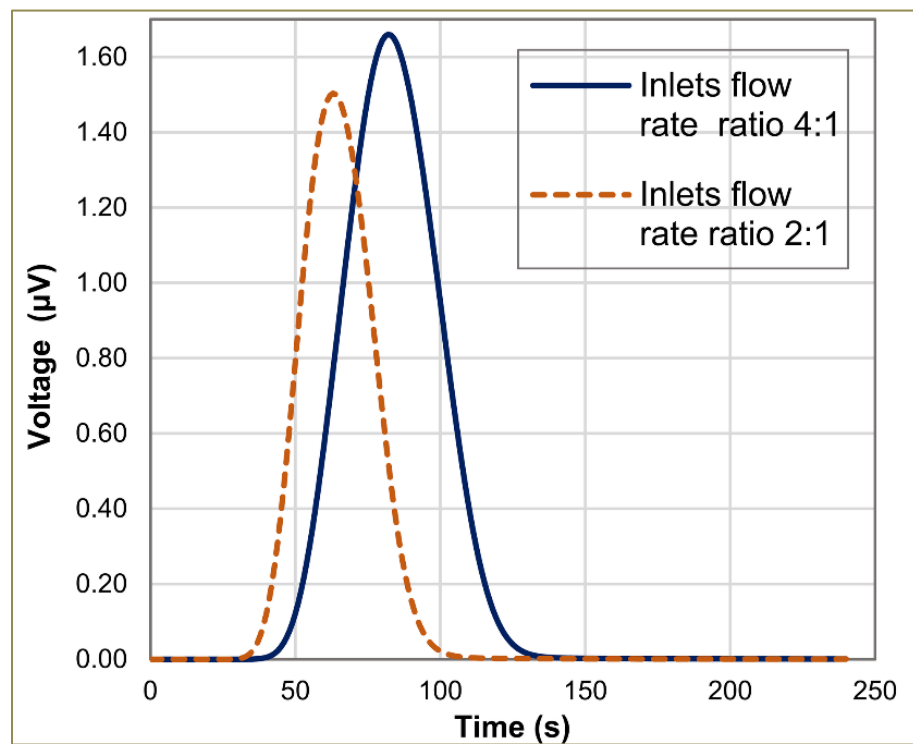


**Figure 5-5:** Numerical analysis of the effect of inlet flow rate ratio on the thermopile voltage output. The channel height was 100µm and the upper and lower channel walls were formed out of glass.<sup>230</sup>

#### 5.3.4 The relationship between material thermal properties, heat sink, and thermoelectric signal

A numerical analysis was performed to investigate the impact of material thermal properties on the magnitude of the thermoelectric voltage output. The simulations were

performed for a device that had a channel height of 50  $\mu\text{m}$  and upper and lower wall thicknesses of 1mm and 170  $\mu\text{m}$ , respectively. The mathematical analysis of heat transfer was performed using the following combinations of materials for the upper and lower channel wall: glass, polydimethylsiloxane (PDMS), and polymethyl methacrylate (PMMA). To understand the impact of keeping the reference junctions of the sensor under temperature control and in contact with an aluminum block, the thermal difference between the junctions of the sensor was analyzed with and without a heat sink. When the reference junctions of the sensor are maintained under constant temperature control, the heat that dissipates laterally from the reaction zone is transferred towards and absorbed by the aluminum heat sink. Adding a heat sink in contact with the reference junctions of the sensor ensures that the reference junctions are kept at a constant temperature. However, the results indicate that keeping the reference junctions of the sensor in contact with a heat sink results in lower average temperatures difference between the junction sets of the sensor that reduces the sensitivity of the calorimeter (**Figure 5-6 and Figure A 1**).

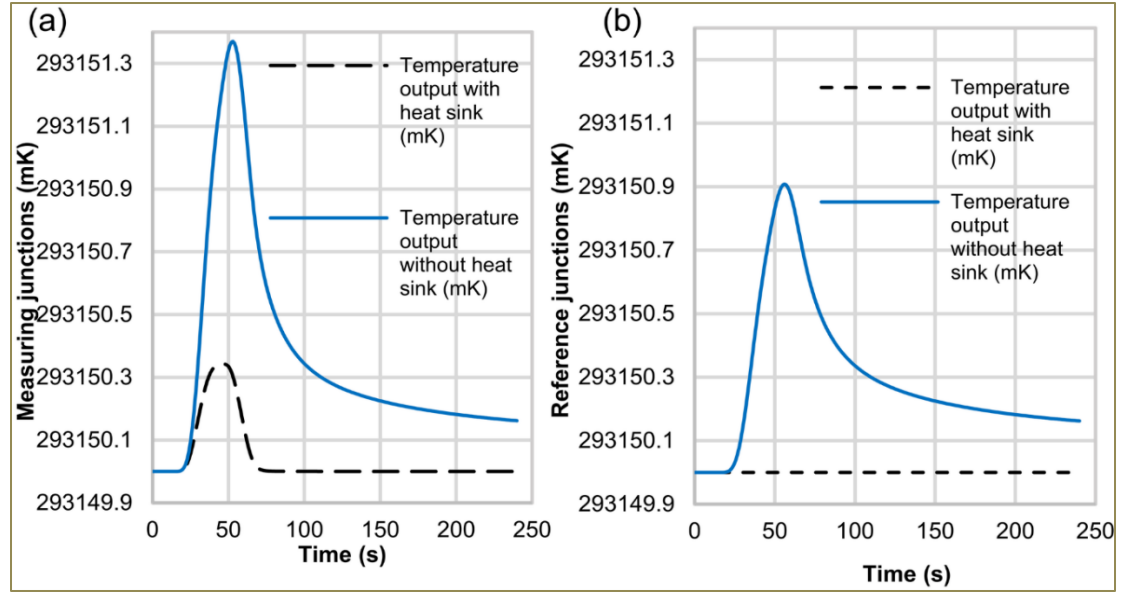


**Figure 5-6:** Mathematical simulation of the temperature outputs at the (a) reference junctions and (b) measuring junctions of the thermopile in the presence and absence of aluminum heat sink. Channel height  $100\mu\text{m}$ , upper and lower channel wall fabricates out of glass.<sup>230</sup>

The design of the microfluidics device minimized the ambient temperature distortions by positioning both junctions of the sensor in a single flow-through channel. These factors ensure controlled symmetry of heat generation and reduce the artifacts of the measured signals in the absence of heat sink.

The thermal conductivity, thermal capacity, and thermal diffusivity of the materials have a significant impact on the magnitude of the thermoelectric signal. Mathematical analysis was performed using five different device configurations where the upper channel wall was fabricated out of PMMA, PDMS, or glass while the lower channel was fabricated out of glass (PDMS-glass; PMMA-glass, glass-glass), PDMS (PDMS-PDMS), or PMMS (PMMA-PMMA). Mathematical analysis indicated that the highest voltage output of  $13.2\mu\text{V}$  is obtained for a device with upper and lower channel walls fabricated out of PDMS and without a heat sink. The glass channel walls

configuration coupled with an aluminum heat sink generates the lowest voltage output of  $1.66\mu\text{V}$  (**Figure 5-7**).

Glass has a higher thermal conductivity and diffusivity ( $0.49\text{mm}^2\text{sec}^{-1}$  <sup>231</sup>) relative to that of PDMS ( $0.11\text{mm}^2\text{sec}^{-1}$  <sup>232</sup>) that leads to the rapid dissipation of the heat in x and y directions. Both PMMA and PDMS materials have higher specific heat capacities that lead to an increase in the temperature difference between the junctions of the sensor. Videos of the heat dissipation for the enzymatic reactions for each material configuration are included in the supplementary information (S4). While PDMS can offer increased sensitivity for calorimetric detection of analytes, the material also has drawbacks that need to be considered for this particular application. It has been reported that PDMS surfaces absorb proteins and small hydrophobic molecules <sup>233</sup> and the polymer is susceptible to swelling and shrinking with commonly used chemicals <sup>234</sup>. In microfluidic devices with a low aspect ratio (height to width), the elastic deformation of the PDMS microchannel can affect the laminar flow profile and pressure distribution within channel <sup>235</sup>. These particular chemical and mechanical properties were not incorporated into this computational study.



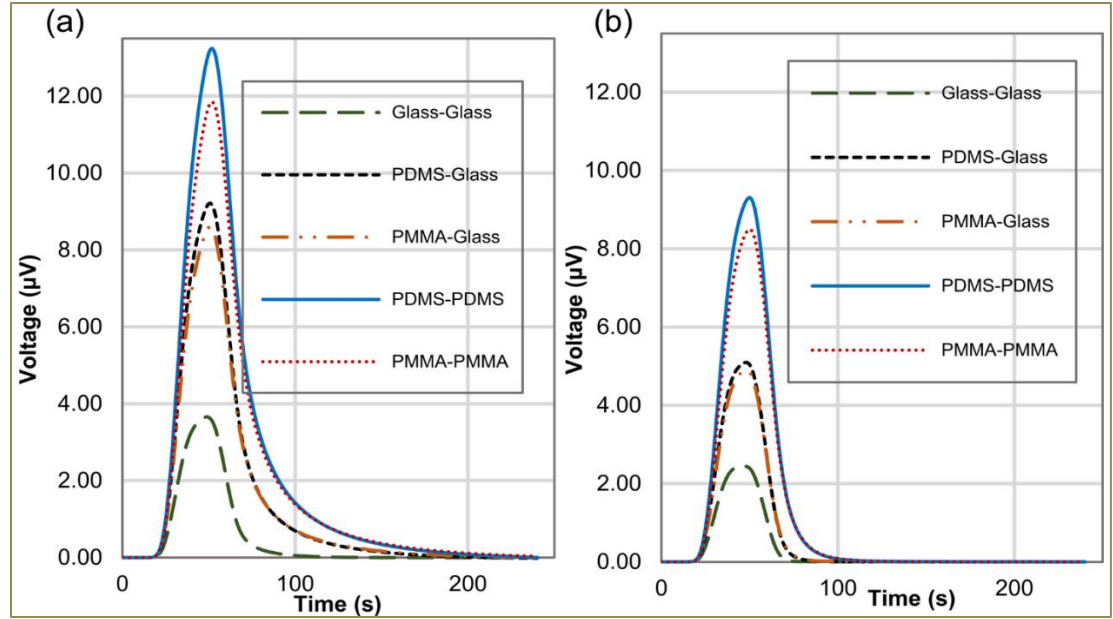


**Figure 5-7:** Numerical simulation of voltage output as a function of material type. The channel height was  $50\mu\text{m}$ . The fluid flow rates for inlet 1 and inlet 2 were  $100\mu\text{L min}^{-1}$  and  $25\mu\text{L min}^{-1}$ , respectively. (a) Thermopile reference junctions at ambient temperature. (b) Thermopile reference junctions in contact with a heat sink.<sup>230</sup>

All of these results are of particular interest to identify the type of material that provides the maximum thermal detection sensitivity. Although glass has a high thermal conductivity the benefits are reduced by the increased rate of lateral heat dissipation from the measuring to the reference junctions of the sensor that reduces the thermal difference between the thermocouple sets. This hypothesis is validated by performing a 2D analysis that neglects the lateral heat dissipation and considers that the reference junctions are maintained at a constant temperature while in contact with a heat sink. The 2D model provides a maximum signal output 30 seconds after glucose is introduced inside the fluidic channel. According to the results obtained, the voltage output decreases by 5.5% for glass-PDMS orientation and 61.4% for PDMS-PDMS after 30 seconds relative to

glass-glass orientation with the same geometry and boundary conditions **Figure 5-8**. This occurs due to the lower thermal conductivity of PDMS compared to glass.

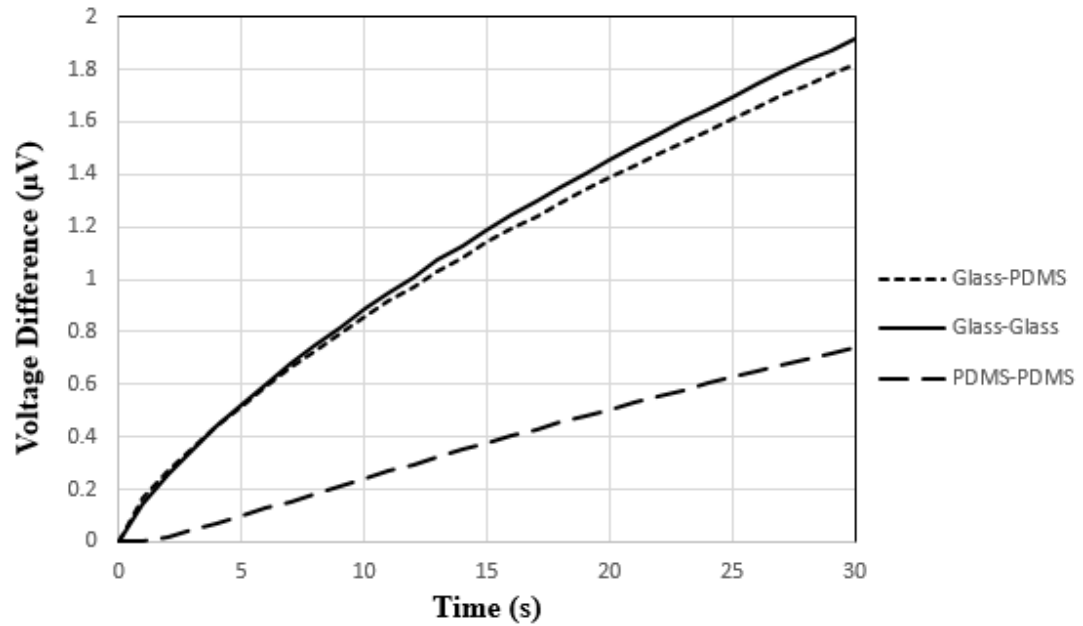


**Figure 5-8:** Effect of substrate material on voltage output obtained using the 2-D model and neglecting the lateral heat dissipation.

However, this 2D model does not account for the thermal diffusivity along the width of the device, which is a crucial factor for the identification of the device materials combination. According to the 3D model, the signal output for a device fabricated out of glass (lower wall) and PDMS (upper wall) is  $5.08\mu\text{V}$  while the signal increases to  $9.27\mu\text{V}$  for a PDMS-PDMS device (with a heat sink present). PDMS is not only a better substrate for the fabrication of the lower channel wall, but it significantly improves the sensitivity of the platform when used as an upper wall material by reducing the rate of heat loss.

## 5.4 Conclusion

The scope of this work has been to identify the critical operational parameters to enhance the sensitivity of the microfluidic thermal sensor. Numerical simulations were performed to investigate the effect of channel height, volumetric flow ratio, and material thermal properties on the temperature distribution and signal output for the platform. The work has relied on both experimental data and numerical analyses that show excellent correlation. The temperature difference detected by the thermopile's junctions depends on the thermal properties of the materials, the presence of a heat sink underneath the reference junctions of the sensor, the flow rate, and the dimensions of the channel. The magnitude of the thermoelectric signal is inversely proportional to the height of the channel and fluid velocity. Using materials with a lower thermal conductivity and eliminating the heat sink can be leveraged to maximize the temperature difference between the thermopile junction sets. This is an exciting hypothesis because theoretically, a material with higher thermal conductivity (glass) should be an ideal substrate compared to a lower thermal conductive material (PDMS) as the application is based on thermoelectric signal measurements. But the 3D model shows that higher lateral thermal diffusivity of glass compared to PDMS acts against the conventional prediction. Experiments are suggested as future works to validate the results obtained using the 3D model to confirm the best combination of materials for the device fabrication predicted by the numerical model.

## CHAPTER 6

# NUMERICAL ANALYSIS OF OPTIMAL DESIGN PARAMETERS FOR A CELL CO-CULTURE MICROFLUIDIC PLATFORM WITH AN INTEGRATED PRESSURE-CONTROLLED VALVE<sup>†</sup>

### 6.1 Background

The development of microfluidic technology for the analysis of cell-to-cell and cell-extracellular matrix interactions is an important topic in biomedical engineering research. While conventional cell co-culture approaches, such as transwell-type co-culture plates, are successfully used for functional analysis of cell-to-cell communications, this technology does not permit a controlled exchange of fluids between two cell culture chambers<sup>55</sup>. Lab-on-a-chip platforms enable a real-time, on-chip analysis of the interaction between cells and their microenvironments. Microfluidics provides flexibility in the device design and better control of the experimental conditions that facilitate drug discovery studies<sup>56</sup>.

Cell co-culture microdevices with an integrated valve enable precise control of the exchange of biochemical factors while minimizing sample variability and enhancing the sensitivity of the analysis<sup>57</sup>. Cell co-culture microfluidic platform has been successfully used for the enhancement of the transfection efficiency of neurons and glia

---

<sup>†</sup> This chapter or portions thereof has been published previously in the **proceedings of the ASME International Mechanical Engineering Congress and Exposition (IMECE)**. Volume 12 (2021). DOI: [10.1115/IMECE2020-23957](https://doi.org/10.1115/IMECE2020-23957). The current version has been formatted for this dissertation.

compared to the conventional petri dish. Polydimethylsiloxane (PDMS) pressure-driven valve fabricated via soft-lithography provided a reversible control and separation of the two cell chambers <sup>236</sup>. A microdevice with a hydraulically controlled PDMS valve was used for the assessment of the interaction between tumor and endothelial cells. On-chip co-culture of multiple cell types of the intestine, liver, and glioblastoma equivalents was used for the analysis of drug absorbance and toxicity <sup>237</sup>.

Although multiple studies are reporting the design and fabrication of microfluidic cell co-culture platforms, very few research groups developed numerical models to investigate the impact of physical parameters (e.g., valve thickness, material elasticity, pressure) on the optimal design of the device. A three-dimensional numerical flow model of cell co-culture was developed to analyze the species concentration within the microchannel. The study indicates that the distribution is a function of channel length and inlet concentration <sup>238</sup>. Numerical analyses were performed to determine the displacement of the micropillars in a cell co-culture platform. The mathematical simulations indicated that the gap, size, velocity, and height of the micropillar modules had a substantial impact on the stability of the arrays <sup>239</sup>.

The rapid development of 3D printing and rapid-prototyping microfabrication techniques enables the fabrication of lab-on-a-chip platforms for cell co-culture. These devices can provide precise control of fluid dynamics and environmental factors. In this paper, we report the fabrication and optimization of critical design parameters of a microfluidic device with an integrated PDMS hydraulic valve that reversibly separates two cell culture chambers. A two-dimensional numerical analysis of factors that affect the deflection of a valve was performed, and the optimal combination of optimized

parameters for effective isolation of two chambers is presented. The parameters under investigation include water height, membrane thickness, and the elasticity of the PDMS.

The proposed microfluidics platform is innovative because it could enable the controlled exchange of released cell signaling molecules between two cell lines as well as the integration of a microprobe-based method for the purification of mRNA<sup>240</sup>. The proposed microfluidics platform offers a promising new tool for the assessment and characterization of the complex interaction of different cell types.

## 6.2 Materials and methodology

### 6.2.1 Device design

The platform under study consists of two 27.5 mm × 35 mm × 10 mm cell culture chambers separated by a PDMS-fabricated hydraulic valve (10 mm × 35 mm × 9.5 mm). The actuation of the valve is controlled using hydraulic pressure exerted by the chamber positioned directly above the valve. The deflection of the valve barrier provides separation of the cell chambers and the individual microenvironments. Upon the release of the pressure, the valve returns to its original position and allows the exchange of signaling molecules between the cells (**Figure 6-1**).

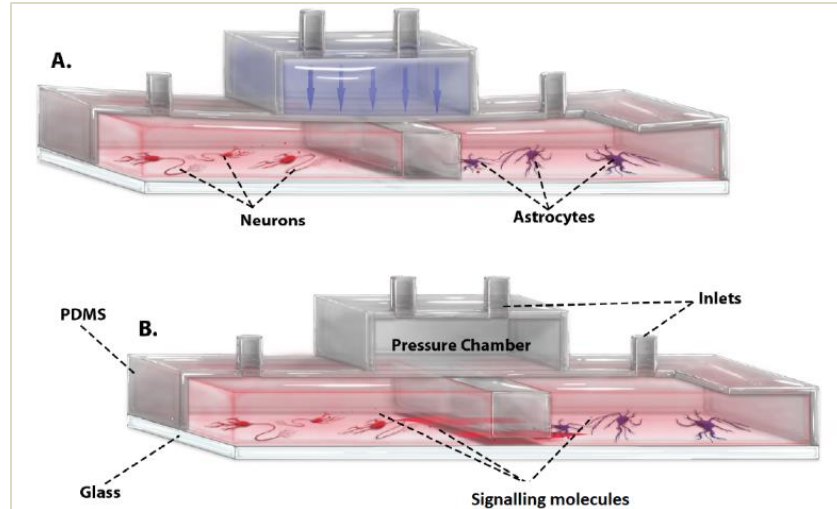


**Figure 6-1:** Design of microfluidics cell co-culture platform. Pressure controlled valve separates the cell chambers (A). Upon release of the pressure, the valve moved to a vertical position and allows the exchange of signaling molecules between the cell lines.<sup>241</sup>

#### 6.2.2 Numerical modeling

The impact of several factors on the vertical displacement of the valve was mathematically simulated using COMSOL Multiphysics 5.4. The software implemented the Mooney-Rivlin method, a widely used hyper-elastic material model due to the choice of fabricating a PDMS-based valve<sup>242</sup>. A schematic of the device, including the dimensions of the pressure-controlled valve is shown in **Figure 6-2**. The two-dimensional numerical model was developed in XZ-plane. The width of the device (along XY-plane) is not considered since the analysis is focused on the displacement of the valve in a vertical direction. The bottom channel wall is a glass slide (75 mm × 35 mm × 18 mm), while the pressure chamber and the hydraulic valve are filled with water to actuate its displacement.

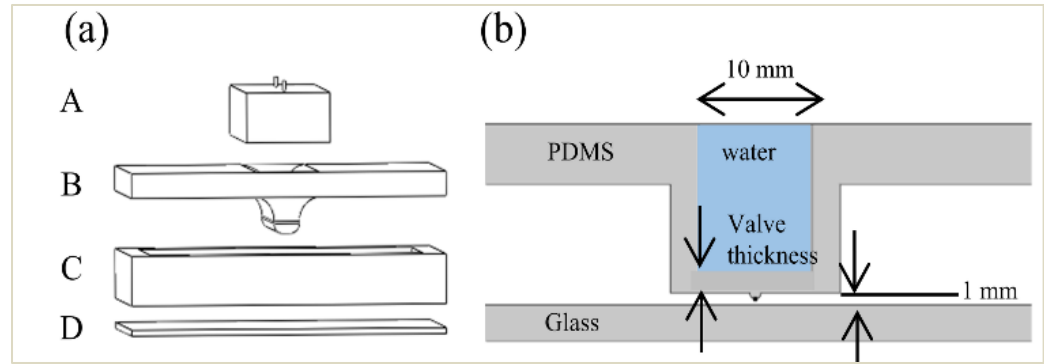


**Figure 6-2:** (a) Schematic of the components of the cell co-culture device. (A) hydraulic pressure chamber, (B) PDMS valve, (C) channel wall, and (D) glass; (b) Schematic and dimensions of hydraulic valve.<sup>241</sup>

The height of the hydraulic pressure chamber provides the force that bends the PDMS and displaces the valve in the vertical direction to close the barrier between the cell chambers. The distance between the valve and the lower channel wall is 1 mm, while the distance between the maximum elevation of the valve and the glass slide is 0.5 mm. The width of the valve and the pressure chamber is 10 mm is considered as an open boundary for the simulations.

The Fluid-Structure Interaction (FSI) multiphysics interface combines fluid flow with solid mechanics to capture the interaction between the fluid and the solid structure. A solid mechanics interface and a single-phase flow interface model the solid and the fluid, respectively. The FSI module combines the pressure exerted by water inside the pressure chamber using the laminar flow interface with the displacement of the valve due to the hydrostatic pressure using the solid mechanics interface. The FSI couplings appear on the boundaries between the fluid and the solid. The deflection of the valve due to the hydraulic pressure is modeled using the arbitrary Lagrangian-Eulerian method (ALE). As for loading, the outer surfaces of the device were fixed. The internal surfaces were free to deform due to the hydrostatic pressure present. However, only the flexible membrane was



thin enough to demonstrate noticeable deflections. The vertical walls of the chamber holding the water that would cause the valve to close experienced some deflections, but it was significantly less than the deflection observed by the membrane.

The working fluid is assumed to be incompressible. Therefore, the Navier-Stokes equation and the continuity equation are solved. Navier-Stokes equation using arbitrary Lagrangian-Eulerian formulation for an incompressible fluid is defined by:

$$\rho_f \frac{\partial u_f}{\partial t} + (\rho_f \cdot \nabla u_f \cdot u_c) + \nabla P - (2\mu \nabla \varepsilon) = \rho_f F_f^b \quad (\text{Eq. 4-1})$$

$$\nabla \cdot u_f = 0 \quad (\text{Eq. 4-2})$$

The model considers a low viscosity fluid ( $\mu = 0$ ) in the pressure chamber, and the walls of the device are considered to be in no-slip condition. The impact of gravitational force on the displacement of the valve is considered as well. The actuation of the valve caused by hydraulic pressure is governed by the following equation:

$$\rho_s \frac{\partial^2 L}{\partial t^2} - \nabla \cdot [F_s \cdot S_s] = \rho_s F_s^b \quad (\text{Eq. 4-3})$$

Both the working fluid and membrane of the valve are fully coupled at the interface of interaction,  $\Gamma$ , to consider for both dynamic and kinematic continuity, which is a prime coupling condition. Therefore, the coupling equations for kinematic continuity is defined as:

$$L_\Gamma(t) = x_\Gamma^f(t) \quad (\text{Eq. 4-4})$$

$$\dot{L}_\Gamma(t) = u_{f_\Gamma}(t) \quad (\text{Eq. 4-5})$$

$$\ddot{L}_\Gamma(t) = \dot{u}_{f_\Gamma}(t) \quad (\text{Eq. 4-6})$$

Similarly, the dynamic coupling equations are expressed as:

$$T_f(t) + T_s(t) = 0 \quad (\text{Eq. 4-7})$$

where  $T$  is the traction vector, that is defined as the product of the normalized vector and stress tensor as follows:

$$T = \sigma \cdot n \quad (\text{Eq. 4-8})$$

To calculate the required fluid pressure needed for the valve as a function of various PDMS elasticity and valve thicknesses, trendlines were added using three different models as follows to find the best-fit equation to show the relationship between water pressure, membrane thickness, and material elasticity (in the form of the mixing ratio) to have a properly functioning valve:

$$\text{Power model: } y = bx^m \quad (\text{Eq. 4-9})$$

$$\text{Exponential model: } y = bm^x \quad (\text{Eq. 4-10})$$

$$\text{Linear model: } y = mx + b \quad (\text{Eq. 4-11})$$

### 6.2.3 Fabrication of cell co-culture microfluidic device

#### 6.2.3.1 Device fabrication using replica molding

The cell co-culture device is fabricated using a replica molding technique from the 3D printed carbon nanofiber molds and PDMS. Carbon nanofiber is given preference over ABS, PLA, and nylon because of its low shrinkage factor that minimizes variability in dimensions of the device components<sup>243</sup>. Three separate negative molds formed the cell culture container, valve, and pressure chamber. After 3D printing (Crealty3D Ender-3 pro-High Precision 3D Printer), the surfaces are smoothened using sandpaper and acetone. PDMS (Sylgard 184, Dow Corning, MI) is poured over the molds, treated in a basic plasma cleaner (Harrick Plasma) for 10 minutes, and stored in a desiccator for 30

minutes to eliminate bubble formation. The PDMS is allowed to solidify for 24 hours at room temperature. **Figure 6-3** shows an image of the fabricated device. Smoothing the 3D printed mold surfaces is a critical step to ensure the effective detachment of the PDMS substrates. The components of the device are assembled in a direction from the bottom to the top of the device using oxygen plasma treatment of the glass and PDMS. The parts are treated for 3 minutes at low pressure (200 millitorrs) in the plasma chamber. Using higher pressure leads to the deformation of the PDMS and reducing its capabilities to bond to the other components of the device.

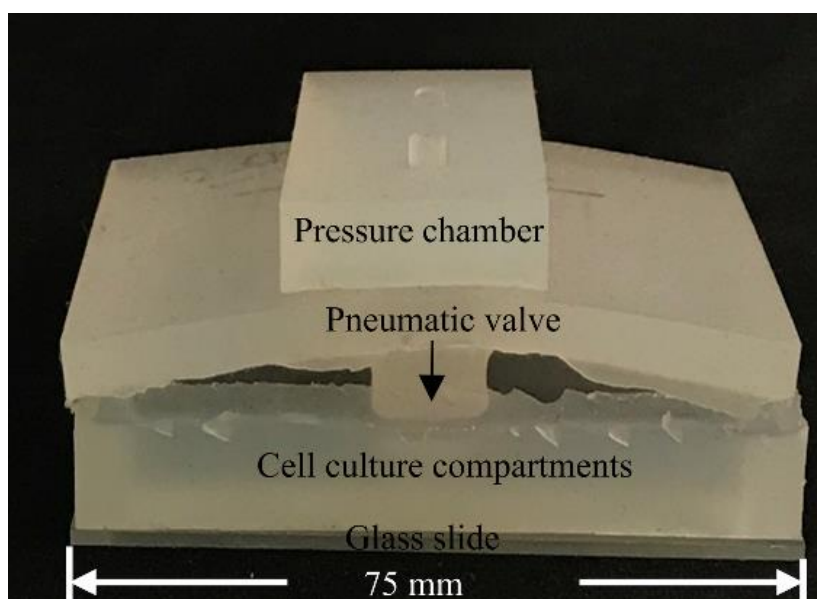


**Figure 6-3:** PDMS microfluidic cell co-culture device fabricated using replica molding.<sup>241</sup>

#### 6.2.3.2 Device fabrication using photolithography

The cell co-culture device fabricated using the photolithography technique consists of two PDMS layers. The bottom layer includes the cell chambers, microfluidic channel, inlets, and outlets, whereas the top PDMS layers involve a hydraulic pressure chamber for regulating the valve movement to separate the two chambers. The mold for

the first PDMS layer was fabricated using a negative photoresist (Hare SQ-5 and Hare SQ-50) patterned by two transparent masks after positioning over a 4" silicon wafer (Wafer World, FL). The masks were printed using a high-resolution printer from Photomask portal, TX. The first transparent mask generated microchannels with dimensions of  $100\text{ }\mu\text{m} \times 100\text{ }\mu\text{m} \times 5\text{ }\mu\text{m}$  (length, width, and height). The second transparent mask generated two cell culture chambers, wells for media reservoirs and waste, and defined the connecting channels that allowed for media exchange between the chambers (**Figure 6-4 (A)**). The dimensions of the cell chambers were  $6\text{ mm} \times 800\text{ }\mu\text{m} \times 100\text{ }\mu\text{m}$  (length, width, and height). A barrier was created between the cell chambers by inserting a strip of PDMS  $100\text{ }\mu\text{m}$  wide having multiple connecting channels at the bottom that could be opened or closed. The mold for the second PDMS layer was made by attaching a slab of glass with dimensions of  $4\text{ mm} \times 12\text{ mm} \times 1\text{ mm}$  (width, length, and height) to a silicon wafer. A pre-polymer of PDMS was then mixed with a curing agent at a 12:1 ratio and poured over the mold (**Figure 6-4(B) and (C)**). After degassing, the PDMS layers were allowed to solidify over their molds at  $70^{\circ}\text{C}$  for 2 h.

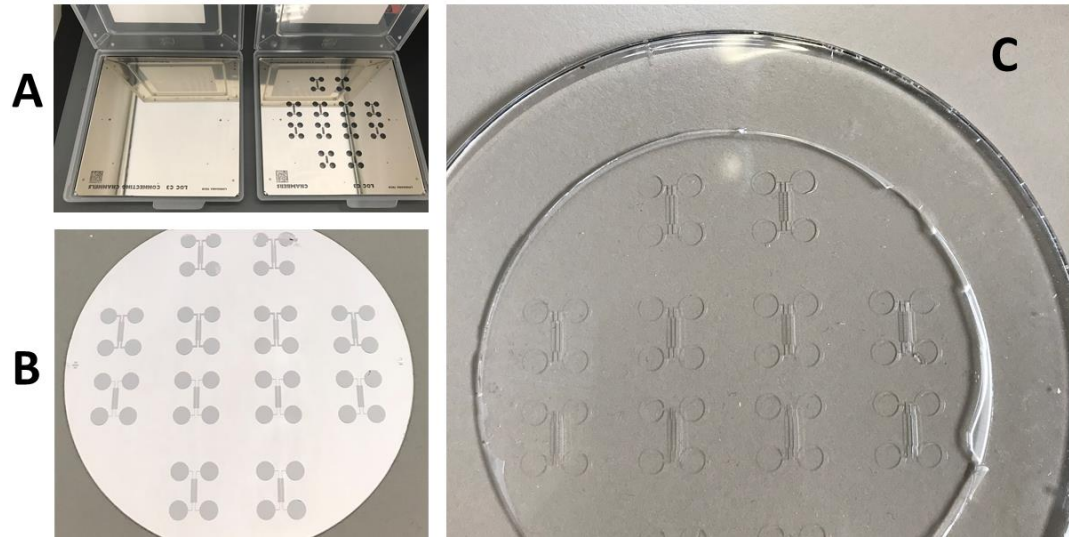


**Figure 6-4:** Cell-co culture device fabricated by a photolithography technique using PDMS. (A) Design of the chrome-plated photomask, (B) Pattern transferred to silicon wafer after completion of the photolithography process, (C) Solidified PDMS fabricated chips.

#### 6.2.3.3 Device fabrication using stereolithography

The design of the cell culture device for the stereolithography method was obtained using SolidWorks. The device consists of two parts: the bottom channel wall that contains the cell culture chambers ( $1.3\text{-inch} \times 0.40\text{ inch} \times 600\text{ }\mu\text{m}$  each for length, width, and height, respectively) and the inlets ( $0.40\text{-inch}$  diameter) and the top channel wall that covers the bottom channel surface.

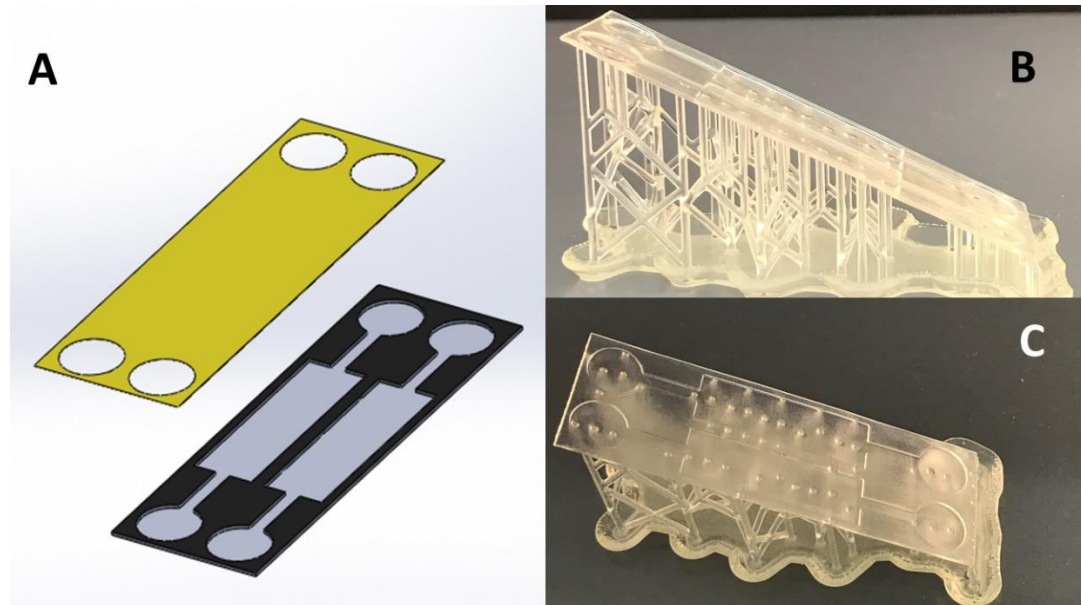


**Figure 6-5:** Microfluidic cell co-culture device fabricated using stereolithography method: (A) SolidWorks design for the top (yellow) and bottom (black) channel walls, (B) & (C) Images of the fabricated lower channel wall of the device with integrated supports to prevent bending.

Stereolithography 3D printing device (FormLabs) and clear resin bought from the same vendor were used to fabricate the device. To avoid any bending of the device due to its thin structure, full raft supports with a touchpoint of 0.50 mm were used. After the printing was done, the device was thoroughly washed in isopropyl alcohol (IPA) and dried at room temperature before placing it into the curing station. It is very important to dry all portions of the device before curing as the wet parts would not be evenly cured as the dry parts could leave the device sticky. After drying the IPA at room temperature, the device was placed inside the curing station (FormLabs) for 45 minutes at 60°C to solidify the resin (**Figure 6-5**).

### 6.3 Results and discussions

#### 6.3.1 Valve displacement as a function of fluid pressure inside the pressure chamber

The vertical displacement of the hydraulically controlled microfluidic valve is modeled using COMSOL Multiphysics 5.4. The physics-controlled extremely fine mesh was chosen for the device under study. COMSOL uses physics (structural mechanics of materials) to optimize the mesh size. Specifically, the mesh was finer in areas that are prone to stress concentrations (e.g., the attachment points of the membrane to the rest of the device). The model uses the value of the stiffness factor of PDMS (also known as the Young's Modulus) and the density of the valve material from two previously published articles that depend on the various crosslinking ratio of the PDMS base and the curing agent <sup>244,245</sup>. Initially, a standard 10:1 crosslinker ratio is employed to analyze the impact of fluid pressure (15 mm-H<sub>2</sub>O, 20 mm-H<sub>2</sub>O, 25 mm-H<sub>2</sub>O, 30 mm-H<sub>2</sub>O, 35 mm-H<sub>2</sub>O, 40 mm-H<sub>2</sub>O, and 45 mm-H<sub>2</sub>O) and valve thicknesses (0.1 mm to 1 mm) on the valve displacement. The model shows that the displacement of the valve is directly proportional to the fluid pressure and inversely proportional to the valve thickness (**Figure 6-6**). Numerical simulations show that valve thickness of 0.1 mm provides the maximum deflection while 1 mm accounts for the lowest. Results indicate a change in vertical displacement from 0.025 mm to 0.886 mm for valve thicknesses of 1 mm and 0.1 mm, respectively, using a 15 mm constant fluid pressure (15 mm-H<sub>2</sub>O).

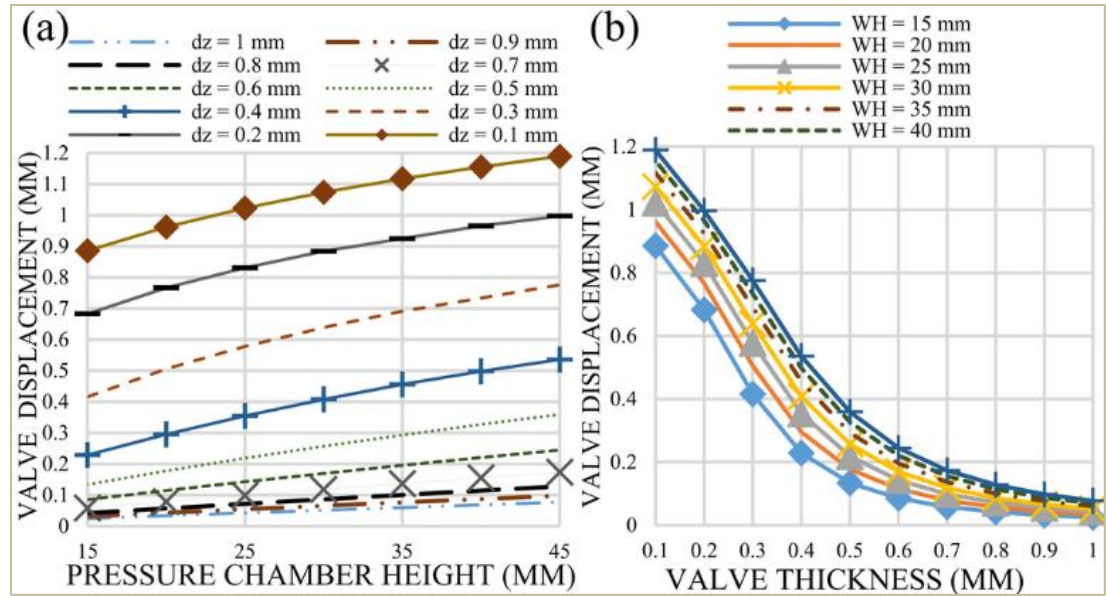


**Figure 6-6:** Valve displacement in the vertical direction as a function of (a) pressure exerted by the fluid inside the pressure chamber, and (b) thickness of the valve. Simulations were performed for the 10:1 elastomer base to crosslinker ratio.<sup>241</sup>

The dimensions of the pressure chamber have a significant impact on the deflection of the valve. Increasing the height of the hydraulic chamber from 15 mm to 45 mm exerts more force on the valve due to additional fluid pressure (mm-H<sub>2</sub>O) which increases the deflection of the 1 mm thick valve by 208%. This impact is 168% and 34% for valve thicknesses of 0.5 mm and 0.1 mm, respectively. This is a very important factor for the efficient design of the cell co-culture device as it ensures permanent isolation of the cell chambers. While thick PDMS valves require a significant amount of initial hydraulic pressure to actuate, thin valves require lower fluid pressure to actuate the valve displacement. For the same hydraulic pressure, the thick valves account for lower displacements compared to the thinner valves (**Figure 6-6b**).



### 6.3.2 Valve displacement as a function of valve thickness and PDMS elasticity

Mathematical simulations indicate that the vertical displacement increases by 0.25 mm when the valve thickness is changed from 1 mm to 0.1 mm for 45 mm-H<sub>2</sub>O fluid pressure. The change in valve deflection is 0.16 mm when the fluid pressure inside the hydraulic pressure chamber decrease to 30 mm-H<sub>2</sub>O. PDMS with different crosslinking ratios was modeled to determine its effect on the displacement of the valve (**Figure 6-7**).

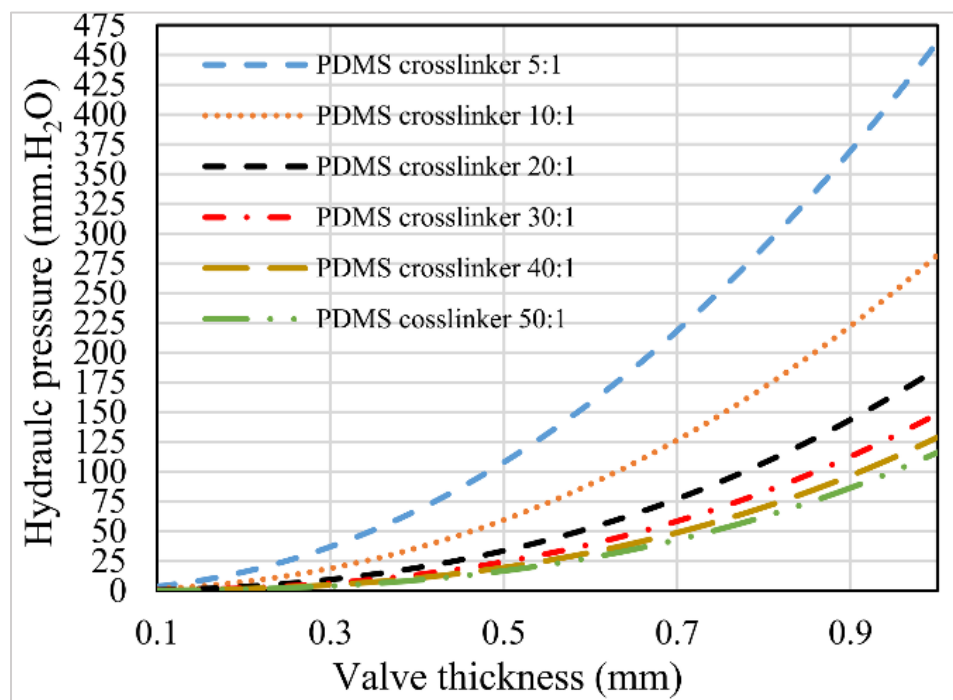


**Figure 6-7:** Pressure (mm-H<sub>2</sub>O) required for 0.5mm valve deflection as a function of valve thicknesses and PDMS elasticity.<sup>241</sup>

### 6.3.3 Valve deflection as a function of various PDMS base and curing agent crosslinking ratio

**Figure 6-8** represents the deflection profiles of various elastomer base and crosslinking ratios (10:1, 20:1, 40:1, and 50:1) that correspond to the moduli of elasticity

of 2060.6 kPa, 1163.75 kPa, 715.33 kPa, and 625.64 kPa, respectively<sup>244</sup>. The analysis was performed using a 0.5 mm thick valve and 30 mm-H<sub>2</sub>O.

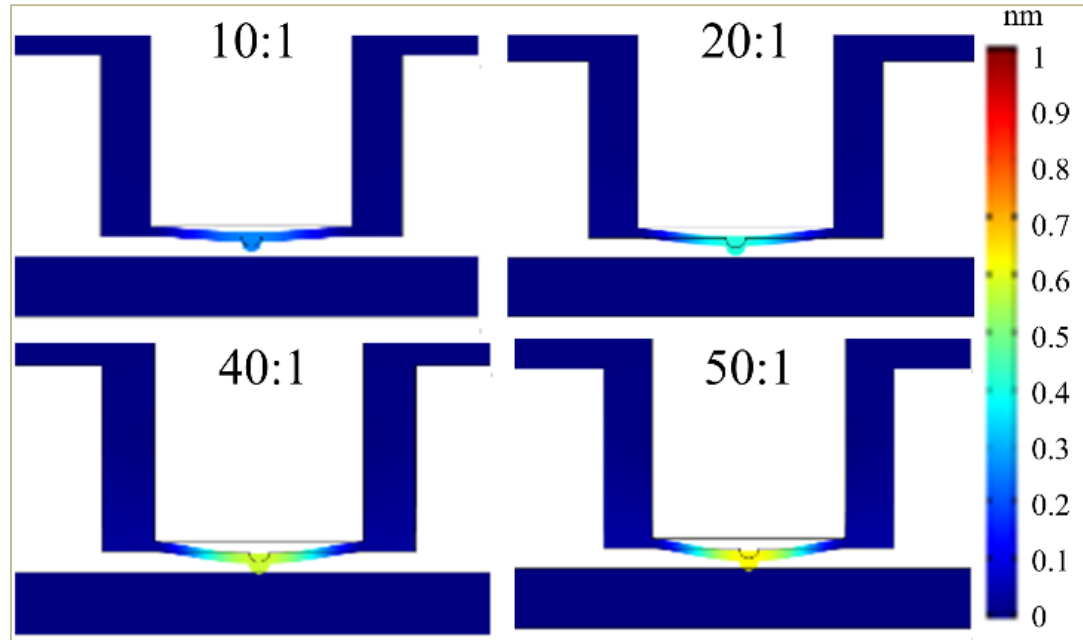


**Figure 6-8:** Simulation of the effect of PDMS elasticity in valve deflections. Analyses were performed for a device that has a 30 mm pressure chamber height, 0.5 mm thick valve, and 10:1, 20:1, 40:1, and 50:1 crosslinking ratio of PDMS base and curing agent.<sup>241</sup>

Mathematical simulations show that the deflection of the valve increases by 58% for a change in PDMS crosslinking ratio from 10:1 to 20:1. Moreover, the increase becomes 143% when the elasticity is increased to 50:1. Polymer with standard elasticity (10:1) is normally used for the fabrication of PDMS microfluidic devices. Optimal deflection of the valve by minimizing the required pressure can be obtained by improving the elasticity of the valve using higher concentrations of the PDMS. The distance between the hydraulic valve and the lower channel wall of the device is 0.5 mm. Therefore, the optimal design parameters ensure that the valve deflects 0.5 mm in a

vertical position. The pressure required to cause a 0.5 mm deflection of the valve for varying valve thicknesses and elasticity is presented in **Table 6-1**.

**Table 6-1:** Fluid pressure (mm-H<sub>2</sub>O) required to deflect the valve 0.5 mm for various thicknesses and PDMS base to curing agent crosslinking ratio.

Valve thickness (mm)	Pressure chamber height (mm)					
	PDMS 5:1	PDMS 10:1	PDMS 20:1	PDMS 30:1	PDMS 40:1	PDMS 50:1
0.1	4.07	1.75	0.73	0.44	0.32	0.25
0.2	13.89	5.85	2.26	1.29	0.88	0.67
0.3	36.82	19.95	9.68	6.12	4.41	3.44
0.4	66.94	39.88	23.43	16.92	13.38	11.19
0.5	107.9	63.91	39.51	30.28	25.27	22.07
0.6	160.72	94.17	58.32	45.29	38.45	34.14
0.7	221.4	128.44	79.57	62.02	53.04	47.29
0.8	291.16	170.48	105.33	81.38	69.44	61.92
0.9	382.38	212.31	134.21	103.17	87.44	78.20
1	453.6	264.88	164.51	125.79	107.28	95.49

Prior publications have shown that PDMS permeability depends on its thickness<sup>246</sup>. However, for our application, this factor was irrelevant and was not considered a critical parameter. During the actual experimental studies, the device will be set up in the cell culture chamber at 37°C, with 5% CO<sub>2</sub> that will diffuse freely into the chambers through the cell culture wells.

#### 6.3.4 Statistical analysis

Statistical testing is performed to develop an equation to predict the necessary pressure to deflect the membrane 0.5 mm for various membrane thicknesses and PDMS base-crosslinker ratios. From the analysis, the equation in the form of a product of exponential functions was created:

$$y = b (m_1)^{x_1} (m_2)^{x_2} \quad \text{(Eq. 4-12)}$$

where  $y$  represents the pressure needed (in mm-H<sub>2</sub>O),  $x_1$  represents the thickness of the membrane (in mm), and  $x_2$  represents the PDMS base-crosslinker ratio (in the form of x:1). The analysis to determine the best-fit curve for the data collected yields the following constant values:  $b = 3.326$ ,  $m_1 = 302.3$ , and  $m_2 = 0.9603$ . The standard error for the three constants  $b$ ,  $m_1$ , and  $m_2$  are 0.2316, 0.2984, and 0.005384, respectively. Comparing t-observed values for each of the three constants to the critical value (2.002) shows that all three constants are needed in approximating the necessary pressure to close the valve. The coefficient of determination for the equation developed is 0.8812. To determine the best-fit equation, linear and power models were also implemented. It was determined that the exponential equation had the highest correlation of determination (0.881) compared to the linear (0.697) and the power (0.747) equations. Therefore, the choice of the exponential model is justified.

A surface plot with the values of the design parameters is presented in **Figure 6-9**. The dimensions of the microfluidic device are within the limits of the replica molding technique, and the valve design requires that it is deflected under minimal pressure. Therefore, the optimal design parameters will ensure minimal pressure chamber height and maximum valve thickness that provide the most efficient displacement.

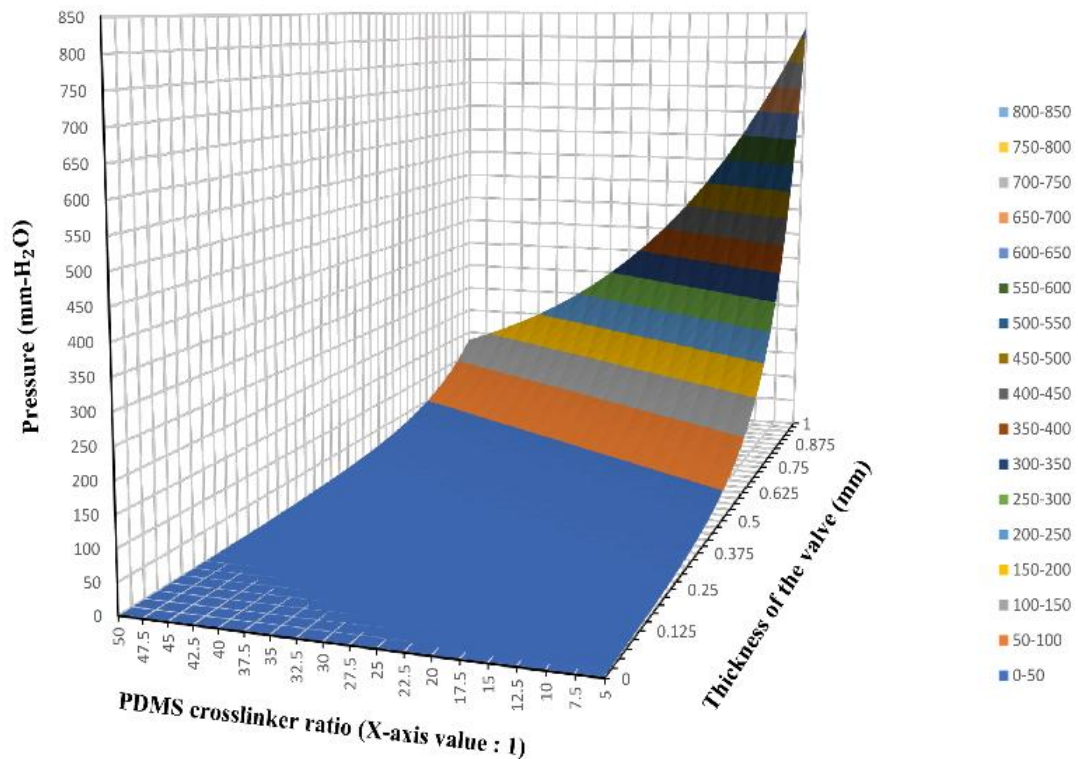


**Figure 6-9:** Surface plot of the values of the fluid pressure (mm-H<sub>2</sub>O), valve thickness, and PDMS elasticity ratio that ensures 0.5 mm displacement of the valve.<sup>241</sup>

## 6.4 Conclusion

This study presents the design and fabrication of a microfluidic cell co-culture device with a hydraulically controlled PDMS valve for the reversible isolation of two distinct cell-culture chambers. A two-dimensional numerical model identifies the optimal design parameters, including valve thickness and pressure exerted by the fluid inside the

hydraulic pressure chamber that enables valve actuation. The reported device has a new design and is easy to fabricate. Future work will focus on the implementation of this device in cell co-culture study.

## **CHAPTER 7**

### **CONCLUSIONS AND RECOMMENDATIONS**

Findings from each study are described at the end of the corresponding chapter. The overall conclusions and suggestions for future work are presented in this chapter.

#### **7.1 Conclusions**

Chapter 2 provides an overview of the existing exosome isolation and detection methods, their efficiencies and drawbacks, the importance of microfluidics for exosome study, and finally a detailed summary of the most recent microfluidic platforms for the separation and detection of exosomes from various biofluids. Although much progress has been achieved in recent years with on-chip exosome isolation and detection, there is still room for improvements to utilize these techniques in clinical and research settings.

Exosomes encapsulate genomic and proteomic biomarkers for non-invasive diagnosis and disease monitoring. However, exosome surface-markers heterogeneity is a major drawback of current isolation methods. In chapter 3, the approach for the functionalization of the ExoPRIME tool (300 $\mu$ m $\times$ 30mm) with the polyelectrolytes, biotin, streptavidin, and anti-CD63 antibodies has been presented. FESEM and EDX analyses were performed to confirm the layer-by-layer assembly of the polyelectrolytes on the microprobe surfaces. Additionally, confirmation of the anti-CD63 immobilization

was obtained using fluorescence imaging by immobilizing the streptavidin-coated microneedles in the biotinylated FITC solution.

The lab-on-a-chip thermoelectric immunosensor presented in chapter 4 was able to quantify the inflammatory cytokine, TNF- $\alpha$ , with picomolar sensitivity. The feasibility of the technology was demonstrated via accurate measurement of the concentration of TNF- $\alpha$  in astrocytes cell culture media. The immunoassay was performed in a microfluidic device with an integrated antimony-bismuth thermopile sensor and had a limit of detection of 14 pg mL<sup>-1</sup>. The device was fabricated using the rapid prototyping xurography technique and consisted of two inlets and a single outlet. The anti-TNF- $\alpha$  monoclonal antibody was used to capture the analyte while the detection was performed using glucose oxidase-conjugated secondary antibody. A standard calibration curve was created using serial dilutions of synthetic TNF- $\alpha$  (0 –2000 pg mL<sup>-1</sup>) by plotting the area under the curve of the signal versus the concentration of the analyte. The efficacy of the device was evaluated by quantifying TNF- $\alpha$  in the cell culture medium of lipopolysaccharide-stimulated and non-stimulated astrocytes. The results demonstrated the excellent accuracy of the calorimetric immunoassay when compared with a standard commercial ELISA microplate reader. The immunosensor offers high reproducibility and versatility in the choice of the detection enzyme.

Chapter 5 reports a three-dimensional numerical analysis of the critical design parameters of a continuous-flow biosensor with an integrated thermopile to significantly increase the detection sensitivity of the platform. The work discusses the impact of volumetric flow rate, channel height, material thermal properties, and heat sink on the magnitude of the thermoelectric signal. Since this experimental configuration has been



implemented in a variety of biochemical analyses, particular emphasis in this work is maximizing the detection sensitivity of the device. Computational thermal modeling was performed to investigate the impact of channel height (50  $\mu\text{m}$ , 100  $\mu\text{m}$ , 150  $\mu\text{m}$ , and 200  $\mu\text{m}$ ), the volumetric flow rate of the substrate (25  $\mu\text{L min}^{-1}$  and 50  $\mu\text{L min}^{-1}$ ), and the microdevice material (glass, PMMA, and PDMS) on the output of the thermoelectric sensor. Experimental data validated the model and provided an excellent correlation between the predicted and measured voltage output. Results show that fabricating the calorimeter out of materials with lower thermal diffusivity, reducing the channel height, and eliminating the heat sink at the reference junction of the thermopile increases the sensitivity of the platform by 783%.

The design, fabrication, and a two-dimensional numerical analysis to identify the optimal operating parameters of a novel microfluidic co-culture platform with an integrated pressure-controlled valve are presented in chapter 6. Photolithography, stereolithography, and replica molding using 3D printed PDMS molds were used for the fabrication of three different cell co-culture devices. Altering the position of the PDMS hydraulic valve permits individual manipulation of the cellular microenvironment of the two adjacent cell culture chambers. The mathematical model analyzes the deflection profile of the valve in the vertical direction as a function of several parameters: valve thicknesses, the pressure exerted by the fluid inside the pressure chamber, and PDMS elasticity determined by the ratio of the elastomer base and the curing reagent. The valve under study requires a deflection of 0.5 mm to completely isolate the two cell chambers. The combination of the optimal design parameters is identified using numerical analysis. Mathematical simulations show that the deflection of the membrane is inversely

proportional to the valve membrane thickness and directly proportional to the pressure exerted by the fluid on the valve.

## **7.2 Future Work**

Fabrication of lab-on-a-chip calorimetric immunosensors using PDMS as both the upper and lower channel walls could increase the LOD of the thermoelectric platform as indicated by the numerical analysis. Therefore, future work should focus on the fabrication and implementation of PDMS-PDMS (upper and lower walls respectively) microfluidic calorimetric immunoassay and compare the results with the presented numerical model in this dissertation.

While this work was focused on the design and fabrication of a microfluidics cell co-culture platform, future work should focus on the integration of two cell lines within the device. The effective manipulation of the microenvironments will provide insights into cellular behavior, as well as the change that occurs at the genomic and transcriptomic levels.

## APPENDIX

**Figure A 1:** Temperature distribution profile at the outer surface of the lower channel wall 0, 60, and 240 seconds after the introduction of the substrate. The channel height is  $50\mu\text{m}$  and the upper and lower channel walls are fabricated from glass. (i) Reference junctions not in contact with a heat sink; (ii) reference junctions in contact with the aluminum heat sink.

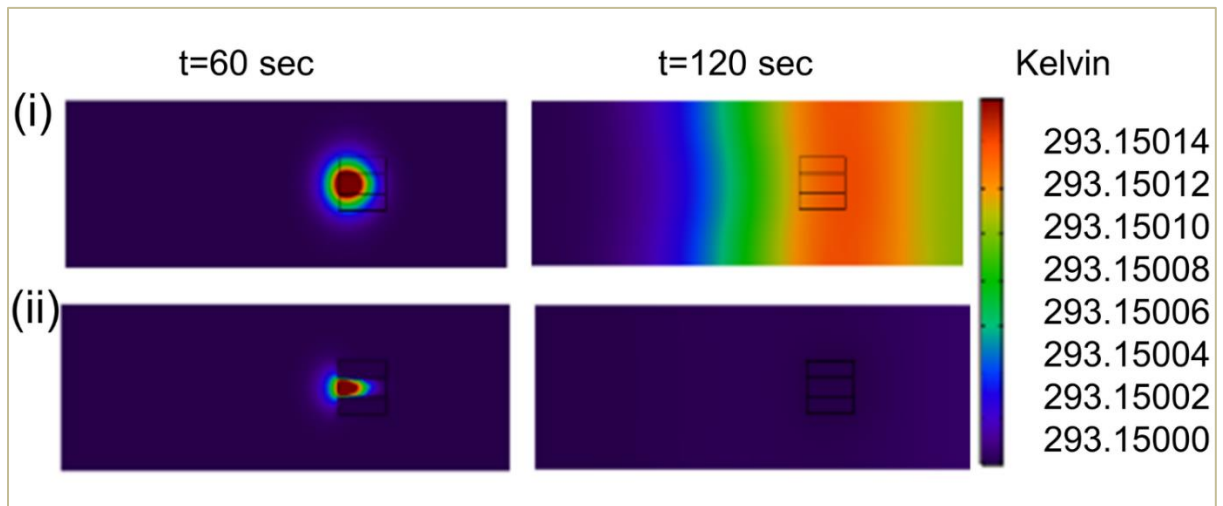


**Table A 1:** Area under the curve ( $\mu\text{V}\cdot\text{s}$ ) of thermoelectric response ( $0\text{--}2000\text{ pg mL}^{-1}$  TNF- $\alpha$ ) that were used to create the standard calibration curve.

	$0\text{ pg mL}^{-1}$	$125\text{ pg mL}^{-1}$	$250\text{ pg mL}^{-1}$	$1000\text{ pg mL}^{-1}$	$2000\text{ pg mL}^{-1}$
Injection 1	0.41	8.54	10.64	35.7	66.7
Injection 2	0.15	8.69	10.20	35.8	62.3
Injection 3	0.45	7.06	10.58	38.4	67.9
Injection 4	0.34	6.97	10.67	36.2	59.7
<b>Average AUC</b>	<b>0.34</b>	<b>7.81</b>	<b>10.47</b>	<b>35.52</b>	<b>64.15</b>
Standard error	0.07	0.46	0.10	0.63	1.91

**Table A 2:** Inter and intra-calorimetric assay variation for devices with 250 pg mL<sup>-1</sup> TNF- $\alpha$ .

# of injections	Area Under the Curve (AUC)		
	Device 1	Device 2	Device 3
Injection 1	10.64	10.41	10.33
Injection 2	10.58	10.39	10.38
Injection 3	10.49	10.44	10.42
Average AUC ( $\mu$ V-s)	10.57	10.41	10.38
Standard deviation	0.08	0.03	0.05
<b>% Coefficient of variation</b>	<b>0.72 %</b>	<b>0.24 %</b>	<b>0.47 %</b>
Inter-assay Average AUC ( $\mu$ V-s)	10.45		
Inter-assay standard deviation	0.10		
<b>Inter-assay % coefficient of variation</b>	<b>0.99 %</b>		

**Table A 3:** Global parameters defined for the mathematical model

Parameters	Values
$D_g \equiv$ Diffusion coefficient of glucose	$6.7 \times 10^{-10} \text{ m}^2 \text{ s}^{-1}$ <sup>210</sup>
$c_i \equiv$ Glucose concentration	$55 \text{ mol m}^{-3}$
$c_{Gox} \equiv$ Glucose oxidase concentration	$6.9892 \times 10^{-4} \text{ mol m}^{-3}$
$u_w \equiv$ Inlet 1 velocity	$0.000674 \text{ m s}^{-1}$
$u_g \equiv$ Inlet 2 velocity	$0.000168 \text{ m s}^{-1}$ and $0.000084 \text{ m s}^{-1}$
$t_u \equiv$ Upper channel wall thickness	1 mm
$t_b \equiv$ Lower channel wall thickness	170 $\mu\text{m}$
$L_c \equiv$ Channel length	65 mm
$W_c \equiv$ Channel width	12 mm
$t_c \equiv$ Channel height	25 $\mu\text{m}$ , 50 $\mu\text{m}$ , 100 $\mu\text{m}$ , 200 $\mu\text{m}$
$L_s \equiv$ Thermopile sensor length	8 mm
$W_s \equiv$ Thermopile sensor width	8 mm
$t_s \equiv$ Thermopile sensor thickness	100 $\mu\text{m}$
$L_r \equiv$ Reaction zone length	8 mm
$W_r \equiv$ Reaction zone width	3 mm
$h_r \equiv$ Reaction zone height	10 $\mu\text{m}$
$L_D \equiv$ Device length	75 mm
$W_d \equiv$ Device width	25 mm
$H_d \equiv$ Device height	1270 $\mu\text{m}$
$k_g \equiv$ Reaction rate constant	$3 \times 10^4 \text{ L mol}^{-1} \text{ s}^{-1}$ <sup>211</sup>

**Table A 4:** Parameters used to define the governing equations of the mathematical model.

Nomenclature	
$C_p$ Specific heat at constant pressure (kJ kg <sup>-1</sup> °C	$\Delta E$ Change in internal energy (J kg <sup>-1</sup> )
$k$ Thermal conductivity W m <sup>-1</sup> °C <sup>-1</sup>	$q$ Conductive heat flux vector
$u_m$ Mass velocity (kg m <sup>-2</sup> s <sup>-1</sup> )	$c_{Gox}$ Concentration of glucose oxidase (mol m <sup>-3</sup> )
$L$ Channel length (m)	$E_g$ Enzymatic reaction energy (J mol <sup>-1</sup> )
$U$ Velocity vector	$\mu$ Viscosity (kg m <sup>-1</sup> s <sup>-1</sup> )
$U^T$ Transpose of the velocity vector	$\rho$ Density (kg m <sup>-3</sup> )
$p$ Pressure (Pa)	$\sigma$ Total stress tensor
$x$ X-axis location	$\tau$ Viscous stress tensor
$y$ Y-axis location	$\beta$ Coefficient of thermal expansion (K <sup>-1</sup> )
$z$ Z-axis location	$\alpha$ Seebeck coefficient (μV mK <sup>-1</sup> )
$h$ Enthalpy (J)	
$u$ Velocity magnitude (ms <sup>-1</sup> )	<b>Subscript</b>
$c_g$ Concentration of glucose (mol m <sup>-3</sup> )	$f$ Fluid
$k_g$ Reaction rate constant (mol m <sup>-3</sup> s)	$g$ Glucose
$D_g$ Diffusion coefficient of glucose (m <sup>2</sup> s <sup>-1</sup> )	
$F_b$ Body force (N)	
$u_{in}$ Inlet velocity (ms <sup>-1</sup> )	
$T$ Temperature (K)	
$\Delta V$ Voltage difference (μV)	
$Q$ Heat rate (W m <sup>-3</sup> )	

**Table A 5:** Material properties of water, glass, PDMS, and PMMA obtained from the COMSOL library.

<b>Material property</b>	<b>Water</b>	<b>Glass</b>	<b>PMMA</b>	<b>PDMS</b>
Density ( $\text{kg m}^{-3}$ )	997	2203	1190	970
Specific heat capacity ( $\text{J kg}^{-1} \text{K}^{-1}$ )	4182	703	1420	1460
Thermal conductivity ( $\text{W m}^{-1} \text{K}^{-1}$ )	0.6	1.38	0.19	0.16



## BIBLIOGRAPHY

1. Luka, G. *et al.* Microfluidics Integrated Biosensors: A Leading Technology towards Lab-on-a-Chip and Sensing Applications. *Sensors* **15**, 30011–30031 (2015).
2. Bange, A., Wong, D. K. Y., Seliskar, C. J., Halsall, H. B. & Heineman, W. R. Microscale immunosensors for biological agents. in (eds. Papautsky, I. & Chartier, I.) 142 (2005). doi:10.1117/12.601758
3. Pires, N., Dong, T., Hanke, U. & Hoivik, N. Recent Developments in Optical Detection Technologies in Lab-on-a-Chip Devices for Biosensing Applications. *Sensors* **14**, 15458–15479 (2014).
4. Mohammed, M.-I. & Desmulliez, M. P. Y. Lab-on-a-chip based immunosensor principles and technologies for the detection of cardiac biomarkers: a review. *Lab Chip* **11**, 569–595 (2011).
5. Mayilo, S. *et al.* Long-Range Fluorescence Quenching by Gold Nanoparticles in a Sandwich Immunoassay for Cardiac Troponin T. *Nano Lett.* **9**, 4558–4563 (2009).
6. Zhu, Y.-D., Peng, J., Jiang, L.-P. & Zhu, J.-J. Fluorescent immunosensor based on CuS nanoparticles for sensitive detection of cancer biomarker. *Analyst* **139**, 649–655 (2014).
7. Pan, Y., Zhou, J., Su, K., Hu, N. & Wang, P. A Novel Quantum Dot Fluorescence Immunosensor Based on Magnetic Beads and Portable Flow Cytometry for Detection of Okadaic Acid. *Procedia Technol.* **27**, 214–216 (2017).
8. Li, M. *et al.* An ultrasensitive sandwich-type electrochemical immunosensor based on the signal amplification strategy of mesoporous core-shell Pd@Pt nanoparticles/amino group functionalized graphene nanocomposite. *Biosens. Bioelectron.* **87**, 752–759 (2017).
9. Xiong, P. *et al.* An Ultrasensitive Electrochemical Immunosensor for Alpha-Fetoprotein Using an Envision Complex-Antibody Copolymer as a Sensitive Label. *Materials (Basel)*. **5**, 2757–2772 (2012).
10. Cheng, C.-M. *et al.* Paper-Based ELISA. *Angew. Chemie Int. Ed.* **49**, 4771–4774 (2010).

11. Lei, K. F. *et al.* Paper-based enzyme-free immunoassay for rapid detection and subtyping of influenza A H1N1 and H3N2 viruses. *Anal. Chim. Acta* **883**, 37–44 (2015).
12. Sassa, F., Morimoto, K., Satoh, W. & Suzuki, H. Electrochemical techniques for microfluidic applications. *Electrophoresis* **29**, 1787–1800 (2008).
13. Wu, J., Fu, Z., Yan, F. & Ju, H. Biomedical and clinical applications of immunoassays and immunosensors for tumor markers. *TrAC Trends Anal. Chem.* **26**, 679–688 (2007).
14. Liana, D. D., Raguse, B., Gooding, J. J. & Chow, E. Recent Advances in Paper-Based Sensors. *Sensors* **12**, 11505–11526 (2012).
15. Rothbauer, M., Zirath, H. & Ertl, P. Recent advances in microfluidic technologies for cell-to-cell interaction studies. *Lab Chip* **18**, 249–270 (2018).
16. Lin, S. *et al.* Progress in Microfluidics-Based Exosome Separation and Detection Technologies for Diagnostic Applications. *Small* **16**, 1903916 (2020).
17. EL Andaloussi, S., Mäger, I., Breakefield, X. O. & Wood, M. J. A. Extracellular vesicles: biology and emerging therapeutic opportunities. *Nat. Rev. Drug Discov.* **12**, 347–357 (2013).
18. Raposo, G. & Stoorvogel, W. Extracellular vesicles: Exosomes, microvesicles, and friends. *J. Cell Biol.* **200**, 373–383 (2013).
19. Katsuda, T., Kosaka, N. & Ochiya, T. The roles of extracellular vesicles in cancer biology: Toward the development of novel cancer biomarkers. *Proteomics* **14**, 412–425 (2014).
20. Contreras-Naranjo, J. C., Wu, H.-J. & Ugaz, V. M. Microfluidics for exosome isolation and analysis: enabling liquid biopsy for personalized medicine. *Lab Chip* **17**, 3558–3577 (2017).
21. Guo, S.-C., Tao, S.-C. & Dawn, H. Microfluidics-based on-a-chip systems for isolating and analysing extracellular vesicles. *J. Extracell. Vesicles* **7**, 1508271 (2018).
22. Jia, Y., Ni, Z., Sun, H. & Wang, C. Microfluidic Approaches Toward the Isolation and Detection of Exosome Nanovesicles. *IEEE Access* **7**, 45080–45098 (2019).
23. Andreu, Z. & Yáñez-Muñoz, M. Tetraspanins in Extracellular Vesicle Formation and Function. *Front. Immunol.* **5**, (2014).

24. Kowal, J. *et al.* Proteomic comparison defines novel markers to characterize heterogeneous populations of extracellular vesicle subtypes. *Proc. Natl. Acad. Sci.* **113**, E968–E977 (2016).
25. Men, Y. *et al.* Exosome reporter mice reveal the involvement of exosomes in mediating neuron to astroglia communication in the CNS. *Nat. Commun.* **10**, 4136 (2019).
26. Zakeri, Z. *et al.* MicroRNA and exosome: Key players in rheumatoid arthritis. *J. Cell. Biochem.* **120**, 10930–10944 (2019).
27. Mizutani, K. *et al.* Urinary exosome as a potential biomarker for urinary tract infection. *Cell. Microbiol.* **21**, (2019).
28. Cañas, J. A., Sastre, B., Rodrigo-Muñoz, J. M. & del Pozo, V. Exosomes: A new approach to asthma pathology. *Clin. Chim. Acta* **495**, 139–147 (2019).
29. Kalluri, R. & LeBleu, V. S. The biology , function , and biomedical applications of exosomes. *Science (80-. ).* **367**, eaau6977 (2020).
30. de Gonzalo-Calvo, D. *et al.* Differential inflammatory responses in aging and disease: TNF- $\alpha$  and IL-6 as possible biomarkers. *Free Radic. Biol. Med.* **49**, 733–737 (2010).
31. Swardfager, W. *et al.* A Meta-Analysis of Cytokines in Alzheimer’s Disease. *Biol. Psychiatry* **68**, 930–941 (2010).
32. Reid, S. E., Murthy, M. S., Kaufman, M. & Scanlon, E. F. Endocrine and paracrine hormones in the promotion, progression and recurrence of breast cancer. *Br. J. Surg.* **83**, 1037–1046 (1996).
33. Arvin, B., Neville, L. F., Barone, F. C. & Feuerstein, G. Z. The Role of Inflammation and Cytokines in Brain Injury. *Neurosci. Biobehav. Rev.* **20**, 445–452 (1996).
34. Ng, A. H. C., Uddayasankar, U. & Wheeler, A. R. Immunoassays in microfluidic systems. *Anal. Bioanal. Chem.* **397**, 991–1007 (2010).
35. Herrmann, M., Veres, T. & Tabrizian, M. Quantification of Low-Picomolar Concentrations of TNF- $\alpha$  in Serum Using the Dual-Network Microfluidic ELISA Platform. *Anal. Chem.* **80**, 5160–5167 (2008).
36. Cesaro-Tadic, S. *et al.* High-sensitivity miniaturized immunoassays for tumor necrosis factor alpha using microfluidic systems. *Lab Chip* **4**, 563–569 (2004).

37. Bellagambi, F. G. *et al.* Electrochemical biosensor platform for TNF- $\alpha$  cytokines detection in both artificial and human saliva: Heart failure. *Sensors Actuators B Chem.* **251**, 1026–1033 (2017).
38. Yin, Z., Liu, Y., Jiang, L.-P. & Zhu, J.-J. Electrochemical immunosensor of tumor necrosis factor  $\alpha$  based on alkaline phosphatase functionalized nanospheres. *Biosens. Bioelectron.* **26**, 1890–1894 (2011).
39. Kongsuphol, P. *et al.* EIS-based biosensor for ultra-sensitive detection of TNF- $\alpha$  from non-diluted human serum. *Biosens. Bioelectron.* **61**, 274–279 (2014).
40. Lee, W., Lee & Koh. Development and applications of chip calorimeters as novel biosensors. *Nanobiosensors Dis. Diagnosis* **1**, 17–29 (2012).
41. Higuera-Guisset, J. *et al.* Calorimetry of microbial growth using a thermopile based microreactor. *Thermochim. Acta* **427**, 187–191 (2005).
42. Nestorova, G. G., Koppa, V. L., Crews, N. D. & Guilbeau, E. J. Thermoelectric lab-on-a-chip ELISA. *Anal. Methods* **7**, 2055–2063 (2015).
43. Nestorova, G. G. & Guilbeau, E. J. Thermoelectric method for sequencing DNA. *Lab Chip* **11**, 1761–1769 (2011).
44. Tangutooru, S. M., Koppa, V. L., Nestorova, G. G. & Guilbeau, E. J. Dynamic thermoelectric glucose sensing with layer-by-layer glucose oxidase immobilization. *Sensors Actuators B Chem.* **166–167**, 637–641 (2012).
45. Ahmad, L. M., Towe, B., Wolf, A., Mertens, F. & Lerchner, J. Binding event measurement using a chip calorimeter coupled to magnetic beads. *Sensors Actuators B Chem.* **145**, 239–245 (2010).
46. Ayala-Mar, S., Donoso-Quezada, J., Gallo-Villanueva, R. C., Perez-Gonzalez, V. H. & González-Valdez, J. Recent advances and challenges in the recovery and purification of cellular exosomes. *Electrophoresis* **40**, 3036–3049 (2019).
47. Doyle, L. & Wang, M. Overview of Extracellular Vesicles, Their Origin, Composition, Purpose, and Methods for Exosome Isolation and Analysis. *Cells* **8**, 727 (2019).
48. Livshits, M. A. *et al.* Isolation of exosomes by differential centrifugation: Theoretical analysis of a commonly used protocol. *Sci. Rep.* **5**, 17319 (2015).
49. Gheinani, A. H. *et al.* Improved isolation strategies to increase the yield and purity of human urinary exosomes for biomarker discovery. *Sci. Rep.* **8**, 3945 (2018).

50. Konoshenko, M. Y., Lekchnov, E. A., Vlassov, A. V. & Laktionov, P. P. Isolation of Extracellular Vesicles: General Methodologies and Latest Trends. *Biomed Res. Int.* **2018**, 1–27 (2018).
51. Lee, K., Shao, H., Weissleder, R. & Lee, H. Acoustic Purification of Extracellular Microvesicles. *ACS Nano* **9**, 2321–2327 (2015).
52. Zhao, Z., Yang, Y., Zeng, Y. & He, M. A microfluidic ExoSearch chip for multiplexed exosome detection towards blood-based ovarian cancer diagnosis. *Lab Chip* **16**, 489–496 (2016).
53. Yu, L.-L. *et al.* A Comparison of Traditional and Novel Methods for the Separation of Exosomes from Human Samples. *Biomed Res. Int.* **2018**, 1–9 (2018).
54. Nwokwu, C. D., Ishraq Bari, S. M., Hutson, K. H., Brausell, C. & Nestorova, G. G. ExoPRIME: Solid-phase immunoisolation and OMICS analysis of surface-marker-specific exosomal subpopulations. *Talanta* **236**, 122870 (2022).
55. Cui, P. & Wang, S. Application of microfluidic chip technology in pharmaceutical analysis: A review. *J. Pharm. Anal.* **9**, 238–247 (2019).
56. Liu, W. *et al.* An integrated microfluidic system for studying cell-microenvironmental interactions versatily and dynamically. *Lab Chip* **10**, 1717–1724 (2010).
57. Shi, M. *et al.* Glia co-culture with neurons in microfluidic platforms promotes the formation and stabilization of synaptic contacts. *Lab Chip* **13**, 3008–3021 (2013).
58. Raposo, G. & Stoorvogel, W. Extracellular vesicles: Exosomes, microvesicles, and friends. *J. Cell Biol.* **200**, 373–383 (2013).
59. Guo, S.-C., Tao, S.-C. & Dawn, H. Microfluidics-based on-a-chip systems for isolating and analysing extracellular vesicles. *J. Extracell. Vesicles* **7**, 1508271 (2018).
60. Mizutani, K. *et al.* Urinary exosome as a potential biomarker for urinary tract infection. *Cell. Microbiol.* **21**, e13020 (2019).
61. Cooper, J. M. *et al.* Systemic exosomal siRNA delivery reduced alpha-synuclein aggregates in brains of transgenic mice. *Mov. Disord.* **29**, 1476–1485 (2014).
62. van Niel, G. *et al.* The Tetraspanin CD63 Regulates ESCRT-Independent and -Dependent Endosomal Sorting during Melanogenesis. *Dev. Cell* **21**, 708–721 (2011).

63. Conde-Vancells, J. *et al.* Characterization and Comprehensive Proteome Profiling of Exosomes Secreted by Hepatocytes. *J. Proteome Res.* **7**, 5157–5166 (2008).
64. Subra, C. *et al.* Exosomes account for vesicle-mediated transcellular transport of activatable phospholipases and prostaglandins. *J. Lipid Res.* **51**, 2105–2120 (2010).
65. Hou, R. *et al.* Advances in exosome isolation methods and their applications in proteomic analysis of biological samples. *Anal. Bioanal. Chem.* **411**, 5351–5361 (2019).
66. Purushothaman, A. Exosomes from Cell Culture-Conditioned Medium: Isolation by Ultracentrifugation and Characterization. in 233–244 (2019).
67. Lobb, R. & Möller, A. Size Exclusion Chromatography: A Simple and Reliable Method for Exosome Purification. in 105–110 (2017).
68. Xu, R., Simpson, R. J. & Greening, D. W. A Protocol for Isolation and Proteomic Characterization of Distinct Extracellular Vesicle Subtypes by Sequential Centrifugal Ultrafiltration. in 91–116 (2017).
69. Weng, Y. *et al.* Effective isolation of exosomes with polyethylene glycol from cell culture supernatant for in-depth proteome profiling. *Analyst* **141**, 4640–4646 (2016).
70. Hong, C. S., Muller, L., Boyiadzis, M. & Whiteside, T. L. Isolation and Characterization of CD34+ Blast-Derived Exosomes in Acute Myeloid Leukemia. *PLoS One* **9**, e103310 (2014).
71. Mastoridis, S. *et al.* Multiparametric Analysis of Circulating Exosomes and Other Small Extracellular Vesicles by Advanced Imaging Flow Cytometry. *Front. Immunol.* **9**, (2018).
72. Wu, Y., Deng, W. & Klinken, D. J. Exosomes: improved methods to characterize their morphology, RNA content, and surface protein biomarkers. *Analyst* **140**, 6631–6642 (2015).
73. Chen, Z. *et al.* Detection of exosomes by ZnO nanowires coated three-dimensional scaffold chip device. *Biosens. Bioelectron.* **122**, 211–216 (2018).
74. Yakovlev, A. A. *et al.* Elevated Levels of Serum Exosomes in Patients with Major Depressive Disorder. *Neurochem. J.* **13**, 385–390 (2019).
75. Zhang, H., Wang, Z., Zhang, Q., Wang, F. & Liu, Y. Ti3C2 MXenes nanosheets catalyzed highly efficient electrogenerated chemiluminescence biosensor for the detection of exosomes. *Biosens. Bioelectron.* **124–125**, 184–190 (2019).

76. Khodashenas, S., Khalili, S. & Forouzandeh Moghadam, M. A cell ELISA based method for exosome detection in diagnostic and therapeutic applications. *Biotechnol. Lett.* **41**, 523–531 (2019).
77. Chen, J. *et al.* Structure-switching aptamer triggering hybridization displacement reaction for label-free detection of exosomes. *Talanta* **209**, 120510 (2020).
78. Su, W., Li, H., Chen, W. & Qin, J. Microfluidic strategies for label-free exosomes isolation and analysis. *TrAC Trends Anal. Chem.* **118**, 686–698 (2019).
79. Sinha, N., Subedi, N. & Tel, J. Integrating Immunology and Microfluidics for Single Immune Cell Analysis. *Front. Immunol.* **9**, 151–173 (2018).
80. Dusny, C. & Grünberger, A. Microfluidic single-cell analysis in biotechnology: from monitoring towards understanding. *Curr. Opin. Biotechnol.* **63**, 26–33 (2020).
81. Hu, J. *et al.* Portable microfluidic and smartphone-based devices for monitoring of cardiovascular diseases at the point of care. *Biotechnol. Adv.* **34**, 305–320 (2016).
82. Hassan, S. *et al.* Capillary-Driven Flow Microfluidics Combined with Smartphone Detection: An Emerging Tool for Point-of-Care Diagnostics. *Diagnostics* **10**, 509 (2020).
83. Bari, S. M. I., Reis, L. G. & Nestorova, G. G. Calorimetric sandwich-type immunosensor for quantification of TNF- $\alpha$ . *Biosens. Bioelectron.* **126**, 82–87 (2019).
84. Zhu, C., Maldonado, J., Tang, H., Venkatesh, S. & Sengupta, K. CMOS-Driven Pneumatic-Free Scalable Microfluidics and Fluid Processing with Label-Free Cellular and Bio-Molecular Sensing Capability for an End-to-End Point-of-Care System. in *2021 IEEE International Solid- State Circuits Conference (ISSCC)* 278–280 (IEEE, 2021).
85. Jafari, D. *et al.* The relationship between molecular content of mesenchymal stem cells derived exosomes and their potentials: Opening the way for exosomes based therapeutics. *Biochimie* **165**, 76–89 (2019).
86. Cheng, N. *et al.* Recent Advances in Biosensors for Detecting Cancer-Derived Exosomes. *Trends Biotechnol.* **37**, 1236–1254 (2019).
87. Yi, Y. W. *et al.* Advances in Analysis of Biodistribution of Exosomes by Molecular Imaging. *Int. J. Mol. Sci.* **21**, 665 (2020).

88. Woo, H.-K. *et al.* Exodisc for Rapid, Size-Selective, and Efficient Isolation and Analysis of Nanoscale Extracellular Vesicles from Biological Samples. *ACS Nano* **11**, 1360–1370 (2017).
89. Kanwar, S. S., Dunlay, C. J., Simeone, D. M. & Negrath, S. Microfluidic device (ExoChip) for on-chip isolation, quantification and characterization of circulating exosomes. *Lab Chip* **14**, 1891–1900 (2014).
90. Yasui, T. *et al.* Unveiling massive numbers of cancer-related urinary-microRNA candidates via nanowires. *Sci. Adv.* **3**, e1701133 (2017).
91. Huang, L. R. Continuous Particle Separation Through Deterministic Lateral Displacement. *Science* (80-. ). **304**, 987–990 (2004).
92. Wu, M. *et al.* Isolation of exosomes from whole blood by integrating acoustics and microfluidics. *Proc. Natl. Acad. Sci.* **114**, 10584–10589 (2017).
93. Cho, S. *et al.* Isolation of extracellular vesicle from blood plasma using electrophoretic migration through porous membrane. *Sensors Actuators B Chem.* **233**, 289–297 (2016).
94. Iliescu, F., Vrtačnik, D., Neuzil, P. & Iliescu, C. Microfluidic Technology for Clinical Applications of Exosomes. *Micromachines* **10**, 392 (2019).
95. Théry, C., Zitvogel, L. & Amigorena, S. Exosomes: composition, biogenesis and function. *Nat. Rev. Immunol.* **2**, 569–579 (2002).
96. Farooqi, A. A. *et al.* Exosome biogenesis, bioactivities and functions as new delivery systems of natural compounds. *Biotechnol. Adv.* **36**, 328–334 (2018).
97. Colombo, M. *et al.* Analysis of ESCRT functions in exosome biogenesis, composition and secretion highlights the heterogeneity of extracellular vesicles. *J. Cell Sci.* **126**, 5553–5565 (2013).
98. Margolis, L. & Sadovsky, Y. The biology of extracellular vesicles: The known unknowns. *PLOS Biol.* **17**, e3000363 (2019).
99. Pathan, M. *et al.* Vesiclepedia 2019: a compendium of RNA, proteins, lipids and metabolites in extracellular vesicles. *Nucleic Acids Res.* **47**, D516–D519 (2019).
100. Zaborowski, M. P., Balaj, L., Breakefield, X. O. & Lai, C. P. Extracellular Vesicles: Composition, Biological Relevance, and Methods of Study. *Bioscience* **65**, 783–797 (2015).
101. Kowal, J., Tkach, M. & Théry, C. Biogenesis and secretion of exosomes. *Curr. Opin. Cell Biol.* **29**, 116–125 (2014).



102. Morita, E. *et al.* Human ESCRT and ALIX proteins interact with proteins of the midbody and function in cytokinesis. *EMBO J.* **26**, 4215–4227 (2007).
103. Géminard, C., de Gassart, A., Blanc, L. & Vidal, M. Degradation of AP2 During Reticulocyte Maturation Enhances Binding of Hsc70 and Alix to a Common Site on TfR for Sorting into Exosomes. *Traffic* **5**, 181–193 (2004).
104. Witwer, K. W. *et al.* Standardization of sample collection, isolation and analysis methods in extracellular vesicle research. *J. Extracell. Vesicles* **2**, 20360 (2013).
105. Crescitelli, R. *et al.* Distinct RNA profiles in subpopulations of extracellular vesicles: apoptotic bodies, microvesicles and exosomes. *J. Extracell. Vesicles* **2**, 20677 (2013).
106. Beach, A., Zhang, H.-G., Ratajczak, M. Z. & Kakar, S. S. Exosomes: an overview of biogenesis, composition and role in ovarian cancer. *J. Ovarian Res.* **7**, 14 (2014).
107. Lim, L. P. *et al.* Microarray analysis shows that some microRNAs downregulate large numbers of target mRNAs. *Nature* **433**, 769–773 (2005).
108. Bullock, M. *et al.* Exosomal Non-Coding RNAs: Diagnostic, Prognostic and Therapeutic Applications in Cancer. *Non-Coding RNA* **1**, 53–68 (2015).
109. Nahand, J. S. *et al.* Exosomal miRNAs: novel players in viral infection. *Epigenomics* **12**, 353–370 (2020).
110. Mao, L. *et al.* Serum exosomes contain ECRG4 mRNA that suppresses tumor growth via inhibition of genes involved in inflammation, cell proliferation, and angiogenesis. *Cancer Gene Ther.* **25**, 248–259 (2018).
111. Zhang, Y. *et al.* Transfer RNA-derived fragments as potential exosome tRNA-derived fragment biomarkers for osteoporosis. *Int. J. Rheum. Dis.* **21**, 1659–1669 (2018).
112. Möhrmann, L. *et al.* Liquid Biopsies Using Plasma Exosomal Nucleic Acids and Plasma Cell-Free DNA Compared with Clinical Outcomes of Patients with Advanced Cancers. *Clin. Cancer Res.* **24**, 181–188 (2018).
113. Tellez-Gabriel, M., Knutsen, E. & Perander, M. Current Status of Circulating Tumor Cells, Circulating Tumor DNA, and Exosomes in Breast Cancer Liquid Biopsies. *Int. J. Mol. Sci.* **21**, 9457 (2020).
114. Record, M., Silvente-Poirot, S., Poirot, M. & Wakelam, M. O. Extracellular vesicles: lipids as key components of their biogenesis and functions. *J. Lipid Res.* **59**, 1316–1324 (2018).

115. Skotland, T., Hessvik, N. P., Sandvig, K. & Llorente, A. Exosomal lipid composition and the role of ether lipids and phosphoinositides in exosome biology. *J. Lipid Res.* **60**, 9–18 (2019).
116. Ferguson Bennit, H. R., Gonda, A., McMullen, J. R. W., Kabagwira, J. & Wall, N. R. Peripheral Blood Cell Interactions of Cancer-Derived Exosomes Affect Immune Function. *Cancer Microenviron.* **12**, 29–35 (2019).
117. Skog, J. *et al.* Glioblastoma microvesicles transport RNA and proteins that promote tumour growth and provide diagnostic biomarkers. *Nat. Cell Biol.* **10**, 1470–1476 (2008).
118. Ståhl, A., Johansson, K., Mossberg, M., Kahn, R. & Karpman, D. Exosomes and microvesicles in normal physiology, pathophysiology, and renal diseases. *Pediatr. Nephrol.* **34**, 11–30 (2019).
119. Solé, C., Cortés-Hernández, J., Felip, M. L., Vidal, M. & Ordi-Ros, J. miR-29c in urinary exosomes as predictor of early renal fibrosis in lupus nephritis. *Nephrol. Dial. Transplant.* **30**, 1488–1496 (2015).
120. Hiemstra, T. F. *et al.* Human Urinary Exosomes as Innate Immune Effectors. *J. Am. Soc. Nephrol.* **25**, 2017–2027 (2014).
121. Biró, O. *et al.* Circulating exosomal and Argonaute-bound microRNAs in preeclampsia. *Gene* **692**, 138–144 (2019).
122. Iranifar, E. *et al.* Exosomes and microRNAs: New potential therapeutic candidates in Alzheimer disease therapy. *J. Cell. Physiol.* **234**, 2296–2305 (2019).
123. Khushman, M. *et al.* Exosomal markers (CD63 and CD9) expression and their prognostic significance using immunohistochemistry in patients with pancreatic ductal adenocarcinoma. *J. Gastrointest. Oncol.* **10**, 695–702 (2019).
124. Kalra, H. *et al.* Comparative proteomics evaluation of plasma exosome isolation techniques and assessment of the stability of exosomes in normal human blood plasma. *Proteomics* **13**, 3354–3364 (2013).
125. Luo, S., Du, L. & Cui, Y. The potential therapeutic applications and developments of exosomes in Parkinson's Disease. *Mol. Pharm.* [acs.molpharmaceut.0c00195](https://doi.org/10.1021/acs.molpharmaceut.0c00195) (2020).
126. Niu, X., Chen, J. & Gao, J. Nanocarriers as a powerful vehicle to overcome blood-brain barrier in treating neurodegenerative diseases: Focus on recent advances. *Asian J. Pharm. Sci.* **14**, 480–496 (2019).

127. Pascucci, L. *et al.* Paclitaxel is incorporated by mesenchymal stromal cells and released in exosomes that inhibit in vitro tumor growth: A new approach for drug delivery. *J. Control. Release* **192**, 262–270 (2014).
128. Kim, M. S. *et al.* Engineering macrophage-derived exosomes for targeted paclitaxel delivery to pulmonary metastases: in vitro and in vivo evaluations. *Nanomedicine Nanotechnology, Biol. Med.* **14**, 195–204 (2018).
129. Sidhom, K., Obi, P. O. & Saleem, A. A Review of Exosomal Isolation Methods: Is Size Exclusion Chromatography the Best Option? *Int. J. Mol. Sci.* **21**, 6466 (2020).
130. Livshits, M. A. *et al.* Isolation of exosomes by differential centrifugation: Theoretical analysis of a commonly used protocol. *Sci. Rep.* **5**, 17319 (2015).
131. Lobb, R. J. *et al.* Optimized exosome isolation protocol for cell culture supernatant and human plasma. *J. Extracell. Vesicles* **4**, 27031 (2015).
132. Klingeborn, M., Skiba, N. P., Stamer, W. D. & Bowes Rickman, C. Isolation of Retinal Exosome Biomarkers from Blood by Targeted Immunocapture. in 21–25 (2019).
133. Sharma, P. *et al.* Immunoaffinity-based isolation of melanoma cell-derived exosomes from plasma of patients with melanoma. *J. Extracell. Vesicles* **7**, 1435138 (2018).
134. Cui, B., Liu, C. & Yao, S. One-Step RT-PCR for Detection of Micrnas in Exosomes Using Droplet Microfluidics. in *2020 IEEE 33rd International Conference on Micro Electro Mechanical Systems (MEMS)* 142–146 (IEEE, 2020).
135. Ludwig, N., Whiteside, T. L. & Reichert, T. E. Challenges in Exosome Isolation and Analysis in Health and Disease. *Int. J. Mol. Sci.* **20**, 4684 (2019).
136. Zarovni, N. *et al.* Integrated isolation and quantitative analysis of exosome shuttled proteins and nucleic acids using immunocapture approaches. *Methods* **87**, 46–58 (2015).
137. Li, P., Kaslan, M., Lee, S. H., Yao, J. & Gao, Z. Progress in Exosome Isolation Techniques. *Theranostics* **7**, 789–804 (2017).
138. Xiao, D. *et al.* Identifying mRNA, MicroRNA and Protein Profiles of Melanoma Exosomes. *PLoS One* **7**, e46874 (2012).

139. Alvarez, M. L., Khosroheidari, M., Kanchi Ravi, R. & DiStefano, J. K. Comparison of protein, microRNA, and mRNA yields using different methods of urinary exosome isolation for the discovery of kidney disease biomarkers. *Kidney Int.* **82**, 1024–1032 (2012).
140. He, L., Zhu, D., Wang, J. & Wu, X. A highly efficient method for isolating urinary exosomes. *Int. J. Mol. Med.* **43**, 83–90 (2018).
141. Batrakova, E. V. & Kim, M. S. Using exosomes, naturally-equipped nanocarriers, for drug delivery. *J. Control. Release* **219**, 396–405 (2015).
142. Navajas, R., Corrales, F. J. & Paradela, A. Serum Exosome Isolation by Size-Exclusion Chromatography for the Discovery and Validation of Preeclampsia-Associated Biomarkers. in 39–50 (2019).
143. Guerreiro, E. M. *et al.* Efficient extracellular vesicle isolation by combining cell media modifications, ultrafiltration, and size-exclusion chromatography. *PLoS One* **13**, e0204276 (2018).
144. Mitchell, M. D. Exosome enrichment by ultracentrifugation and size exclusion chromatography. *Front. Biosci.* **23**, 4621 (2018).
145. Soares Martins, T., Catita, J., Martins Rosa, I., A. B. da Cruz e Silva, O. & Henriques, A. G. Exosome isolation from distinct biofluids using precipitation and column-based approaches. *PLoS One* **13**, e0198820 (2018).
146. Greening, D. W., Xu, R., Ji, H., Tauro, B. J. & Simpson, R. J. A Protocol for Exosome Isolation and Characterization: Evaluation of Ultracentrifugation, Density-Gradient Separation, and Immunoaffinity Capture Methods. in 179–209 (2015).
147. Theodoraki, M., Hong, C., Donnenberg, V. S., Donnenberg, A. D. & Whiteside, T. L. Evaluation of Exosome Proteins by on-Bead Flow Cytometry. *Cytom. Part A* cyto.a.24193 (2020).
148. van der Vlist, E. J., Nolte-'t Hoen, E. N. M., Stoorvogel, W., Arkesteijn, G. J. A. & Wauben, M. H. M. Fluorescent labeling of nano-sized vesicles released by cells and subsequent quantitative and qualitative analysis by high-resolution flow cytometry. *Nat. Protoc.* **7**, 1311–1326 (2012).
149. Boriachek, K. *et al.* Biological Functions and Current Advances in Isolation and Detection Strategies for Exosome Nanovesicles. *Small* **14**, 1702153 (2018).

150. Theodoraki, M.-N., Matsumoto, A., Beccard, I., Hoffmann, T. K. & Whiteside, T. L. CD44v3 protein-carrying tumor-derived exosomes in HNSCC patients' plasma as potential noninvasive biomarkers of disease activity. *Oncoimmunology* **9**, 1747732 (2020).
151. Severic, M. *et al.* Genetically-engineered anti-PSMA exosome mimetics targeting advanced prostate cancer in vitro and in vivo. *J. Control. Release* **330**, 101–110 (2021).
152. Wang, K. *et al.* An exosome-like programmable-bioactivating paclitaxel prodrug nanoplatform for enhanced breast cancer metastasis inhibition. *Biomaterials* **257**, 120224 (2020).
153. Logozzi, M. *et al.* High Levels of Exosomes Expressing CD63 and Caveolin-1 in Plasma of Melanoma Patients. *PLoS One* **4**, e5219 (2009).
154. Serrano-Pertierra, E. *et al.* Extracellular Vesicles: Current Analytical Techniques for Detection and Quantification. *Biomolecules* **10**, 824 (2020).
155. Wang, C. *et al.* Droplet digital PCR improves urinary exosomal miRNA detection compared to real-time PCR. *Clin. Biochem.* **67**, 54–59 (2019).
156. Cho, S. M. *et al.* A novel approach for tuberculosis diagnosis using exosomal DNA and droplet digital PCR. *Clin. Microbiol. Infect.* **26**, 942.e1-942.e5 (2020).
157. Anderson, W., Lane, R., Korbie, D. & Trau, M. Observations of Tunable Resistive Pulse Sensing for Exosome Analysis: Improving System Sensitivity and Stability. *Langmuir* **31**, 6577–6587 (2015).
158. Yamauchi, M. *et al.* Efficient method for isolation of exosomes from raw bovine milk. *Drug Dev. Ind. Pharm.* **45**, 359–364 (2019).
159. Dou, D. *et al.* Cancer-Associated Fibroblasts-Derived Exosomes Suppress Immune Cell Function in Breast Cancer via the miR-92/PD-L1 Pathway. *Front. Immunol.* **11**, (2020).
160. Liu, C. *et al.* Field-Free Isolation of Exosomes from Extracellular Vesicles by Microfluidic Viscoelastic Flows. *ACS Nano* **11**, 6968–6976 (2017).
161. Gaillard, M. *et al.* Biosensing extracellular vesicles: contribution of biomolecules in affinity-based methods for detection and isolation. *Analyst* **145**, 1997–2013 (2020).
162. Gurunathan, S., Kang, M.-H., Jeyaraj, M., Qasim, M. & Kim, J.-H. Review of the Isolation, Characterization, Biological Function, and Multifarious Therapeutic Approaches of Exosomes. *Cells* **8**, 307 (2019).

163. Wang, W., Wu, C. & Jin, H. Exosomes in chronic inflammatory skin diseases and skin tumors. *Exp. Dermatol.* exd.13857 (2018).
164. Wang, J., Ma, P., Kim, D. H., Liu, B.-F. & Demirci, U. Towards microfluidic-based exosome isolation and detection for tumor therapy. *Nano Today* **37**, 101066 (2021).
165. Le, M.-C. N. & Fan, H. Z. Exosome isolation using nanostructures and microfluidic devices. *Biomed. Mater.* (2021).
166. Lin, B. *et al.* Microfluidic-Based Exosome Analysis for Liquid Biopsy. *Small Methods* **5**, 2001131 (2021).
167. Davies, R. T. *et al.* Microfluidic filtration system to isolate extracellular vesicles from blood. *Lab Chip* **12**, 5202–5210 (2012).
168. Liang, L.-G. *et al.* An integrated double-filtration microfluidic device for isolation, enrichment and quantification of urinary extracellular vesicles for detection of bladder cancer. *Sci. Rep.* **7**, 46224 (2017).
169. Wang, Z. *et al.* Ciliated micropillars for the microfluidic-based isolation of nanoscale lipid vesicles. *Lab Chip* **13**, 2879 (2013).
170. Qi, R. *et al.* Microfluidic device for the analysis of MDR cancerous cell-derived exosomes' response to nanotherapy. *Biomed. Microdevices* **21**, 35 (2019).
171. Chen, C. *et al.* Microfluidic isolation and transcriptome analysis of serum microvesicles. *Lab Chip* **10**, 505–511 (2010).
172. Zhang, P., He, M. & Zeng, Y. Ultrasensitive microfluidic analysis of circulating exosomes using a nanostructured graphene oxide/polydopamine coating. *Lab Chip* **16**, 3033–3042 (2016).
173. Zhang, Y. *et al.* A herringbone mixer based microfluidic device HBEXO-chip for purifying tumor-derived exosomes and establishing miRNA signature in pancreatic cancer. *Sensors Actuators B Chem.* **332**, 129511 (2021).
174. Ding, X. *et al.* On-chip manipulation of single microparticles, cells, and organisms using surface acoustic waves. *Proc. Natl. Acad. Sci.* **109**, 11105–11109 (2012).
175. Wang, Z. *et al.* Acoustofluidic separation enables early diagnosis of traumatic brain injury based on circulating exosomes. *Microsystems Nanoeng.* **7**, 20 (2021).
176. Wang, Z. *et al.* Acoustofluidic Salivary Exosome Isolation. *J. Mol. Diagnostics* **22**, 50–59 (2020).

177. Hattori, Y., Shimada, T., Yasui, T., Kaji, N. & Baba, Y. Micro- and Nanopillar Chips for Continuous Separation of Extracellular Vesicles. *Anal. Chem.* **91**, 6514–6521 (2019).
178. Smith, J. T. *et al.* Integrated nanoscale deterministic lateral displacement arrays for separation of extracellular vesicles from clinically-relevant volumes of biological samples. *Lab Chip* **18**, 3913–3925 (2018).
179. Salafi, T., Zhang, Y. & Zhang, Y. A Review on Deterministic Lateral Displacement for Particle Separation and Detection. *Nano-Micro Lett.* **11**, 77 (2019).
180. Santana, S. M., Antonyak, M. A., Cerione, R. A. & Kirby, B. J. Microfluidic isolation of cancer-cell-derived microvesicles from heterogeneous extracellular shed vesicle populations. *Biomed. Microdevices* **16**, 869–877 (2014).
181. Zeming, K. K., Ranjan, S. & Zhang, Y. Rotational separation of non-spherical bioparticles using I-shaped pillar arrays in a microfluidic device. *Nat. Commun.* **4**, 1625 (2013).
182. Wunsch, B. H. *et al.* Nanoscale lateral displacement arrays for the separation of exosomes and colloids down to 20 nm. *Nat. Nanotechnol.* **11**, 936–940 (2016).
183. Zhou, Y., Ma, Z., Tayebi, M. & Ai, Y. Submicron Particle Focusing and Exosome Sorting by Wavy Microchannel Structures within Viscoelastic Fluids. *Anal. Chem.* **91**, 4577–4584 (2019).
184. Oh, J., Hart, R., Capurro, J. & Noh, H. (Moses). Comprehensive analysis of particle motion under non-uniform AC electric fields in a microchannel. *Lab Chip* **9**, 62–78 (2009).
185. Cheung, L., Sahloul, S., Orozaliyev, A. & Song, Y.-A. Rapid Detection and Trapping of Extracellular Vesicles by Electrokinetic Concentration for Liquid Biopsy on Chip. *Micromachines* **9**, 306 (2018).
186. Shi, L., Rana, A. & Esfandiari, L. A low voltage nanopipette dielectrophoretic device for rapid entrapment of nanoparticles and exosomes extracted from plasma of healthy donors. *Sci. Rep.* **8**, 6751 (2018).
187. Ibsen, S. D. *et al.* Rapid Isolation and Detection of Exosomes and Associated Biomarkers from Plasma. *ACS Nano* **11**, 6641–6651 (2017).
188. Lewis, J. M. *et al.* Integrated Analysis of Exosomal Protein Biomarkers on Alternating Current Electrokinetic Chips Enables Rapid Detection of Pancreatic Cancer in Patient Blood. *ACS Nano* **12**, 3311–3320 (2018).

189. Li, B. *et al.* Homogenous Magneto-Fluorescent Nanosensor for Tumor-Derived Exosome Isolation and Analysis. *ACS Sensors* **5**, 2052–2060 (2020).
190. Han, J., Zhang, L., Cui, M., Su, Y. & He, Y. Rapid and Accurate Detection of Lymph Node Metastases Enabled through Fluorescent Silicon Nanoparticles-Based Exosome Probes. *Anal. Chem.* **93**, 10122–10131 (2021).
191. Vaidyanathan, R. *et al.* Detecting Exosomes Specifically: A Multiplexed Device Based on Alternating Current Electrohydrodynamic Induced Nanoshearing. *Anal. Chem.* **86**, 11125–11132 (2014).
192. Xu, L., Chopdat, R., Li, D. & Al-Jamal, K. T. Development of a simple, sensitive and selective colorimetric aptasensor for the detection of cancer-derived exosomes. *Biosens. Bioelectron.* **169**, 112576 (2020).
193. Zhang, Y. *et al.* Plasmonic Colorimetric Biosensor for Sensitive Exosome Detection via Enzyme-Induced Etching of Gold Nanobipyramid@MnO<sub>2</sub> Nanosheet Nanostructures. *Anal. Chem.* **92**, 15244–15252 (2020).
194. Issadore, D. *et al.* Miniature magnetic resonance system for point-of-care diagnostics. *Lab Chip* **11**, 2282 (2011).
195. Shao, H. *et al.* Protein typing of circulating microvesicles allows real-time monitoring of glioblastoma therapy. *Nat. Med.* **18**, 1835–1840 (2012).
196. Sancho-Albero, M. *et al.* Isolation of exosomes from whole blood by a new microfluidic device: proof of concept application in the diagnosis and monitoring of pancreatic cancer. *J. Nanobiotechnology* **18**, 150 (2020).
197. Peixoto de Almeida, M. *et al.* Gold Nanoparticles as (Bio)Chemical Sensors. in 529–567 (2014).
198. Zeng, S., Baillargeat, D., Ho, H.-P. & Yong, K.-T. Nanomaterials enhanced surface plasmon resonance for biological and chemical sensing applications. *Chem. Soc. Rev.* **43**, 3426 (2014).
199. Zhu, L. *et al.* Label-Free Quantitative Detection of Tumor-Derived Exosomes through Surface Plasmon Resonance Imaging. *Anal. Chem.* **86**, 8857–8864 (2014).
200. Chen, W. *et al.* Surface plasmon resonance biosensor using hydrogel-AuNP supramolecular spheres for determination of prostate cancer-derived exosomes. *Microchim. Acta* **187**, 590 (2020).
201. Xu, L. *et al.* Optical, electrochemical and electrical (nano)biosensors for detection of exosomes: A comprehensive overview. *Biosens. Bioelectron.* **161**, 112222 (2020).



202. Zhou, Y.-G. *et al.* Interrogating Circulating Microsomes and Exosomes Using Metal Nanoparticles. *Small* **12**, 727–732 (2016).
203. Jeong, S. *et al.* Integrated Magneto–Electrochemical Sensor for Exosome Analysis. *ACS Nano* **10**, 1802–1809 (2016).
204. Cao, L., Han, G.-C., Xiao, H., Chen, Z. & Fang, C. A novel 3D paper-based microfluidic electrochemical glucose biosensor based on rGO-TEPA/PB sensitive film. *Anal. Chim. Acta* **1096**, 34–43 (2020).
205. Bruch, R. *et al.* CRISPR-powered electrochemical microfluidic multiplexed biosensor for target amplification-free miRNA diagnostics. *Biosens. Bioelectron.* **177**, 112887 (2021).
206. Kashefi-Kheyraadi, L. *et al.* Detachable microfluidic device implemented with electrochemical aptasensor (DeMEA) for sequential analysis of cancerous exosomes. *Biosens. Bioelectron.* **169**, 112622 (2020).
207. Samavedi, S., Vaidya, P., Gaddam, P., Whittington, A. R. & Goldstein, A. S. Electrospun meshes possessing region-wise differences in fiber orientation, diameter, chemistry and mechanical properties for engineering bone-ligament-bone tissues. *Biotechnol. Bioeng.* **111**, 2549–2559 (2014).
208. Edelman, J. L. & Castro, M. R. Quantitative Image Analysis of Laser-induced Choroidal Neovascularization in Rat. *Exp. Eye Res.* **71**, 523–533 (2000).
209. Weibel, B. Y. M. K. & Bright, H. J. Kinetic Behaviour of Glucose Oxidase Bound to Porous Glass Particles. *Biochem. J.* **124**, 801–807 (1971).
210. Hannoun, B. J. M. & Stephanopoulos, G. Diffusion coefficients of glucose and ethanol in cell-free and cell-occupied calcium alginate membranes. *Biotechnol. Bioeng.* **28**, 829–835 (1986).
211. Tao, Z., Raffel, R. A., Soud, A.-K. & Goodisman, J. Kinetic Studies on Enzyme-Catalyzed Reactions: Oxidation of Glucose, Decomposition of Hydrogen Peroxide and Their Combination. *Biophys. J.* **96**, 2977–2988 (2009).
212. Liao, Z. *et al.* Microfluidic chip coupled with optical biosensors for simultaneous detection of multiple analytes: A review. *Biosens. Bioelectron.* **126**, 697–706 (2019).
213. Bange, A., Wong, D. K. Y., Seliskar, C. J., Halsall, H. B. & Heineman, W. R. Microscale immunosensors for biological agents. in *Microfluidics, BioMEMS, and Medical Microsystems III* 142–150 (International Society for Optics and Photonics, 2005).

214. Nestorova, G. G., Kopparthy, V. L., Crews, N. D. & Guilbeau, E. J. Thermoelectric lab-on-a-chip ELISA. *Anal. Methods* **7**, 2055–2063 (2015).
215. Vermeir, S. *et al.* Computational Fluid Dynamics Model for Optimal Flow Injection Analysis Biosensor Design. in *IEEE Sensors* 365–368 (IEEE, 2005).
216. Ho, C.-M. & Tai, Y.-C. Micro-Electro-Mechanical-Systems (MEMS) and fluid flows. *Annu. Rev. Fluid Mech.* **30**, 579–612 (1998).
217. Darhuber, A. A. & Troian, S. M. Principles of microfluidic actuation by modulation of surface stresses. *Annu. Rev. Fluid Mech.* **37**, 425–455 (2005).
218. Chen, S. & Tian, Z. Simulation of thermal micro-flow using lattice Boltzmann method with Langmuir slip model. *Int. J. Heat Fluid Flow* **31**, 227–235 (2010).
219. Zhao, Z., Fisher, A. & Cheng, D. Numerical simulation in microfluidics and the introduction of the related software. in *Microfluidics: Fundamental, Devices and Applications* 147–174 (Wiley-VCH Verlag GmbH & Co. KGaA, 2018).
220. Nestorova, G. G., Crews, N. D. & Guilbeau, E. J. Theoretical and experimental analysis of thermoelectric lab-on-a-chip ELISA. *Microfluid. Nanofluidics* **19**, 963–972 (2015).
221. Jia, Y., Wang, B., Zhang, Z. & Lin, Q. A polymer-based MEMS differential scanning calorimeter. *Sensors Actuators A Phys.* **231**, 1–7 (2015).
222. Li Wang, Sipe, D. M., Yong Xu & Qiao Lin. A MEMS Thermal Biosensor for Metabolic Monitoring Applications. *J. Microelectromechanical Syst.* **17**, 318–327 (2008).
223. Nestorova, G. G., Adapa, B. S., Kopparthy, V. L. & Guilbeau, E. J. Lab-on-a-chip thermoelectric DNA biosensor for label-free detection of nucleic acid sequences. *Sensors Actuators B Chem.* **225**, 174–180 (2016).
224. Wang, S. *et al.* Micro-differential scanning calorimeter for liquid biological samples. *Rev. Sci. Instrum.* **87**, 105005 (2016).
225. Lerchner, J. *et al.* A new micro-fluid chip calorimeter for biochemical applications. *Thermochim. Acta* **445**, 144–150 (2006).
226. Kopparthy, V. L., Tangutooru, S. M., Nestorova, G. G. & Guilbeau, E. J. Thermoelectric microfluidic sensor for bio-chemical applications. *Sensors Actuators B Chem.* **166–167**, 608–615 (2012).

227. Davani, S., Kopparthy, V. L. & Crews, N. Detecting thermal asymmetry in microfluidics for sensor applications: Critical design considerations and optimization. *Int. J. Heat Mass Transf.* **133**, 572–580 (2019).
228. Lerchner, J., Wolf, A., Wolf, G. & Fernandez, I. Chip calorimeters for the investigation of liquid phase reactions: Design rules. *Thermochim. Acta* **446**, 168–175 (2006).
229. Li Wang & Qiao Lin. Theory and Experiments of MEMS Thermal Biosensors. in *2005 IEEE Engineering in Medicine and Biology 27th Annual Conference* 1301–1304 (IEEE, 2005).
230. Ishraq Bari, S. M., Reis, L. G. & Nestorova, G. G. Numerical Optimization of Key Design Parameters of a Thermoelectric Microfluidic Sensor for Ultrasensitive Detection of Biochemical Analytes. *J. Therm. Sci. Eng. Appl.* **13**, (2021).
231. Baesso, M. L., Shen, J. & Snook, R. D. Time-resolved thermal lens measurement of thermal diffusivity of soda—lime glass. *Chem. Phys. Lett.* **197**, 255–258 (1992).
232. Mark, J. . *Polymer Data Handbook*. (Oxford University Press, 1999).
233. Paguirigan, A. L. & Beebe, D. J. From the cellular perspective: exploring differences in the cellular baseline in macroscale and microfluidic cultures. *Integr. Biol.* **1**, 182–195 (2009).
234. Lee, J. N., Park, C. & Whitesides, G. M. Solvent Compatibility of Poly(dimethylsiloxane)-Based Microfluidic Devices. *Anal. Chem.* **75**, 6544–6554 (2003).
235. Gervais, T., El-Ali, J., Günther, A. & Jensen, K. F. Flow-induced deformation of shallow microfluidic channels. *Lab Chip* **6**, 500–507 (2006).
236. Majumdar, D., Gao, Y., Li, D. & Webb, D. J. Co-culture of neurons and glia in a novel microfluidic platform. *J. Neurosci. Methods* **196**, 38–44 (2011).
237. Jie, M., Li, H.-F., Lin, L., Zhang, J. & Lin, J.-M. Integrated microfluidic system for cell co-culture and simulation of drug metabolism. *RSC Adv.* **6**, 54564–54572 (2016).
238. Zeng, Y., Lee, T.-S., Yu, P. & Low, H.-T. Numerical Simulation on Mass Transport in a Microchannel Bioreactor for Co-culture Applications. *J. Biomech. Eng.* **129**, 365–373 (2007).
239. Ge, Z. *et al.* Development of Multi-Dimensional Cell Co-Culture via a Novel Microfluidic Chip Fabricated by DMD-Based Optical Projection Lithography. *IEEE Trans. Nanobioscience* **18**, 679–686 (2019).

- 240. Nestorova, G. G., Hasenstein, K., Nguyen, N., DeCoster, M. A. & Crews, N. D. Lab-on-a-chip mRNA purification and reverse transcription via a solid-phase gene extraction technique. *Lab Chip* **17**, 1128–1136 (2017).
- 241. Ishraq Bari, S. M., Reis, L. G., Holland, T. & Nestorova, G. G. Numerical Analysis of Optimal Design Parameters for a Cell Co-Culture Microfluidic Platform With an Integrated pressure-controlled Valve. in *Volume 12: Mechanics of Solids, Structures, and Fluids* (American Society of Mechanical Engineers, 2020).
- 242. Nunes, L. C. S. Mechanical characterization of hyperelastic polydimethylsiloxane by simple shear test. *Mater. Sci. Eng. A* **528**, 1799–1804 (2011).
- 243. Ngo, T. D., Kashani, A., Imbalzano, G., Nguyen, K. T. Q. & Hui, D. Additive manufacturing (3D printing): A review of materials, methods, applications and challenges. *Compos. Part B Eng.* **143**, 172–196 (2018).
- 244. Wang, Z., Volinsky, A. A. & Gallant, N. D. Crosslinking effect on polydimethylsiloxane elastic modulus measured by custom-built compression instrument. *J. Appl. Polym. Sci.* **131**, 41050 (2014).
- 245. Hocheng, H., Chen, C.-M., Chou, Y.-C. & Lin, C.-H. Study of novel electrical routing and integrated packaging on bio-compatible flexible substrates. *Microsyst. Technol.* **16**, 423–430 (2010).
- 246. Firpo, G., Angeli, E., Repetto, L. & Valbusa, U. Permeability thickness dependence of polydimethylsiloxane (PDMS) membranes. *J. Memb. Sci.* **481**, 1–8 (2015).